High-κ rare-earth oxides on GaN and ferroelectric properties of hafnia based thin films

Von der Fakultät für Mathematik, Informatik und Naturwissenschaften der RWTH Aachen University zur Erlangung des akademischen Grades eines Doktors der Naturwissenschaften genehmigte Dissertation

vorgelegt von

M. Sc. Thomas Carl Ulrich Tromm

aus Köln

Berichter: apl. Prof. Dr. phil. Siegfried Mantl
Univ.-Prof. Dr. rer. nat Joachim Mayer

Tag der mündlichen Prüfung: 14. Dezember 2018

Abstract

The continuous improvement of the transistors is the basis for the increase of computing power. For enhanced metal-oxide-semiconductor (MOS) field-effect-transistors (FETs) and other devices suitable gate dielectrics are required, that exhibit a high relative permittivity, good insulating properties like a large band gap, and a good layer quality. Additionally, new device structures like negative capacitance FET (NCFET) are developed.

In this thesis the ternary rare-earth oxides $GdScO_3$ (GSO), $LaLuO_3$ (LLO) and $SmScO_3$ (SSO) are grown on GaN by pulsed laser deposition (PLD). Those oxides reveal a hexagonal phase, that has been discovered few years ago. The oxides have a large lattice mismatch to the GaN and are not at thermodynamic equilibrium, according to ab-initio calculations. The hexagonal ternary rare-earth oxides reveal a permittivity of 30 (GSO) and of 32 (LLO) and a bandgap above 5 eV. To understand the growth mechanism of the rare-earth oxides, the layer and especially the interface are investigated. First of all hexagonal GSO reveals a decomposition of Sc and Gd at the interface, so that it exhibits twice as much Sc than Gd, which reduces the length of the in-plane axis of the GSO and subsequently the lattice mismatch. Secondly, the grains are tilted in-plane, revealing a fibre texture with the c-axis as fibre axis perpendicular to the interface. Thirdly, the distance of the lattice planes at the interface is enhanced, revealing a distance of 3.1 Å. The SSO also reveals a fibre texture and an enhanced interface distance, thought the decomposition of the Sm and the Sc occurs in places. The hexagonal LLO reveals a fibre texture and a small decomposition.

For a novel NCFET a ferroelectric is placed in between the gate metal and the oxide of a MOSFET. The ferroelectric should exhibit a negative capacitance and in this way cause a voltage amplification, resulting in a subthreshold slope (SS) below 60 mV/dec. PLD grown ferroelectric HfO_2 with 5% Gd and HfO_2 with 5% Lu (HfLuO) reveal a remanent polarization of 12 µC/cm^2, while the HfO_2 with 5% Y, grown by atomic layer deposition, reveals one of 20 µC/cm^2 and a steeper hysteresis. HfLuO exhibits a pinched hysteresis at the initial state, if the sample is annealed at 500 °C, which could be related to an antiferroelectric phase. At an annealing temperature of 700 °C the HfLuO layer becomes ferroelectric.

Kurzfassung

Die kontinuierliche Verbesserung der Transistoren ist die Grundlage für die Steigerung der Rechenleistung. Für verbesserte Metalloxidhalbleiter (MOS) -Feld-Effekt-Transistoren (FETs) und andere Bauelemente werden geeignete Gate-Dielektrika benötigt, die eine hohe relative Dielektrizitätskonstante, gute Isoliereigenschaften wie eine große Bandlücke und eine gute Schichtqualität aufweisen. Zusätzlich werden neue Bauelementstrukturen wie der negative capacity FET (NCFET) entwickelt.

In dieser Arbeit werden die ternären Seltenerdoxide $GdScO_3$ (GSO), $LaLuO_3$ (LLO) und $SmScO_3$ (SSO) auf GaN mittels gepulstem Laserstrahlverdampfen (PLD) gewachsen. Diese Oxide zeigen eine hexagonale Phase, die vor einigen Jahren entdeckt wurde. Die Oxide haben eine große Gitterfehlanpassung zum GaN und befinden sich gemäß ab-initio-Rechnungen nicht im thermodynamischen Gleichgewicht. Die hexagonalen ternären Seltenerdoxide zeigen eine Permittivität von 30 (GSO) und 32 (LLO) und eine Bandlücke über 5 eV. Um den Wachstumsmechanismus der Seltenerdoxide zu verstehen, werden die Schicht und insbesondere die Grenzfläche untersucht. Zunächst zeigt das hexagonale GSO eine Entmischung von Sc und Gd an der Grenzfläche, so dass es doppelt so viel Sc wie Gd aufweist, was die Länge der Achse in der Ebene des GSO und folglich die Gitterfehlanpassung reduziert. Zweitens sind die Körner in der Ebene gekippt und zeigen eine Fasertextur, mit der c-Achse als Faserachse senkrecht zur Grenzfläche. Drittens wird der Abstand der Gitterebenen auf 3.1 Å an der Grenzfläche vergrößert. Das SSO zeigt auch eine Fasertextur und einen vergrößerten Grenzflächenabstand, jedoch tritt die Entmischung des Sm und des Sc nur stellenweise auf. Das hexagonale LLO zeigt auch eine Fasertextur und eine geringe Entmischung.

Für einen neuen NCFET ist ein Ferroelektrikum zwischen dem Gate-Metall und dem Oxid eines MOSFET angeordnet. Das Ferroelektrikum sollte eine negative Kapazität aufweisen und auf diese Weise eine Spannungsverstärkung bewirken, was zu einer Unterschwellenneigung (SS) kleiner als 60 mV/dec führt. PLD gewachsenes ferroelektrisches HfO_2 mit 5% Gd und HfO_2 mit 5% Lu (HfLuO) zeigen eine remanente Polarisation von 12 $\mu C/cm^2$, während das HfO_2 mit 3% Y, das mittels Atomlagenabscheidung gewachsen wird, eine remanente Polarisation von 20 $\mu C/cm^2$ und eine steilere Hysterese zeigt. HfLuO weist im Anfangszustand eine tailliert Hysterese auf, wenn die Probe bei 500 ºC geglüht wird, was mit der antiferroelektrischen Phase zusammenhängen könnte. Bei einer Glühtemperatur von 700 °C wird die HfLuO-Schicht ferroelektrisch.

Contents

1 Introduction

Computer, smart-phones and data processing significantly influence our daily life, so that the improvement of the computing power is a key for future life. Transistors, which are integrated in a large number on chips, are the basic device for all computing. Besides new transistor structures like tunnel field-effect-transistors or the fin field-effect-transistors, the metal-oxide-semiconductor field-effect-transistor (MOSFET) is still the most important device of semiconductor technology.
In this work the focus is on the development of new gate oxides for MOSFETs. The effort to make transistors smaller and more efficient has lead to the development of improved gate oxides in comparison to the common standard gate oxide HfO_2 in complementary metal-oxide-semiconductor (CMOS) technology and to the application of recently discovered physical properties of the oxides, i.e. ferroelectricity in HfO_2. In this work both aspects are explored: First, epitaxial ternary rare-earth oxides grown on GaN are investigated, to improve the electrical properties like the permittivity of gate dielectrics. Second, ferroelectric HfO_2 is analysed for the application in negative capacitance field-effect-transistors (NCFET).
Ternary rare-earth oxides are promising candidates for gate oxides, since a large relative permittivity (κ) and a large band gap is expected of those materials [1]. Schäfer et al. reported on the formation of a so far unknown hexagonal phase of $GdScO_3$ and $LaLuO_3$ on GaN. The lattice mismatch of the hexagonal phase is above 13% and ab-initio calculations show, that the determined phase is not thermodynamically stable, but still the existence of the phase is profen by X-ray diffraction and transmission electron microscopy. [2, 3, 4] The semiconductor GaN offers a large band gap of 3.4 eV [5], which results in a high breakdown voltage [6] and it can be employed for power electronic applications [7]. Thus, a combination of the ternary rare-earth oxides and GaN can become a worthwhile future device. To verify the ternary rare-earth oxides $GdScO_3$ and $LaLuO_3$ as suitable gate dielectric for GaN, the electrical properties like the permittivity and the band structure are determined. Furthermore, the structural properties of the hexagonal layers are analysed to understand the formation of this phase. Therefore, the layers are investigated by X-ray diffraction and, in particular, the interface structure is analysed by transmission electron microscopy.
For the new approach of negative capacitance field-effect-transitors (NCFET) suitable ferroelectric layers are required, that can be easily integrated in existing CMOS

technoloy. The standard gate dielectric HfO_2 transforms into an orthorhombic, ferroelectric phase by adding various elements like Si or Sr [8]. Since HfO_2 is already used as gate oxide, the implementation of ferroelectric HfO_2 into MOSFETs should be unproblematic. To transform a common MOSFET into a NCFET, an additional ferroelectric HfO_2 layer is mounted in between the gate oxide and the gate metal. In theory the ferroelectric exhibits a negative capacitance in the region of zero polarisation, which is stabilized by combining the dielectric gate oxide and the ferroelectric layer. The negative capacitance induces a voltage amplification of the applied gate voltage and thereby reduces the subthreshold slope of the device and thus the power consumption. [9, 10] To fabricate a working NCFET, stable ferroelectric HfO_2 is required, which exhibits a steep polarization switching. Hence the electrical and the structural properties of HfO_2 with 5% Gd, 5% Lu or 3% Y are investigated and optimized.

2 Experimental, Fundamentals and Details

The advances in computer technology affect every aspect of our lives, which is why the further development of the computing power is significant, so that more efficient transistors are required. The essential device structure for complementary metal-oxide-semiconductor (CMOS) technology is the metal-oxide-semiconductor (MOS) field-effect transistor (FET), whose improvement is very dependent on new gate oxides. In this work, the ternary rare-earth oxides $GdScO_3$, $LaLuO_3$ and $SmScO_3$ are evaluated as gate oxides, for more efficient transistors. Further ferroelectric HfO_2 thin films are analysed for negative-capacity FETs (NCFET) (see section 4.1.1.3), which are MOSFETs with an additional ferroelectric layer. The investigated gate oxides are key components for further scaling and power reduction of future FETs. In order to achieve these goals, analysis of the electrical, ferroelectrical and structural properties of the rare-earth oxides and HfO_2 samples is required. In the following the applied experimental techniques are described: First the macroscopic techniques, secondly, the microscopic techniques and finally the device fabrication are explained. The growth and processing of rare-earth oxides and HfO_2 are elaborated in 3.1.3 and 4.1.2, respectively.

2.1 Macroscopic techniques

In this section the macroscopic techniques are elucidated including the electrical characterization, X-ray diffraction, X-ray photoelectron spectroscopy, atomic force microscopy and scanning electron microscopy.

2.1.1 Capacitance voltage measurements

To determine the capacity and further the permittivity (κ) of the oxides, capacitance voltage (CV) measurements were performed using a *E4980A Precision LCR Meter* from *Keysight Technologies*. Two metal top contacts with an area ratio of 400 ($4\ mm^2 : 0.01\ mm^2$) were contacted, whereby the high potential was connected to

the small pad and the low potential was connected to the large pad. Since capacities are proportional to the area and they are added reciprocally the capacity of the large pad is negligible. A DC voltage with an overlying AC voltage (V_{Ac}) of 50 mV at a frequency (ω) of 100 kHz is applied. The capacitive current (I_{Cap}) was measured and the capacitance (C) was determined from the relation $I_{Cap}/V_{Ac} = \omega C$. The capacity normalized to the area is plotted over the DC voltage. From the measured capacity the Capacitance Equivalent Thickness (CET) is calculated by:

$$CET = d = \frac{\kappa_{\mathrm{SiO_2}} \epsilon_0 A}{C}. \tag{2.1}$$

Here d is the calculated layer thickness of an SiO_2 layer exhibiting the same capacitance, $\kappa_{\mathrm{SiO_2}}$ the permittivity of SiO_2, ϵ_0 the vacuum permittivity, A the area of the capacitor and C the capacity. The calculated CET was plotted against the actual layer thickness of the oxide for samples with varying thickness (see Figure 3.12). Thus, a linear trend was visible and from the regression line the permittivity (κ) of the oxide layer was calculated by:

$$\kappa = \frac{3.9}{m}, \tag{2.2}$$

where m is the slope of the regression line and 3.9 is the permittivity of SiO_2.

2.1.2 Current voltage measurements

Resistivity, breakthrough voltage and leakage current of the oxides were determined by current-voltage measurements using a *4200-SCS* from *Keithley Instruments Germany*. The high potential was connected to the small pad (0.01 mm^2) and the low potential was connected to the large pad (4 mm^2). A DC voltage was applied and the current was measured. Since resistivity is inversely proportional to the area and they are added in series, the resistivity is mainly caused by the small pad.

2.1.3 Polarization voltage measurements

Besides the capacitance and the resistance of the ferroelectric capacitor the coercive field strength (E_c) and the remanent polarization (P_r) are important properties of the ferroelectric capacitor (compare section 4.1.1). The ferroelectric capacitors were investigated by an *AixACCT TF2000* from *aixACCT Systems GmbH*. The easiest way to measure the polarization is by the Sawyer-Tower Circuit as displayed

in Figure 2.1 (a). The ferroelectric capacitor (C_{ferro}) is connected in series with a reference capacitor (C) (s1 closed, s2 open), which has a 100 times higher capacity compared to C_{ferro} to assure that the main voltage drop is across C_{ferro}. As impulse a triangular voltage is applied and an oscilloscope measures the voltage at the reference capacitor (V_{ref}) against the applied voltage. Since the charge at the ferroelectric capacitor (Q_{ferro}) is the same as at the reference capacitor (Q_{ref}), the polarization (P) can be calculated from the reference capacity (C) and V_{ref}:

$$Q_{ferro} = \frac{C_{ferro}}{V_{ferro}} = \frac{C}{V_{ref}}, \tag{2.3}$$

where V_{ferro} is the voltage drop over the ferroelectric capacitor. A measured polarization voltage (PV) curve looks like a ferroelectric hysteresis, if there are high leakage currents. Therefore, the ferroelectric capacitor is afterwards connected to a resistance and the displacement current is analysed in respect to the applied voltage by the oscilloscope (s1 open, s2 closed see Figure 2.1 (a)). A ferroelectric capacitor exhibits two current peaks, which correspond to the switching of the polarization, while leakage currents exhibit an increase in the current, but no peaks. The disadvantage of the Sawyer-Tower method is, that the precision of the measurement is strongly influenced by the reference capacitor and the measurement accuracy is influenced by parasitic capacities.

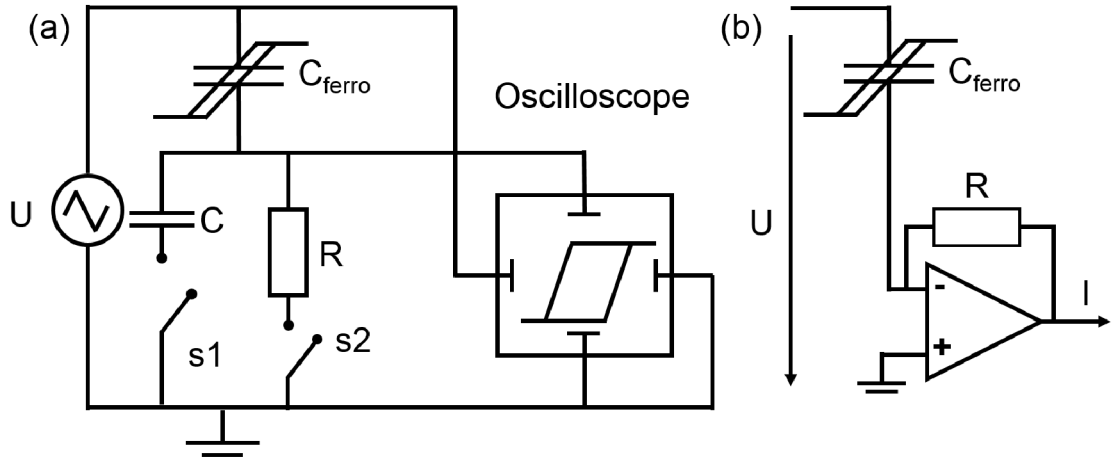

Figure 2.1: Scheme of the PV measurement set-up of a Sawyer-Tower Circuit (a) and virtual ground set-up (b). [11]

To overcome this drawbacks the virtual ground set-up was developed shown in Figure 2.1 (b). The ferroelectric capacitor is connected to an inverse entrance of the

operational amplifier, while the other entrance of the operational amplifier is connected to ground. Due to the small voltage difference between the entrances, the inverse entrance is a virtual mass. At the exit of the operational amplifier a resistance is fed back to the entrance respectively to C_{ferro}. Thus, the whole current flows over the resistance and an integrator calculates the polarization from the measured charge. The explained measuring principle is used in the *AixACCT TF2000.* Four separated triangle voltage impulses are applied (Figure 2.2). From the four cycles only the second and fourth cycle are used to determine the hysteresis, while the other cycles just polarize the sample before the measurement. Due to relaxation, the polarization at the beginning differs from the polarization at the end of the triangle voltage impulse. Thus, the polarization voltage curve and the current voltage curve were determined from the second half of the second and fourth triangle voltage impulse. Beside the polarization-voltage measurement the samples are characterized by fatigue. Therefore, the hysteresis of the ferroelectric capacitors is measured at the initial state. Afterwards, a defined positive and negative voltage is applied 10^4 times and then the hysteresis is measured again. This procedure is repeated until failure of the device, which allows to determine the durability of the ferroelectric capacitors. [11]

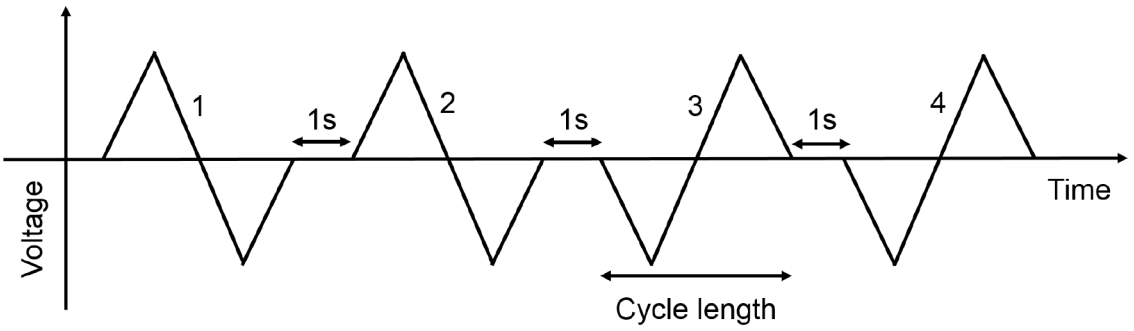

Figure 2.2: Triangular excitation signal for hysteresis measurement. [11]

2.1.4 X-ray diffraction

Crystalline layers, polycrystalline layers and amorphous layers can be characterized by elastically scattered X-rays. The monochromatic incident beam is scattered by the lattice planes, the surface or the interface to a measurable signal, depending on the orientation of the X-ray source, the sample and the detector. Different methods are applied depending on the investigated oxide and the desired information. Layer thickness and roughness are investigated by X-ray reflection (XRR), while X-ray

diffraction (XRD) is used to extract the crystal structure of a single crystal or an epitaxial grown layer. The crystal structure of polycrystalline layers is analysed by grazing incidence X-ray diffraction (GIXRD) and the layer quality and growth are evaluated by a reciprocal space map (RSM). Measurements were performed using a *Philips X'Pert* four cycle diffractometer with a Cu K_α X-ray tube with a wave length of 0.15418 nm. The measured intensity is described by the Bragg law for constructive interference [12]:

$$2dsin\Theta_B = n\lambda \text{ [12]}, \tag{2.4}$$

where d is the lattice plane distance, Θ_B is the Bragg angle, n is an integer and λ is the wavelength of the X-ray. The X-rays, diffracted by the lattice planes of the crystal, interfere, whereby the path difference depends on the angle of the detector and the X-ray source, generating a large detectable intensity, if the X-rays interfere constructively. The lattice planes can be described by the Miller Indizes. In Figure 2.4 the XRD set-up is shown. Φ is the tilt of the sample, ω refers to the angle of the incident beam in relation to the sample surface, Ψ is the rotation normal to the sample surface, and 2Θ is the angle of the diffracted beam relative to the incident beam. [12]

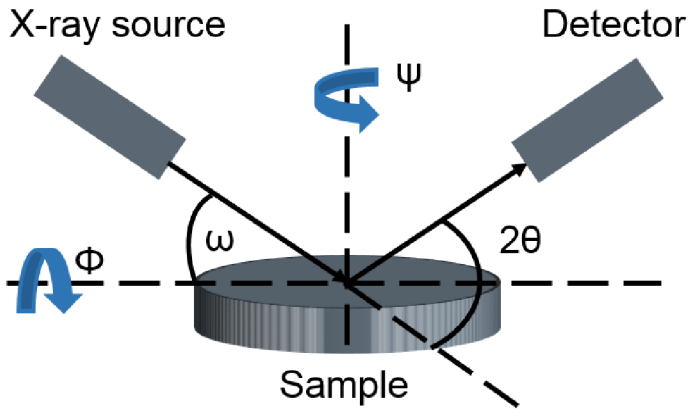

Figure 2.3: Scheme of the XRD set-up showing the sample, the X-ray source and the detector. Φ is the tilt of the sample, ω refers to the angle of the incident beam in relation to the sample surface, Ψ is the rotation normal to the sample surface, and 2Θ is the angle of the reflected beam relative to the incident beam. [12]

XRD was used to determine the crystal structure of the epitaxial grown layers. Therefore, ω and 2Θ were adjusted to fulfil $\omega = 2\Theta$ and the measured intensity is plotted against 2Θ. The lattice distance was calculated by the Bragg law (equation

2.4). Only lattice planes that are orthogonal to the axis of incidence diffract the X-rays into the detector, so to determine various lattice planes the sample is tilted by Φ and ω. Further analyses of the sample by XRD are described in the following. For a certain determined reflection 2Θ and ω were fixed and the sample was tilted around the surface normal (Ψ). In this way the symmetry conditions of the crystal could be determined and conclusions on the crystal were drawn. For example a sixfold symmetry can result from a hexagonal structure or from twined cubic structures. To determine the crystal quality, rocking curves were measured, whereby 2Θ was kept constant and ω was varied in between 1°-3°. A perfect crystal would reveal one sharp peak at a fixed ω, 2Θ combination, but structural defects in the epitaxial grown layers produce a broadened peak. Thus, the broadening of the peak, specifically the full width half maximum (FWHM) of a reflection is a measure for the crystallinity. [12]

2.1.5 Reciprocal space map

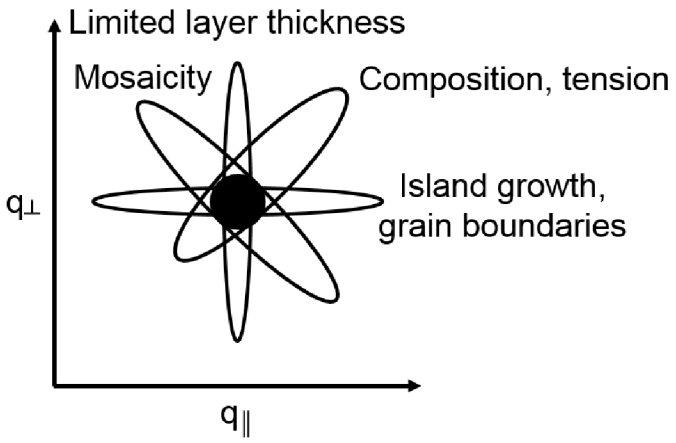

Figure 2.4: Scheme of a reciprocal space map and the possible broadenings and their cause. [12]

A reciprocal space map (RSM) was measured to determine the crystal quality in-plane and out-of-plane. RSM is a two-dimensional measurement around a known reflection, whereby multiple $\omega - 2\Theta$ scans by alternated incident beam angles ω are measured. The measurement is transformed into the in-plane $q_{\parallel}$ and out-of-plane $q_{\perp}$ coordinates by the formulas 2.5 and 2.6 [12]:

$$q_{\parallel} = R_{Ewald}(cos(\omega) - cos(2\Theta - \omega)). \tag{2.5}$$

$$q_\perp = R_{Ewald}(sin(\omega) - sin(2\Theta - \omega)). \tag{2.6}$$

Here R_{Ewald} is the radius of the Ewald sphere in the reciprocal space. The intensity is plotted against the calculated $q_\parallel$ and $q_\perp$. A perfect, endless crystal would exhibit a high intensity at an specific $q_\parallel$ and $q_\perp$. Due to imperfections in the crystal the reflection is broadened. The broadening of the reciprocal lattice point provides conclusions about the layer quality and the layer growth. A horizontal broadening is due to island growth or grain boundaries, while a horizontal broadening is related to the limited layer thickness. Broadening in the direction of the scattering vector is related to tensions and changes in the composition and a perpendicular broadening to the scattering vector is related to mosaicity. [12]

2.1.6 Grazing incidence X-ray diffraction

By grazing incidence X-ray diffraction (GIXRD) thin polycrystalline layers were investigated. To improve the signal to noise ratio of a thin layer, small incident angles ($< 3°$) are employed. This way the X-rays pass mainly through the near-surface region, while the signal of the substrate is suppressed. The detector is shifted around the sample, so that different crystallographic orientations of the layer are explored. Thus, the grains fulfil the Bragg condition at a certain point, independent of their orientation. By GIXRD different crystals can be distinguished by their characteristic peaks in a polycrystalline thin film. Since only a small part of the thin film fulfils the Bragg condition, the intensities are lower compared to XRD. The resolution is limited by the chromatic aberration of the X-ray source, precluding the differentiation of similar crystal structures. [12] For GIXRD measurements employed here, ω was fixed to 2°.

2.1.7 X-ray reflectivity

X-ray reflectivity (XRR) was used to determine the layer thickness and the roughness at the surface and at the interface to the substrate of the grown oxide layers. XRR is an applied $\omega - 2\Theta$ scan at small angles ranging from 0-10° [12]. Due to the small angles, the reflections are not caused by the lattice spacings, but by the interfaces. The reflection of the incident X-ray by interfaces is described by the Fresnel equations, which elucidate the reflection and transmission of electromagnetic waves at an interface. At the beginning of the measurement ($\omega \sim 0$) the incident beam is parallel to the sample surface and gets reflected by the layer with increasing angle. At the critical angle of the layer some X-rays penetrate the layer and are partially

reflected by the substrate. The reflected beams of the layer and the ones reflected by the substrate interfere and cause measurable oscillations, with a width depending on the path difference of the X-ray reflected by the oxide and the X-ray reflected by the substrate. Since the layer thickness is related to the path difference, the layer thickness can be determined from the width of the oscillations. Further, the roughness of the interfaces causes diffuse scattering, inducing a reduction of the measured intensity. Therefore, roughness of the interfaces are related to the steepness of the intensity reduction. [12] The measured intensity is plotted against the scattering vector q.

2.1.8 X-ray photoelectron spectroscopy

X-ray photoelectron spectrocscopy (XPS) is a widely used surface analysis technique to determine non destructively the binding energies and hence chemical composition of thin films and surfaces. The investigated surface is irradiated with soft X-ray photons, which interact with the surface atoms. During this process the energy of the X-ray photon is transferred to an electron in the core level and the electron is ejected. The electron leaves the atom with a specific kinetic energy (E_{kin}), which is detected. The kinetic energy of the electron depends on the X-ray photon energy ($h\nu$) and the binding energy of the electron (E_{bin}) and is described by the following equation [13]

$$E_{kin} = h\nu - E_{bin} - \Phi_S \text{ [13]}, \tag{2.7}$$

where Φ_S is a small, almost constant work function. From the XPS spectra an elemental analysis is possible, because the binding energy is unique for each atom. Further, the binding energy of the electrons is influenced by the chemical environment, so that changes in the kinetic energy, carry chemical information. The technique is surface sensitive, i.e. chemical information are only acquired from the surface and from the region few nm underneath the surface. The electrons ejected by the X-ray photons exhibit a certain amount of kinetic energy, which is reduced by inelastic scattering with atoms. If the electron reaches the surface, the residual kinetic energy must be larger than the binding energy, to leave the sample and reach the detector. Hence, the distance an electron can travel without scattering is an important characteristic of a sample, which is called inelastic mean free path (λ_{free}). Most signal of the XPS spectra comes from the escape depth $d = 3\lambda_{free}$, which is roughly 10 nm. [13] The samples for XPS investigation were bare substrates or exhibited a 4 nm thick oxide layer.
The characteristic band alignment of an oxide on a semiconductor is a key property and was identified by the method of Miyazaki [14]. The bandgap of the oxide and the semiconductor, and the valence band offset (VBO) are determined and subsequently

the conduction band offset is calculated. The bandgap (E_{gap}) was determined from the shifted onset of the electron loss peak at higher binding energy from the peak (as shown in Figure 3.17 (a)). Therefore, the intersection of the average background at the base of the peak and the linear fit to the electron loss peak was identified, which was the onset of energy dispersion by inelastic collision. The bandgap was calculated from the onset of energy dispersion by inelastic collision (E_{onset}) and the binding energy at the maximum of the peak ($E_{peakmax}$). [14]

$$E_{gap} = E_{onset} - E_{peakmax} \text{ [14]}. \tag{2.8}$$

The VBO was ascertained by the two onsets at low binding energies, which resulted from the minima of electron excitation of the valence band of the oxide and the semiconductor. The onset was defined as the intersection of the linear regression of the onset with the background at 0 eV (see Figure 3.17 (b)). [14]

$$VBO = E_{VB\,Oxide} - E_{VB\,Semiconductor} \text{ [14]}, \tag{2.9}$$

where $E_{VB\,Oxide}$ and $E_{VB\,Semiconductor}$ are the onset of the oxide and the semiconductor, respectively. In order to detect a signal from the oxide as well as from the semiconductor a thin oxide layer (~10 nm) is obligatory, because of the small escape depth of the electrons [14]. The XPS measurements were done at the Department of Materials Science and Engineering at the Technion. For XPS measurements a *Thermo VG Scientific Sigma Probe* with a monochromated Al K_α source with an energy of 1486.6 eV was used. The collector was a high angular acceptance electrostatic lens with an imposed pass energy of 50 eV, adjusted 20°-80° relative to the sample normal. The detector was an energy and angular multi channel 180° spherical analyser.

2.1.9 Atomic force microscopy

Atomic force microscopy (AFM) was used to derive an image of the surface morphology and to evaluate the roughness of the substrates and the layers. An oscillating cantilever with a narrow tip is raster-scanning over the surface at very low distance. The force between the surface and the tip results in a deformation of the cantilever, which is measured by the displacement of a laser beam, that is focused on the cantilever. When the tip gets closer to the surface, the Van-der Waals forces change the oscillation behaviour. In the ideal case the tip is an individual atom, that interacts, with the atoms of the surface. A feedback loop is used to keep the tip at a constant distance to the surface and maintain a free oscillation. The position and the height of the cantilever is controlled by piezo elements, so that the known position and

height is used to from an AFM image, representing the height profile of the surface. [15]
In this thesis a *Digital Instruments Nanoscope IIIa AFM* in tapping mode was used.

2.1.10 Scanning electron microscopy

Scanning electron microscopy (SEM) is used to investigate the surface of the substrates and the samples. In a high vacuum an electron beam is formed at a field emission cathode, which is raster-scanned over the sample surface. The primary electrons of the electron beam, generate secondary electrons, that are detected. The intensity of the secondary electrons is plotted against the position of the electron beam and in this way an image of the sample surface is created. Secondary electrons are only emitted from the first few nm of the sample, so that the sample topography is displayed. SEM achieves a high resolution of few nm. In this thesis a *SEM Gemini 1550* from the company *Zeiss* was used.

2.2 Transmission electron microscopy

The local structure and composition of the oxide layer is investigated by transmission electron microscopy (TEM). The invention of the first TEM by Max Knoll and Ernst Ruska allowed surpassing the resolution of a light microscope. In our days a wide range of microscopical techniques even on the atomic scale is available, e.g. imaging, compositional and bonding analyses, measurement of local electrical and magnetic fields, studies under external stimuli, to name a few. All of these techniques make use of the signals produced, when a (coherent) electron beam is elastically or inelastically scattered by the sample.
In this thesis various diffraction techniques, making use of the elastically scattered electrons, are employed, in order to access the crystal structure. High resolution (scanning) microscopy is used to investigate the atomic structure, in particular the interface between the substrate and the layer. Furthermore, energy dispersive X-ray analysis is performed to measure the local chemical composition. Finally, the transmission of an electron beam through the material requires a thin (100 - 10 nm) specimen. The preparation of such TEM specimen is described in the following.

2.2.1 Preparation of TEM specimen

For transmission electron microscopy (TEM) high-quality images and analysis, thin samples, i.e. 10-100 nm, were required. TEM samples were fabricated by focused ion beam (FIB) using a *Helios NanoLab 400S* or wedge grinding using a *MultiPrep* polishing system from *Applied High Tech*. Before cutting a FIB lamella an Au layer was sputtered on top of the sample for protection during cutting. Afterwards the lamella was cut at 30 keV and was polished at 5 keV with Ga ions. A standard lamella exhibits a thick area, which is attached to the grid. This thick area gets thinner stepwise, until the lamella exhibits an electron transparent region. Standard lamella of the rare-earth oxides could not be thinned to electron transparency, because they used to break or the oxides were torn off by the tension in between the substrate and the oxide layer during the sample thinning. Therefore, an improved lamella structure was developed to stabilize the oxide. Three different approaches were tested and evaluated. Since the oxide was stable, if the lamella was thicker, in the first approach the electron transparent area was reduced in length and the size of the bulk area, attached to the grid, was kept larger. During thinning of the lamella the oxide was still torn off. For the second try at both ends of the lamella similar bulk areas were added with an smaller electron transparent region in between. The lamella was only attached to the grid on one side, while the bulk area standing free, was only hold by the thin electron transparent area. During thinning of the lamella the electron transparent region became too weak, to hold the free standing bulk area and broke during thinning or investigation. The final design used an asymmetric shape of the lamella, with a large bulk area attached to the grid and a smaller, free standing bulk area at the end of the lamella (see Figure 2.5 (a)). In addition, the electron transparent area for investigation was minimized down to 5 µm. In this way the oxide was stabilized and breaking of the lamella during investigation and thinning was prevented. The final thinning and polishing of the samples was done with the aid of low energy thinning by a *Fischione NanoMill Model 1040* by 900 eV and 500 eV, respectively. The sample was polished for half the time at 500 eV as it was thinned at 900 eV.

Samples were also prepared by wedge grinding, see Figure 2.5 (b) and (c). Here, a wedge is formed, which becomes thinner and in the ideal case electron transparent at the edge. To prepare a cross section sample by wedge grinding two pieces with a size of 0.8 x 2 mm^2 were cut out of the sample by a diamond saw. The sample pieces were cleaned with a cotton bud soaked in acetone, which was gently swept over the oxide surface. Afterwards the top side of the sample pieces were glued together with a small amount of *Gatan G1* glue with the oxide layers facing each other. The glued sample was pressed together in a bench vice and annealed for 15 minutes at 200 °C to harden. The sample stack is shown in Figure 2.5 (b). The

holder of the *MultiPrep* grinding machine was heated to 150 °C and a little bit of wax was melted on the holder. A temperature above 150 °C induced bubbles in the wax, which destabilized the sample. The sample was placed on the wax and was gently pressed against the holder. Afterwards, the sample holder was fixed to the *MultiPrep* and the sample was ground by abrasive papers with decreasing roughness and rotation speed until the remaining sample thickness was 250 µm. To remove all marks of the previous abrasive paper, three times the roughness of the previous abrasive paper had to be excavated. The roughness of the abrasive papers and the rotation speed are shown in table 2.1.

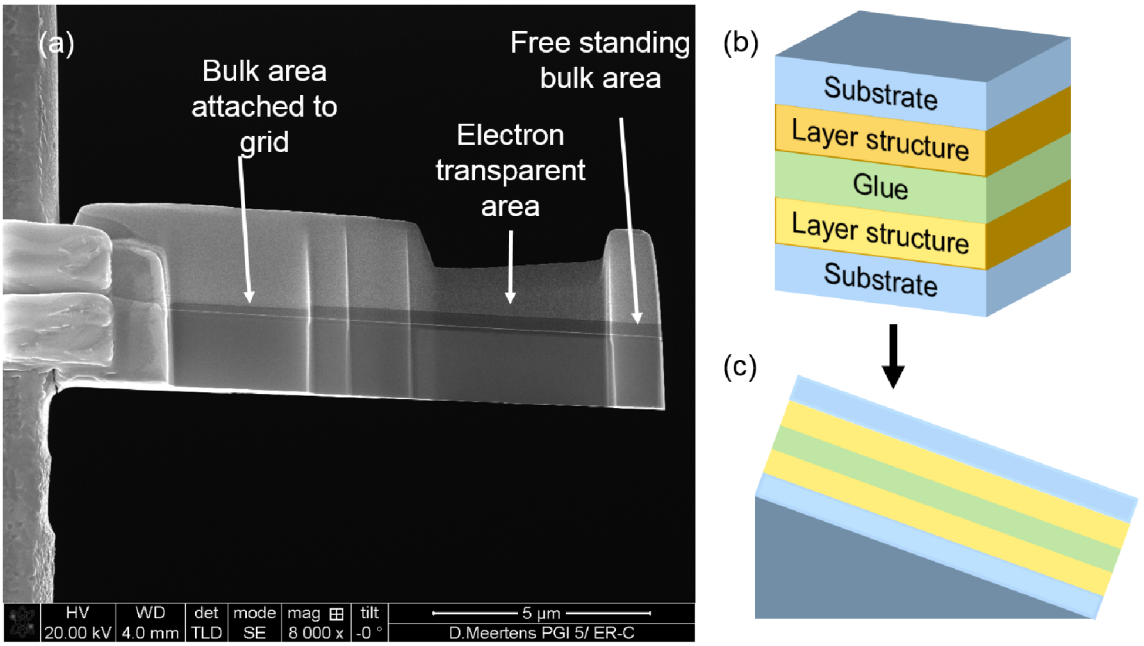

Figure 2.5: Scanning electron microscope image of the improved, asymmetric lamella with stabilization bulk areas for rare-earth oxides (a). Structure of the sample for wedge grinding (b) and a finished wedge (c).

In a last step the sample was polished by a Si polishing compound on a felt cloth. The rotation was 5 rpm and the felt cloth was kept humid by distilled water. Afterwards the sample was taken from the holder with tweezers and the holder was cleaned from the wax by acetone. An new small drop of wax was put on the holder and the sample was fixed to the holder, after it was turned up side down. The holder was tilted by 3° by the micrometer callipers at the *MultiPrep*. Subsequent, the sample was ground again with the same abrasive papers and the Si solution until electron transparency was achieved. During the whole process the spindle load was set to the

unitless value 2. After grinding, the holder was put into acetone, to solve the wax. Underneath the holder a filter paper was placed, on which the sample fell, when the wax was solved. A scheme of the finished wedge is shown in Figure 2.5 (c). To place the sample in a TEM, the sample had to be fixed to a Mo-ring. The filter paper was taken slightly tilted from the acetone with tweezers, so that residual acetone could drain. The Mo-ring was clamped into reverse tweezers and a very small drop of *Gatan G1* glue was placed on the edge of the ring with a thin cat hair. Afterwards, the ring was flipped and the sample was picked up with the glue on the ring. The tweezers, holding the ring with the sample on it, was slowly heated up to 200 °C, to prohibit bubbles in the glue. The grid samples were finally thinned and polished by the *Fischione NanoMill Model 1040* in the same way as the lamella.

Table 2.1: Parameters for wedge grinding.

Step	Grain size [µm]	Rotation speed [rpm]
1	15	70
2	6	50
3	3	25
4	1	20
5	0.1	15

2.2.2 Electron Diffraction techniques

In this thesis selected area diffraction (SAED), nanobeam electron diffraction (NBED) and automated diffraction tomography (ADT) are applied, to determine the crystal structure, space group and atom positions in the unit cell.
Diffraction is mathematically described by the diffraction of the initial electron wave ($\vec{k_0}$) into the diffracted one ($\vec{k_D}$), which results in a change described by the vector $\vec{K}$. The diffraction is elastic, so that $|\vec{k_0}| = |\vec{k_D}|$. If $\vec{k_0} + \vec{k_D} = \vec{K} = \vec{g}$, whereby $\vec{g}$ is the diffraction vector of a any lattice plane, the Laue condition is fulfilled and hence the electrons interfere coherently and a diffraction spot becomes visible. The diffracted beams form the "Ewald sphere" and all lattice planes with a $\vec{g}$ on the sphere contribute to the diffraction pattern as shown in Figure 2.6. By rotating the Ewald sphere different reciprocal planes with a different set of $\vec{g}$ are observed. In contrast to XRD the Ewald sphere is almost planar due to its huge radius. The electron wave length at 200 kV is 2 pm, revealing a radius of the Ewald sphere of 540 nm^{-1}. Due to the limited thickness (t) of the TEM specimen, the diffraction spots exhibit a rod-like shape, where the length of the rod scales with $\frac{1}{t}$. Hence, diffraction spots become visible, even if the Ewald sphere deviates by the so called excitation error ($\vec{s}$) from the pattern of the "ideal" spot (see Figure 2.6) [16] and

consequently, the Laue condition becomes

$$\vec{g} + \vec{s} = \vec{k_0} + \vec{k_D} \text{ [16].} \tag{2.10}$$

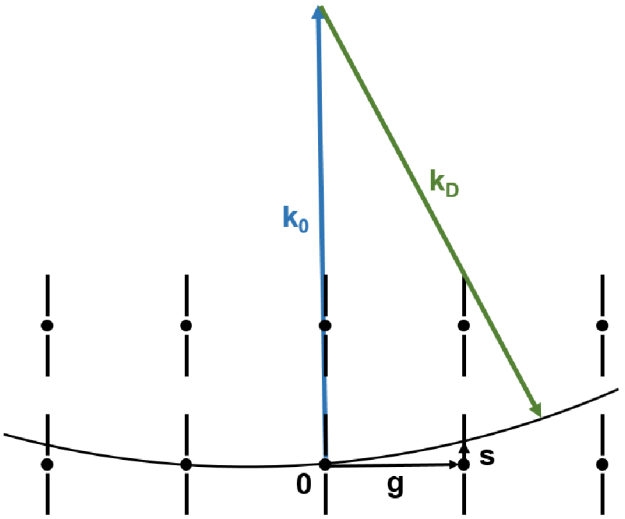

Figure 2.6: Scheme of the Ewald sphere displaying the k-vector of the incident wave (k_0) to the k-vectors of the diffracted wave (k_D) and the origin of the reciprocal lattice (O). The diffraction spots are elongated, due to the excitation error (s). In this way diffraction spots, that do not fulfill the Laue condition, contribute to the diffraction pattern. [16]

The intensity and the position of the diffracted beams depends on the crystal structure and types of atoms. In addition, the strong interaction of the electrons with the sample gives rise to dynamical scattering, i.e. the electron waves may be scattered multiple times. [16]

Selected area electron diffraction (SAED) was applied to determine the phase and crystal structure of the grown layer. The SAED patterns were recorded using a selected area aperture with a diameter of 4000 nm. For SAED a *FEI Tecnai G2 F2012* operated at accelerating voltage 200 kV was used [17].
Nano beam diffraction (NBD) is a type of diffraction, that is acquired in STEM mode. NBD technique uses a nearly parallel electron beam, achieved by lowering down the condenser aperture C_2 size down to about 10 µm or by using a three-condenser system. The convergence angle can be reduced to 0.1 mrad, if a 1 µm C_2 is used. NBD forms diffraction spots at the back-focal plane of the objective lens by focusing the beam on the specimen, with that the lattice parameters can be

determined. [18]

Automated diffraction tomography (ADT) was employed to confirm the unit cell, determine the space group and finally retrieve the atom positions in the hexagonal $GdScO_3$ and $LaLuO_3$ [19, 20]. The ADT measurements were performed by Dr. Ute Kolb and Sergi Plana Ruiz from the Institut für Physikalische Chemie in Mainz. In a FEI Tecnai F30 S-Twin at 300 kV, STEM mode was applied to image the crystal and nano beam diffraction (NBD) was used to record the electron diffraction pattern (DP). Because of the STEM imaging instead of TEM imaging the microscope is in diffraction mode all the time. In this way, the "microprobe" beam setting available in FEI microscopes was used for STEM imaging and diffraction pattern acquisition, which has the advantage of less convergent angle, but the disadvantage of higher beam probe sizes compared to the "nanoprobe" beam setting (usually used for high-resolution STEM imaging). The sequential ADT acquisition steps are the following: The holder is tilted to the initial alpha angle, a STEM image is recorded, the beam is stopped and positioned to the region of interest, a diffraction pattern is acquired. Then, the alpha tilt is increased usually by 1° and the previous steps are repeated until the final angle is reached. The key point of ADT is the high completeness of the acquired reciprocal space volume and the possibility to acquire diffraction patterns of off-zone axis, which minimizes the dynamical effects on the intensity of the reflections. The use of a precessed electron beam allows more reduction of the dynamical effects and increases the number of reflections for each diffraction pattern, that in turn increase even more the completeness of the diffraction volume. However, dynamical effects cannot be fully eliminated and this hinders the structure solution, when high dynamic materials such as metals or semiconductors are analysed. The ADT comprises three steps: 1. Data acquisition by recording diffraction patterns at different sequential alpha tilt angles. 2. Data processing to reconstruct the reciprocal space, find the unit-cell, determine the space group and extract the intensity for each reflection. 3. Structure analysis contains structure solution and refinement. In this work only the first two steps were accomplished and in the future further investigations will be carried out to elucidate the structure. The investigated crystal was tilted from -60° to 60° with a tilt step of 1° and a precision angle of 1°. A spot size 6, gun lens 4 and a 10 µm C2 aperture were used, to set a beam probe size of around 5 nm and a convergence angle of 0.5 mrad. This configuration was used for STEM imaging and diffraction pattern acquisition. The sample was investigated with an electron dose rate of around 1800 $e^-/Å^2 s$.

2.2.3 Imaging techniques

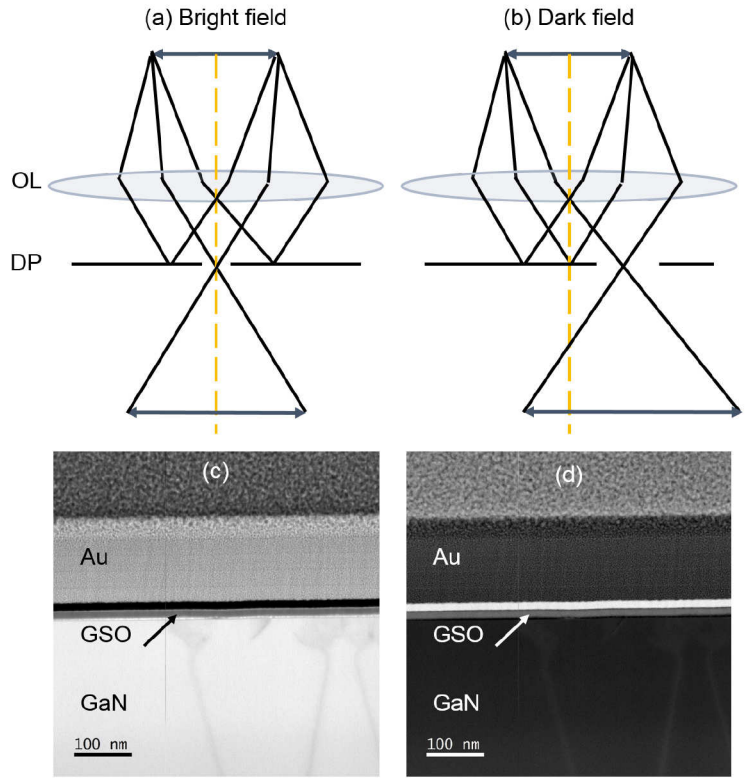

Figure 2.7: Scheme of the microscope set-up for a bright field image (a) and a dark field image (b). In the image the objective lens (OL) and the diffraction plane (DP) are shown. [16] Bright field (c) and dark field image (d) of GSO on GaN.

Transmission electron microscopy (TEM) exhibits a multitude number of imaging techniques, which offer the possibility to investigate the specimens in the range from a few µm down to a several hundred of pm. In this work TEM was used to investigate the interface quality, the crystal structure and the grain size of polycrystalline layers. In the following the applied techniques bright field TEM, dark field TEM and scanning TEM are elucidated. In **bright field (BF)** TEM a parallel illumination of the specimen is adjusted and the central beam ($\vec{k_0}$) is selected by the aperture as shown in Figure 2.7 (a) and (c). BF TEM was used to investigate the interface and the grown devices. [16, 21]
In **dark field (DF)** TEM only the diffracted beams ($\vec{k_D}$) contribute to the image, while the direct beam is excluded (see Figure 2.7 (b) and (d)). The diffracted beam is chosen by the aperture, so that only specific lattice planes, that fulfil the Laue

condition contribute to the image. In polycrystalline layers the grains and consequently the lattice planes reveal different orientations. By choosing a certain part of the diffraction pattern only specific grains contribute to the image and appear bright, offering the possibility to determine the grain size. [16, 21]
In contrast to TEM images or DP, for **scanning transmission electron microscopy (STEM)** the incident beam is focused on the specimen and scanned over it [16, 22]. The principle set-up of a TEM in scanning mode is shown in Figure 2.8, displaying the position of the EDX detector and the charge-coupled device (CCD) and high-angle annular dark field (HAADF) detector.

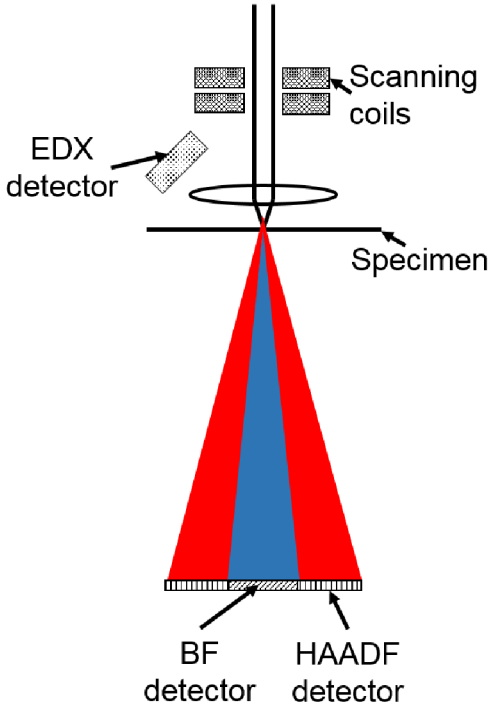

Figure 2.8: Scheme of microscope set-up for STEM mode, showing scanning coils, specimen, EDX detector, bright field detector (BFD) and high-angle annular dark field (HAADF) detector. [16]

The electrons are scattered by the atomic nuclei, whereby the scattering angle depends on the atomic number (Z). The scattering of the electrons by the nucleus is described by Rutherford scattering ($\sim Z^2$), but it is slightly reduced by the atom's electron cloud ($\sim Z^{1.7}$). For each position of the beam a installed high-angle annular dark field (HAADF) detector records electrons, scattered at least 50 mrad. [16, 22]
STEM investigations are done using an *FEI Titan G2 80-200 CREWLEY* equipped with a Schottky type high-brightness electron gun (FEI X-FEG), a Cs probe correc-

tor (*CEOS DCOR*), and an in-column Super-X energy dispersive X-ray spectroscopy unit (*ChemiSTEM technology*). The resolution is about 0.8 Å. [23] Depending on the investigated specimen, the accelerating voltage was either 80 keV or 200 keV. In the STEM multiple, circular detectors are installed recording electrons scattered at different angles. A bright field detector on the optic axis and an angular dark field detector are available in the microscope. The in-column Super-X energy dispersive X-ray spectroscopy unit was used for energy dispersive X-ray (EDX) analysis.

2.2.4 Energy dispersive x-ray spectroscopy

Spectrometry utilizes the signals resulting from inelastic scattering of the beam electrons with the specimen. During inelastic scattering the beam electrons partially transfer their energy to the specimen, resulting in a whole range of signals with information about the specimen's chemistry, bonding and dielectric function. Energy-loss electron spectrometry, characteristic X-rays and secondary electrons are the most important signals. In this work the specimens are investigated by energy dispersive X-rays, so that their formation is explained. A high-energy electron beam penetrates into the inner-shell of an atom and interacts with an inner-shell electron. If a critical amount of energy from the electron beam is transferred to the inner-shell electron, it is ejected and a hole in the shell is formed. The ionized atom has more energy than at the ground state and to return to this state, the hole is filled with an electron from the outer shell. Thereby an X-ray or an Auger electron is emitted, revealing a characteristic energy, which depends on the two electron shells involved. The X-ray is detected and from its energy the type of atom can be distinguished. The shells of an atom are described by K,L,M, etc. from the innermost to the outermost shell. The emitted X-ray is named after the shell, from which the electron is ejected, and by the distance to the shell, the hole is filled from. X-rays emitted, while refilling the shell with an electron from the next shell, get the index α, and those filled from the shell after the next shell get the index β and so on. Thus, an X-ray emitted by filling a hole in the K shell from the M shell is named K_β. To remove an electron from the innermost shell consumes more energy than an electron from an outer shell. Further, atoms with a higher mass exhibit more protons, so that the binding of the electrons is stronger. So the energy of the X-rays increases with the atomic number and for shells further inside the atom. A quantitative X-ray analysis can be performed by the the Cliff-Lorimer ratio technique, by which the ratio of the measured X-ray intensities of different elements is related to the concentration ratio. The weight percent of the elements A (C_A) and B (C_B), is related to their X-ray intensities (I_A and I_B) by the Cliff-Lorimer equation [16].

$$\frac{C_A}{C_B} = k_{AB}\frac{I_A}{I_B} \quad [16], \tag{2.11}$$

where k_{AB} is the Cliff-Lorimer factor [16]. EDX investigations in the STEM are done using an *FEI Titan G2 80-200 CREWLEY* equipped with a Schottky type high-brightness electron gun (FEI X-FEG), a Cs probe corrector (*CEOS DCOR*), and an in-column Super-X energy dispersive X-ray spectroscopy unit (*ChemiSTEM technology*) [23].

2.3 Growth and device fabrication

This section contains the applied processes for device fabrication. A general description of the processes is given, while the parameters for sample preparation are listed in section 3.1.3 and section 4.1.2 for the ternary rare-earth oxides and the ferroelectric layers, respectively.

2.3.1 Pulsed laser deposition

Pulsed laser deposition (PLD) was used to deposit HfO_2 with 5% Lu (HfLuO), HfO_2 with 5% Gd (HfGdO), $GdScO_3$ (GSO), $SmScO_3$ (SSO) and $LaLuO_3$ (LLO). A stoichiometric rotating target in a vacuum chamber is evaporated by a focused laser beam, see Figure 2.9. The target material is ionized and forms a plasma shaped like a plume, which sublimates on a substrate aligned in the spreading direction of the plume. In this work a KrF excimer laser with a wave length of 248 nm, a fluence of 5 J/cm^2, a pulse rate of 10 Hz and a pulse width of 20 ns was used. The substrate was placed on a SiC heater providing temperatures up to 900 °C. The SiC heater is a resistance heater, that heats up, if constant current is flowing through it. Since measuring the temperature of the substrate is impossible and depends strongly on the substrate material and geometry, the exact growth temperature is unknown. Instead the current through the heater was specified. Epitaxial growth was enabled by heating the substrate. The detailed target preparation and the growth parameters are specified in section 3.1.3 and 4.1.2.

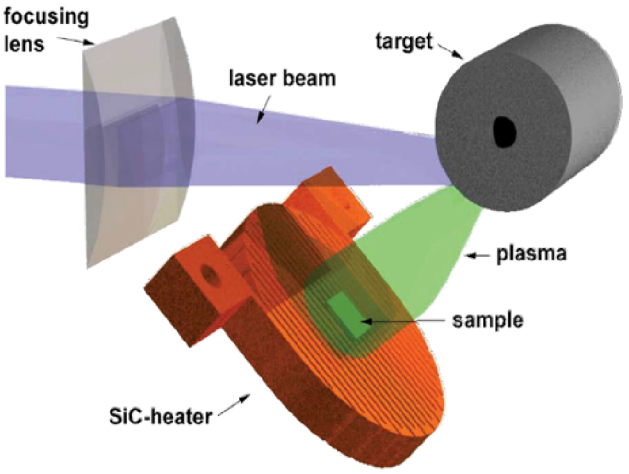

Figure 2.9: Scheme of the PLD showing the laser beam, the target and the sample on the SiC heater.

2.3.2 Atomic layer deposition

Atomic layer deposition (ALD) is one method of chemical vapour deposition with the unique property of a pulsed precursor flow, offering a self-limiting surface reaction. ALD is used to grow thin oxide layers on various substrates like Si. The thickness of ALD grown layers is very precise, since with each cycle the layer grows less than 1 nm, providing a very homogeneous layer with a constant thickness. Each cycle consists of four steps, which are shown in Figure 2.10: In the first step a metal organic precursor is induced into the reaction chamber and the ligands of the precursor react with the OH terminated surface until the surface is saturated. In the second step the residual precursor and the by-products are purged out by Ar, before in a third step ozone is introduced into the chamber, reacting with the free ligands of the precursor. In a final step the ozone and the by-products are purged out by Ar. These steps are repeated, until the desired layer thickness is achieved. In this thesis a *Tricent Oxide-ALD* of the company *AIXTRON SE* with a 300 mm recess in a perpendicular-flow reactor with a showerhead design was used. Samples with a size of 20 x 20 mm^2 were placed in the pockets of a pocket wafer. The pockets were mechanical grinded into a 300 mm Si wafer. The ozone dissolved in oxygen was used as oxygen precursor. The metal organic precursor for deposition of HfO_2 was TEMAHf (Tetrakis[Ethyl-Methyl-Amino]-Hafnium) - $Hf[N(CH_3)(CH_2CH_3)]_4$ and for Y deposition was $Y(nBuCp)_3$.

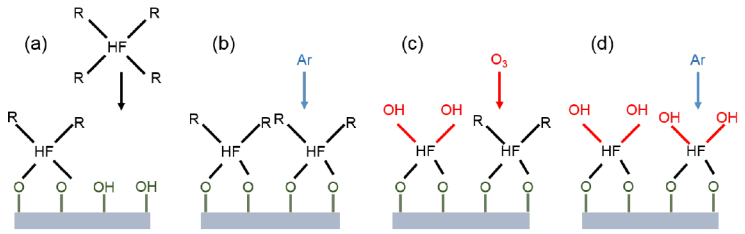

Figure 2.10: Scheme of the ALD process: (a) The precursor reacts with the OH-terminated surface. (b) The residual precursor and the by-products are purged out by Ar. (c) Ozone reacts with the free ligands of the precursor. (d) The ozone and the by-products are purged out by Ar.

2.3.3 Metallization

Metallization of the samples was done by DC sputtering and by electron beam evaporation. For sputtering the samples were placed in a *Oerlikon Sputter Deposition System LLS EVO II*. In the chamber the sample is positioned opposite to the metal, which becomes the cathode by applying a DC electrical current. Ar atoms are inserted into the chamber, which are ionised and accelerated to the target material. The Ar atoms collide with the metal atoms, that are ejected thereby. The metal atoms condensate at the sample surface and form a thin film. An additional reaction gas can be inserted into the chamber, that reacts with the metal on its way to the sample. In this work Ti was sputtered and N_2 was used as reaction gas to form a TiN layer.
Contacts on the samples for electrical characterization were formed by lithography and electron beam evaporation. The oxides were annealed at 115 °C for 20 minutes to dehydrate the oxides, to ensure an adhesion of the photoresist. The thermally stable negative photoresist *AZ nLOF 2020* from *Microchemicals GmbH* was spin-coated at 3000 rpm for 30 s and afterwards annealed for 90 s at 115 °C. For electrical measurements multiple, square top metal contacts with a size of 100 x 100 µm^2 and one big metal contact with a size of (4 mm^2) were defined by a mask and UV exposure. The photoresist was annealed for 90 s at 115 °C, before it was developed by *AZ 326 MIF developers* from *Microchemicals GmbH* for 50 s. The metal was deposited by the e-gun *Balzers PLS 500* of the company *Pfeiffer*. The electron beam is formed at an thermionic-emitting filament and is directed to the desired metal by a magnetic field. The metal is heated up, evaporated and is partially absorbed by the oxide surface. After metal deposition a lift-off was performed in acetone, to solve the residual photoresist, until the structure was revealed.

2.3.4 Rapid thermal annealing

To crystallize the amorphous HfO_2 the samples were annealed within short heating and cooling times, called rapid thermal processing (RTP) or rapid thermal annealing (RTA). For the RTP a *Helios* from *Mattson Technology* was used. During the anneal a constant flow of Ar was applied in the chamber. The layers were annealed for 30 s at various temperatures reaching from 300 °C up to 1000 °C. The *Helios* has a cooling chamber for fast cooling of the samples. If the cooling should not be used, the sample stayed in the heating chamber and an additional gas flow for 8 minutes was adjusted.

2.3.5 Reactive ion etching

Reactive ion etching (RIE) was used to remove a TiN top layer on HfO_2. In contrast to chemical etching, reactive ion etching (RIE) has the advantage of anisotropic etching. In RIE the sample is placed on a cathode, which is connected to a radio frequency generator. The anode is grounded and an etching gas is inserted. Free electrons are accelerated in the electric field and collide with the gas molecules. Thus, the gas molecules are ionized and form a plasma, which is accelerated to the sample and hits it orthogonal to the sample surface. In this work an *Oxford Plasmalab 100 Cluster Tool* is used. The sample is etched with an SF_6 and Ar (ratio 3:1) gas at a pressure of 10^{-8} mbar at 150 W. TiN is strongly etched by this process, while other metals like Pt are not, and are therefore used as hard mask. After RIE the remaining TiN was etched with Standard Clean 1 (SC1) process at RT for 15 s following the approach of Kern et al. [24]. SC1 consists of NH_3, H_2O_2 and distilled water in a ratio of 1:1:5.

3 Rare-earth oxides on GaN

The following chapter comprises the characterization of the rare-earth oxides $GdScO_3$ (GSO), $SmScO_3$ (SSO) and $LaLuO_3$ (LLO) regarding their electrical and structural properties. Electrical properties are investigated with respect to the suitability of the oxides as gate materials. Structural properties of the non-thermodynamic equilibrium, hexagonal phase of the LLO and GSO layer are investigated, to understand the formation of the hexagonal phase. In the following a introduction about the requirements for gate dielectrics, ternary rare-earth oxides on GaN and the sample preparation are elaborated. Subsequently, the results of the electrical and the structural investigations are described, and finally the results are summarised and discussed.

3.1 Introduction

The proceeding development of the computing power demands the improvement of gate dielectric and the exploration of new gate materials. In this thesis the rare-earth oxides $GdScO_3$, $SmScO_3$ and $LaLuO_3$ are investigated. In the following sections the requirements for gate dielectrics and the state of the art for rare-earth oxides is explained. In the final section the sample processing is explained.

3.1.1 Requirements for gate dielectrics

The gate dielectric is important for the effective function of a MOSFET or a MOSCap (see section 3.1.1.2). The MOS system in those devices contains a heterojunction between a semiconductor and a dielectric, and a Schottky barrier in between the dielectric and a metal. To achieve a good performance of the device the gate dielectric has to fulfil several requirements [1]:

- The applied gate voltage falls across the semiconductor and the oxide, whereby a large portion of the applied voltage should fall across the semiconductor close

to the oxide interface. This way a high switching efficiency of the transistor is assured. Therefore, a large ratio of the oxide capacitance and the semiconductor capacitance is desired, which can be achieved by a larger area of the capacitor (A), a thinner oxide thickness (d) or a higher permittivity (κ) of the oxide [1, 25]:

$$C = \frac{\epsilon_0 \kappa A}{d}, \tag{3.1}$$

where ϵ_0 is the vacuum permittivity. A larger area dissents with the scaling of the devices, while the minimal thickness is limited by the occurrence of leakage currents. Therefore, the κ of the gate dielectrics must be boosted, which depends on the material properties as discussed in section 3.1.1.1.

- Leakage in between the semiconductor and the oxides must be prevented, because a good insulation between the semiconductor and the oxides channel is essential. Hence, a high band gap and a high band offset are indispensable and since the band offset does not need to be symmetric a band gap of at least 5 eV and a band offset of at least 1 eV is required. [1, 26]

- The gate dielectric must be thermodynamically stable in contact with the substrate and compatible to established production techniques, i.e. it must be stable at an annealing at 1000 °C for 5 s.

- The gate dielectric must exhibit a high interface quality to the substrate to minimize defects at the interface. Defects and impurities cause an hysteresis and shift of the flatband voltage (V_{fB}).

- Bulk defects should be prevented or reduced, since they cause a shift and a hysteresis of the flat band voltage. Further, defects in the gate dielectric reduce the breakdown voltage.

3.1.1.1 Permittivity

For a high efficiency of electronic devices an increasing capacity of the dielectric gate oxide is necessary. Increasing the area of the capacitor is impossible due to the proceeding scaling of the devices. The thickness of the gate oxide can be reduced until dramatic leakage occurs. Thus, the relative permittivity (κ) must be increased. The relative permittivity is related to the propensity of the gate material to form dipoles under an applied electric field. For simplicity the case of a plate capacitor with two metal plates with vacuum in between is assumed. The electric field (E) in between the metal plates is constant, but when a dielectric is placed between the

metal plates, the electric field in between the dipole charges of the dielectric material decreases. To compensate the loss inside the capacitor, the electric field is increased at the metal plates. The separation of dipole charges under an electric field is called polarisation (P). The increased charges on the metal plates with the inserted dielectric material are equal to the charges of the capacitor placed in vacuum and the polarisation of the dielectric material is described by the following equation [1]:

$$\kappa\epsilon_0 E = \epsilon_0 E + P. \tag{3.2}$$

The relative permittivity of a material depends on its polarizability (α) and the distance between the dipoles (L_m) [1]:

$$\kappa = \frac{1}{1 - \frac{\alpha}{L_m \epsilon_0}}. \tag{3.3}$$

Thus, the relative permittivity depends on the material properties as can be derived from the equation 3.3. Soft materials, that exhibit a higher L_m, exhibit a higher κ than hard materials. The polarisation of a dielectric is caused by four different mechanisms under an applied electric field: Electronic polarisation (i) describes the shift of the electrons around a positive atomic nuclei (see Figure 3.1 (a)). Ionic polarisation (ii) is the displacement of anions with respect to cations (see Figure 3.1 (b)). The orientation of charged molecules is called orientation polarisation (iii), and the last mechanism is interface or space charge polarisation (iv). Due to the different masses contributing to each mechanism, the types of polarisation influence the dielectric at different frequencies. For the used frequencies in modern CMOS technology(10^8-10^{10} Hz) only ionic and electronic polarisation are relevant. [27, 1]

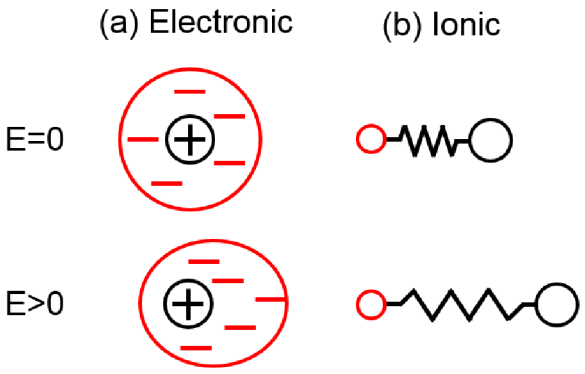

Figure 3.1: Scheme of the electronic polarisation (a) and the ionic polarisation (b) without and under an applied electric field. [1]

The permittivity determined from CV measurements is influenced by additional ox-

ides on the substrate, since the capacity is the sum of the capacity of a deposited oxide and a native oxide like SiO_2 on Si. To determine the permittivity of the gate dielectric capacitance equivalent thickness (CET) plots of the oxides are determined Therefore, using the capacity of a gate dielectric with several thicknesses is measured by CV and the capacity is either extracted at the maximum capacity in accumulation or several volts from the flat band voltage (compare section 3.1.1.2) into the accumulation region. From the determined capacity the CET is calculated by

$$CET = \frac{\epsilon_0 \kappa_{SiO_2} A}{C}, \tag{3.4}$$

where κ_{SiO_2} is the relative permittivity of SiO_2 and is 3.9, A is the area of the capacitor and C is the determined capacity. The CET is the thickness that a SiO_2 gate dielectric would have, to exhibit the same capacitance per area as the measured one. The determined CETs for oxides with varying thickness are plotted over the deposited oxide thicknesses. The slope of the CET can be described by a linear equation:

$$CET = \frac{\kappa_{SiO_2}}{\kappa_{oxide}} d_{oxide} + CET_{IL}, \tag{3.5}$$

where κ_{oxide} is the relative permittivity of the deposited oxide, d_{oxide} is the thickness of the deposited oxide and CET_{IL} is the thickness of the interfacial layer. For Si substrate the interfacial SiO_2 layer thickness can be determined from CET_{IL}.

3.1.1.2 MOSCap and MOSFET

The metal-oxide-semiconductor field-effect-transistor (MOSFET) is the most important device for high-density integrated circuits like microprocessors. A MOSFET is named after the channel opened in the substrate, which is doped oppositely, cf. a p-MOSFET fabricated on a n-doped substrate. The working principle of a MOSFET is described for a p-MOSFET, because the used GaN is n-doped. The principle is the same for an n-MOSFET. A p-MOSFET is produced on a n-doped substrate and consists of a p-doped source and drain region in the semiconductor, an heterojunction between an oxide and the semiconductor, and a Schottky barrier between a metal and the oxide as displayed in Figure 3.2 (a). By applying a positive voltage at the gate metal a channel in between the source and drain region is opened and a current flows. Two types of MOSFETs are distinguished: A depletion type MOSFET (i) is self-conducting, if no gate voltage is applied, while an enhancement type MOSFET is only conductive, if a gate voltage is applied. [5] The electrical properties of the semiconductor, the oxide and the interface of a MOSFET can be

studied at an metal-oxide-semiconductor capacitor (MOSCAP), which is similar to a MOSFET without the source and drain region as shown in Figure 3.2 (b) [1].

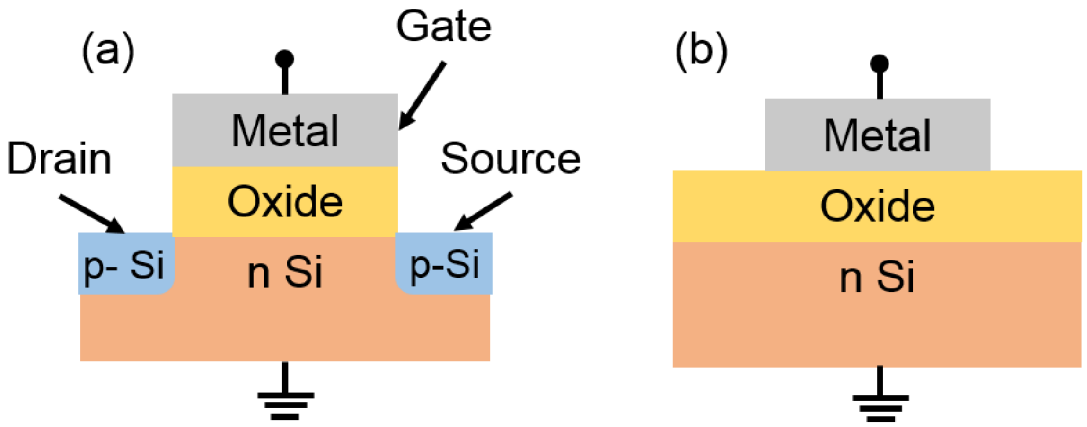

Figure 3.2: (a) Scheme of an MOSFET exhibiting a n-doped substrate, p-doped source and drain regions, a gate oxide and a gate metal. (b) Scheme of a MOSCAP displaying semiconductor, oxide and gate metal. [5]

The band diagram of an oxide semiconductor heterojunction is described for an ideal MOSCAP, which does not exhibit any leakage through the oxide, has zero difference in the workfunction of the gate metal and the semiconductor, and reveals no charge states in the oxide or at the interface. An ideal MOSCAP has three distinguishable states depending on the applied voltage as displayed in Figure 3.3 for a n-type semiconductor. Without an applied voltage the valence band (VB) and the conduction band (CB) are not bent, which is called flat-band condition as shown in Figure 3.3 (a). When a positive voltage is applied to the metal gate the bands are bent downwards, leading to an accumulation of majority carriers (electrons) near the semiconductor surface Figure 3.3 (b). If a negative voltage is applied to the metal gate the bands are bent upwards, causing a depletion of the majority carriers (see Figure 3.3 (c)). If the negative voltage is increased the bands bend even more upwards, so that the intrinsic level (E_I) at the surface crosses over the Fermi energy at the surface. Hence, the concentration of minority carriers (holes) is larger than the amount of majority carriers and the surface is called inverted (inversion compare Figure 3.3 (d)). [1, 5]

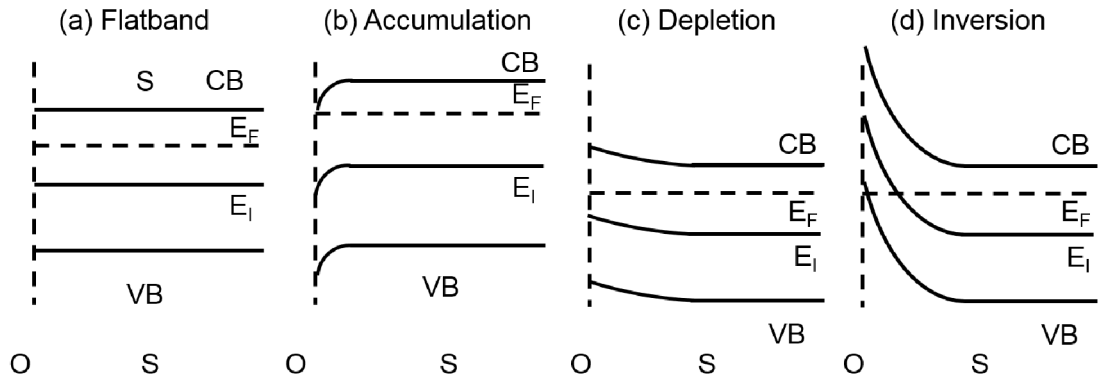

Figure 3.3: Band diagram for the oxide (O) semiconductor (S) interface for a n-type semiconductor at flatband (a), in accumulation (b), in depletion (c) and in inversion (d). [1]

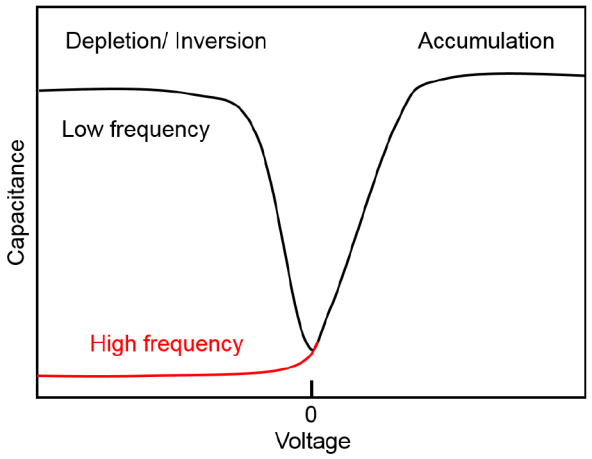

Figure 3.4: CV measurement for a n-doped substrate displaying accumulation at positive voltage and depletion for a high frequency measurement (red curve) and inversion for a low frequency measurement (black curve). [1]

The measured capacity is the sum of the capacity of the oxide and the capacity of the semiconductor's space charge region. During an applied positive voltage the MOSCAP is in accumulation and the electrons are accumulated at the semiconductor interface and in this way the space charge region is negligible and the capacity is large. If a negative voltage is applied the capacitance depends on the measurement frequency. In case of a low frequency measurement minority carries

are generated at the semiconductor interface at high negative applied voltage. The minority carriers accumulate near the semiconductor interface, forming an inversion layer. Accordingly, the space charge region is filled with minority carriers, so that the capacitance increases (Figure 3.4 black line). At high frequency depletion occurs near the semiconductor interface, an extended space charge region occurs. The space charge region contributes to the capacitance, so that the overall capacitance is reduced (Figure 3.4 red line). Due to the high frequency the thermal generation rate for the minority carriers is too low. [1, 5]

3.1.1.3 Heterostructure field-effect-transistor

A heterostructure field-effect-transistor (HFET) is a special type of MOSFET and is also called high-electron-mobility transistor (HEMT) or two-dimensional electron-gas field-effect transistor (TEGFET). The structure of a HFET is shown in Figure 3.5

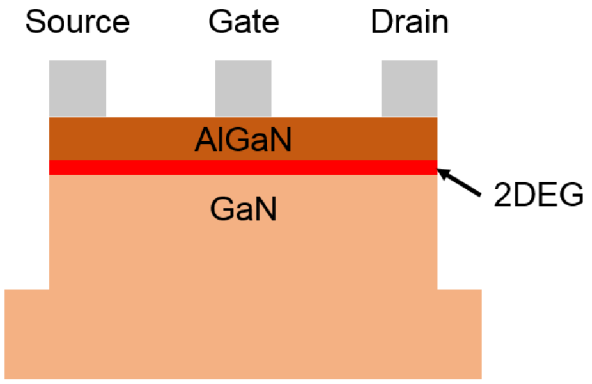

Figure 3.5: Schematic draw of an AlGaN/GaN heterostructure field-effect-transistor. [28]

The special aspect is the heterostructure, which is a combination of doped wide-energy-gap material and an undoped layer, is the formation of a two-dimensional electron gas (2DEG) at the heterointerface of the undoped narrowbandgap layer. For III-V semiconductors the heterostrucutre can be formed by an AlGaN/GaN interface, where carriers diffuse from the wide-energy-gap material into the undoped narrowbandgap layer. Comparable to a MOSFET drain and source are two ohmic contacts, between those a drain-source-voltage is applied. The source and drain contacts are positioned on the upper layer and the contact to the 2DEG is induced by thermal annealing. The electron current in the channel in between the drain and the source is controlled by the sheet charge, which is regulated by the gate voltage (V_G).

Thus, the conducting channel is formed by the 2DEG. A large electron concentration of roughly 10^{13} cm^{-2} is present. Since the channel is almost free of scattering centres, the channel exhibits a large charge carrier mobility. [28] Figure 3.6 displays the band diagram underneath the gate electrode of an AlGaN/GaN HFET. On the left side no gate voltage is applied and the gate is separated from the channel by a high resistance. An applied positive voltage at the drain, a current along the 2DEG will flow. By appling a negative gate voltage at the gate, the bands in the GaN raise and the channel region starts to deplete, until the channel is pinched-off as shown in Figure 3.6 (b). [28]

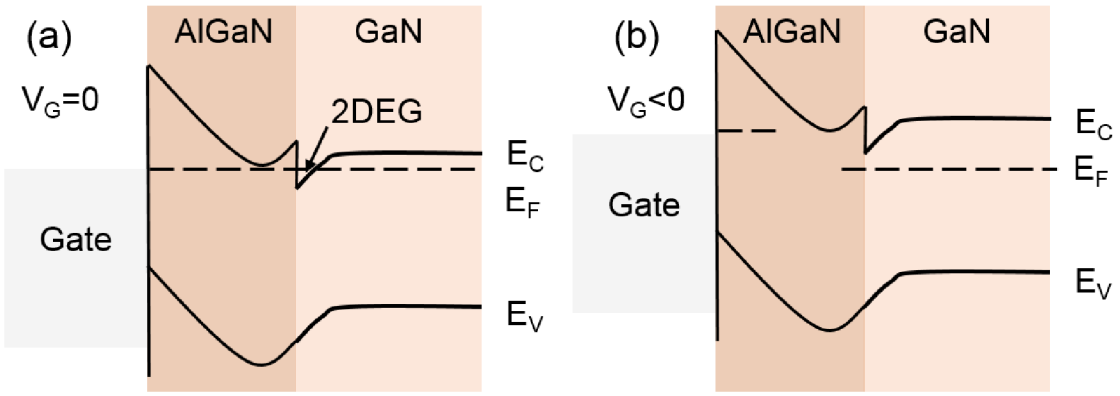

Figure 3.6: Band diagram of an AlGaN/GaN heterostructure field-effect-transistor at zero gate voltage (a) and applied negative gate voltage (b). [28]

3.1.2 Ternary rare-earth oxides

The demand for lower power consumption in modern transistors requires the development of gate oxides with a higher permittivity than (κ) SiO_2 (compare section 3.1.1). Therefore the research focuses on the transition and rare-earth series of the periodic table. According to Engström [1] the reaction of rare-earth metals, like Gd and Lu, with oxygen creates insulators with a high κ, due to their high ionicity and their atomic structure (compare 3.1.1.1). Ternary oxides based on rare-earth metals like $LaLuO_3$ and mixtures between rare-earth and transition metals like $GdScO_3$ have promising features for applications. Binary oxides exhibit a large band gap (E_g) lack a high-κ or vice versa. This disadvantage ternary rare-earth oxides can overcome. [1] Various applications of ternary rare-earth oxides have been reported. Misra et al. deposited $SmGdO_3$ by PLD for resistive switching memory devices, in which three different values of resistance were measured, indicating the promising application of $SmGdO_3$ as resistive random access memory [29]. Amorphous

$GdScO_3$, $DyScO_3$ and $LaScO_3$ were deposited by PLD as high-κ gate dielectric on Si. A lower leakage current and a much higher crystallization onset temperature were measured, compared to HfO_2. A higher crystallization temperature is beneficial, because high temperature anneals are necessary for device fabrication. [30] Gottlob et al. reported on a fully functional n-MOSFET with epitaxial Gd_2O_3 high-κ gate dielectrics and TiN metal gate [31].
An auspicious substrate for future transistors is GaN for power electronic applications, like power conditioning, microwave amplifiers and transmitters, due to its outstanding properties [7]. GaN reveals a band gap of 3.4 eV [5], a high breakdown voltage, fast switching speed, high-power handling, low on-resistance [6] and intrinsic robustness [7]. In contrast to SiO_2, III-V semiconductors like GaN lack a native oxide as an insulator and for passivation [32]. Therefore, a suitable oxide for GaN passivation and reduction of interfacial traps is desired. GaN suffers from a current collapse at high drain voltages, which is an increased resistance in the channel region. The mechanism for the current collapse is still unknown, but trapped electrons by surface states in high-electric fields are supposed to cause the increasing resistance [33, 34]. Current research focuses on oxides for the surface passivation to reduce the current collapse by trapped electrons. Huang et al. achieved dynamic ON-resistance reduction and significant current collapse suppression by AlN deposition grown by plasma-enhanced atomic layer deposition [6].
Further, oxide-based high-κ dielectrics like HfO_2 [35] and Al_2O_3 [34] have been deposited as passivation layer. Besides common dielectrics, rare-earth oxides are investigated as gate dielectric for GaN. Lin et al. fabricated a metal-insulator-semiconductor high-electron mobility-transistor (MISHEMT) using an electron beam evaporated Er_2O_3 gate oxide on AlGaN. The MISHEMT revealed a more than four orders of magnitude lower gate leakage than that of the corresponding conventional SiO_2/Si HEMT. XPS measurements reveal the formation of a natural oxide of AlGaN during fabrication. [36] Trivalent oxides like most rare-earth oxides form better interfaces with the GaN than covalent oxides, because they allow charge matching across the interface [36, 37]. In addition, rare-earth oxides are thermodynamically stable in contact with GaN [36]. Jur et al. reported on the epitaxial growth of Sc_2O_3 and La_2O_3 on GaN by MBE for enhancement mode MOSFETs. The Sc_2O_3 and La_2O_3 are epitxial grown in the hexagonal phase, so that the leakage is reduced in comparison to amorphous Sc_2O_3 and La_2O_3, due to less electrical defects. Though, the leakage reduction can be dwindled by the high lattice mismatch of 21% and 7.2% for La_2O_3 and Sc_2O_3, respectively. Due to the lattice mismatch the layers reveal a high concentration of dislocations, creating possible leakage paths. However, no increased gate leakage was measured, which is explained by the surface passivation of GaN by an oxide, which reduces the electrical defects or is a barrier to leakage paths between electrical defects in the oxide to the GaN. This oxide could be Ga_2O_3, that forms due to the large growth temperature of 400 °C. The existence of Ga_2O_3 is proven by X-ray photoelectron spectrospcopy, by which a Ga-O bond

is detected. [38] Besides the effect of the lattice mismatch on the leakage, it also influences the nucleation and growth mode. Further, the La_2O_3 is hygroscopic and reveals La-O-H bonds measured by XPS [38]. Gd_2O_3 as gate oxide in a MOSFET was investigated by Johnson et al. The Gd_2O_3 exhibits a κ of 11.4 and a E_g of 5.3 eV and was grown in the bixbyite crystal structure on GaN by MBE. The leakage through the gate oxide disabled the MOSFET, so that an additional amorphous SiO_2 layer was necessary for insulation. [39]
Many ternary rare-earth oxides are known to crystallize in a rhombohedral perovskite structure. The common building block in this structure is, that oxygen atoms form a tetrahedron with Sc, Ti or Lu in its center. However, few years ago a so far unknown hexagonal phase of the ternary rare-earth oxides $LaLuO_3$(LLO) and $GdScO_3$(GSO) was discovered [4]. For the LLO and the GSO various crystalline phases have been reported, which are listed in table 3.1. Additionally the reported crystal structure of the binary oxides Sc_2O_3, Gd_2O_3 and La_2O_3 are shown. For the ternary rare-earth oxides no hexagonal phase has been reported before and from the binary rare-earth oxides only La_2O_3 and Sc_2O_3 exhibit a hexagonal phase.

Table 3.1: Reported crystal structures, space group and relative permittivity of the rare-earth oxides $GdScO_3$, $LaLuO_3$, Sc_2O_3, Gd_2O_3, La_2O_3 and Lu_2O_3

Material	Crystal structure	Space group	Relative permittivity	Reference
$GdScO_3$	orthorhombic	Pnma	-	[40, 41]
$LaLuO_3$	cubic	-	30	[42]
$LaLuO_3$	orthorhombic	Pbnm	30	[43]
$LaLuO_3$	orthorhombic	-	-	[44]
Sc_2O_3	hexagonal		-	[38]
La_2O_3	hexagonal	-	-	[38]
Gd_2O_3	cubic	$Ia\bar{3}$	-	[45]

The crystal structure was determined by XRD and TEM as shown in Figure 3.7. In Figure 3.7 (a) a Ψ-scan of GSO on GaN of the $1\bar{1}01$ reflection is shown, exhibiting a sixfold symmetry of the GSO, which proves the existence of the hexagonal phase. In Figure 3.7 (b) a diffraction pattern of the LLO and the GaN substrate along the (1210) zone axis is displayed. Since the diffraction spots of the LLO are next to the GaN ones, the LLO layer is grown epitaxial and has a similar hexagonal crystal structure. The oxides were epitaxial grown by pulsed laser deposition (PLD) on GaN (0001) and Si/Y_2O_3 substrate at about 680 °C. The lattice parameters determined from XRD and TEM are a=0.38 nm and c=0.61 nm, and a=0.36 nm and c=0.59 nm for LLO and GSO, respectively. The c-axis of the oxides is perpendicular to the substrate surface. The layers reveal a high lattice mismatch between the oxide and

GaN of 13% and 18% for GSO and LLO, respectively. Schäfer suggested an epitaxial growth, whereby not every atom of the oxide layer is matched to a substrate atom, but still some atoms of the oxides are matched to the substrate atoms in periodic distance. [4]

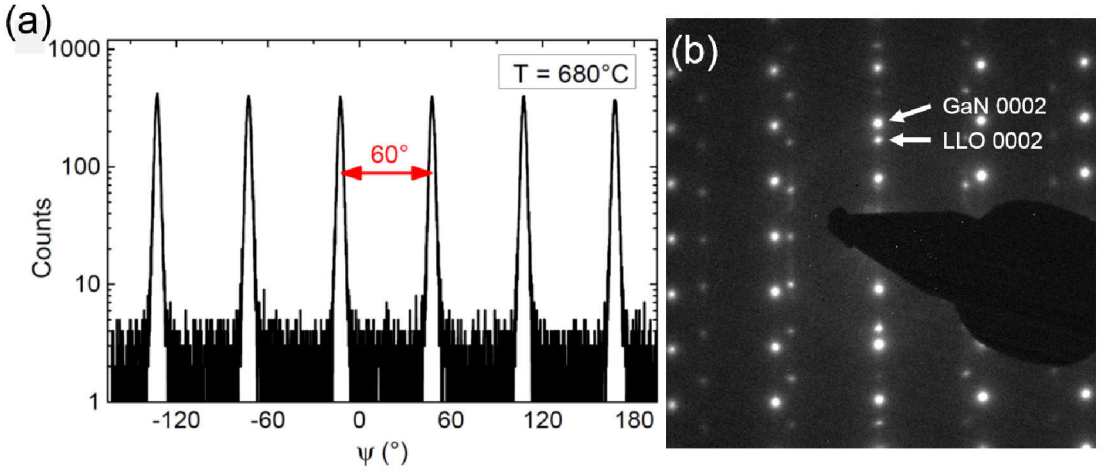

Figure 3.7: (a) Ψ-scan of GSO on GaN of the $1\bar{1}01$ reflection showing a sixfold symmetry to prove the hexagonal structure. (b) Diffraction pattern along the (1210) zone axis of LLO on GaN displaying the epitaxial, hexagonal growth by the LLO diffraction spots next to the GaN ones. [4]

For the hexagonal LLO on cubic Y_2O_3 Schäfer suggested, that every fifth atom of LLO fits to every sixth atom of Y_2O_3. In this way the lattice mismatch is reduced below 2% for the hexagonal LLO and GSO on GaN. To understand the formation of the hexagonal phase, ab-initio calculations were made. A density functional theory using the full-potential linearized augmented plane wave (FLAPW) approach was applied. Because the space group of the hexagonal phase is unknown, several possible unit cells were investigated. The simplest model was an ordered in-plane hexagonal phase and alternating Sc and Gd layers in the out-of-plane direction. The further calculated models were considered as alloys with larger unit cells. The calculations revealed, that the phase is not at thermodynamic equilibrium. Due to electrical defects in the GaN no electrical characterization of GSO and LLO on GaN was possible. Therefore, the electrical properties were investigated on Si/Y_2O_3, revealing a relative permittivity (κ) of 26 and 24 for LLO and GSO, respectively. [4] This work continues the research on the ternary rare-earth oxides $GdScO_3$ and $LaLuO_3$ and investigates the structural and electrical properties. In particular the ternary rare-earth oxides are electrically characterised, to verify their potential as high-κ gate

dielectric. Further, the interface is investigated by transmission electron microscopy and X-ray diffraction in respect to the structure and chemical composition, because the formation and the stabilization of the hexagonal phase is expected to arise from the interface structure.

3.1.3 Sample preparation

In this chapter the sample preparation of the metal-oxide-semiconductor capacitors (MOSCaps) of the ternary rare-earth oxides is described. The explanation of the applied methods is described in the chapter 2. A scheme of the capacitor fabrication is shown in Figure 3.8.

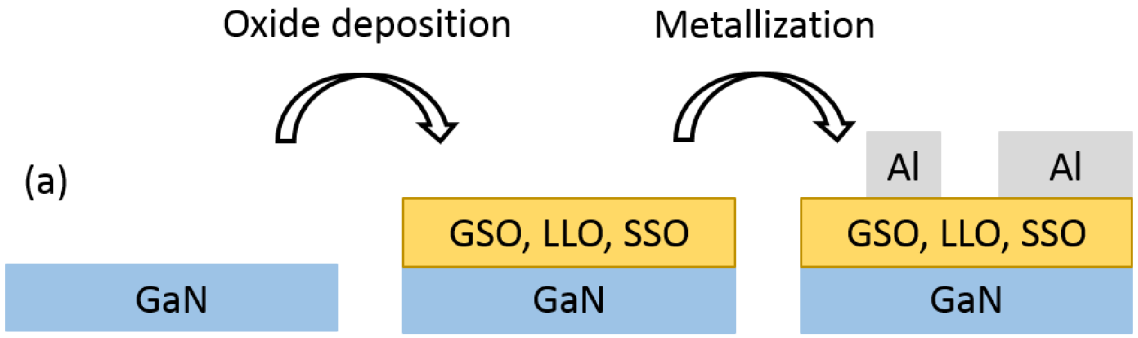

Figure 3.8: Scheme of the capacitor fabrication of ternary rare-earth oxides on GaN.

The high-κ oxides $GdScO_3$ (GSO), $SmScO_3$ (SSO) and $LaLuO_3$ (LLO) were deposited on 3 µm thick hexagonal GaN (0001) in a wurtzite crystal structure, deposited on α-Al_2O_3 by metalorganic vapor phase epitaxy [46]. Further GaN, AlGaN and InGaN from NovaGaN was utilised, which are grown on a Si wafer [47]. The GaN was provided as 2 inch wafers. For sample preparation the wafers were spin-coated with photoresist and cut into 8x8 mm^2 square pieces by a diamond saw. Before oxide deposition the photoresist was solved, to prevent contamination of the substrate. The substrate pieces were cleaned twice in acetone in an ultrasonic bath for five minutes and afterwards cleaned in isopropyl for three minutes. To remove any surface contamination, the substrates were cleaned in 30% H_2SO_4 for 5 minutes and in 30% HCl for 2 minutes. After each etching the substrate was rinsed with distilled water.
For pulsed laser deposition of the rare-earth oxides the GSO, SSO and LLO stoichiometric targets were prepared by mixing 99.99 % Gd_2O_3 and Sc_2O_3, Sm_2O_3

and Sc_2O_3 and La_2O_3 and Lu_2O_3 powders in the desired amount, respectively. The GSO, LLO and SSO powders were ball milled in isopropanol for 24 h and calcined at 1300 °C for 24 h. Finally, the powders were pressed into 25 mm targets and sintered at 1500 °C for 12 h. For epitaxial growth the substrates were heated up to 900 °C. Finally 100 nm thick Al contacts were defined on the oxides as described in section 2.3.3.

3.2 Experimental Results

In the following section the experimental results of the ternary rare-earth oxides on GaN are presented. First the electrical characterization and secondly the structural investigation are shown. In the subsequent section the results are summarized and discussed. Parts of this work have already been published [48, 49, 50].

3.2.1 Electrical characterization of $GdScO_3$ and $LaLuO_3$

Capacitance voltage (CV) measurements of hexagonal $GdScO_3$ (GSO) layers deposited on GaN with different thickness in the range of 5-40 nm were performed. The capacity was normalized to the area of the small pad and plotted against the applied voltage as shown in Figure 3.9. All measured CV curves exhibit a low capacity at negative voltages and a large capacity at positive voltages, which can be explained by the band diagram of the GaN substrate: The GaN is n-doped and therefore the Fermi energy level is close to the conduction band (compare section 3.1.1.2). Thus, an applied positive gate voltage bends the bands downwards and the majority carriers, electrons, accumulate at the interface, so that the measured capacity is the capacity of the GSO oxide layer as shown as inset on the right side of Figure 3.9. At negative voltages the bands of the GaN bend upwards and the semiconductor is depleted (see inset left side Figure 3.9). Besides the GSO oxide an additional capacitance of the depletion layer contributes to the overall capacity, so it is reduced. Due to the large band gap of the GaN and the measurement frequency of 100 kHz no inversion layer is formed. With increasing layer thickness the capacity is reduced. The flatband voltage (V_{fB}) is determined at the inflexion point of the CV curve. The V_{fB} differs for the shown sample and it is in the range of -0.22 V up to 0.04 V. All measured hexagonal GSO on GaN samples during this thesis revealed a varying V_{fB}. Electrical defects in the oxide, like oxygen vacancies, or surface defects of the semiconductor, like imperfections of the crystal at the interface, are charged and screen an applied voltage, which effects the band diagram and consequently the

measured CV curve as well as the V_{fB} (compare section 3.1.1.2). The GaN substrate surface is rough as is shown in Figure 3.10. In the atomic force microscope image diverse levels and several holes are visible . The determined average roughness (R_a) is 0.3 nm Those imperfections of the substrate surface vary and consequently the electrical defects and the V_{fB} of each measured sample and pad.

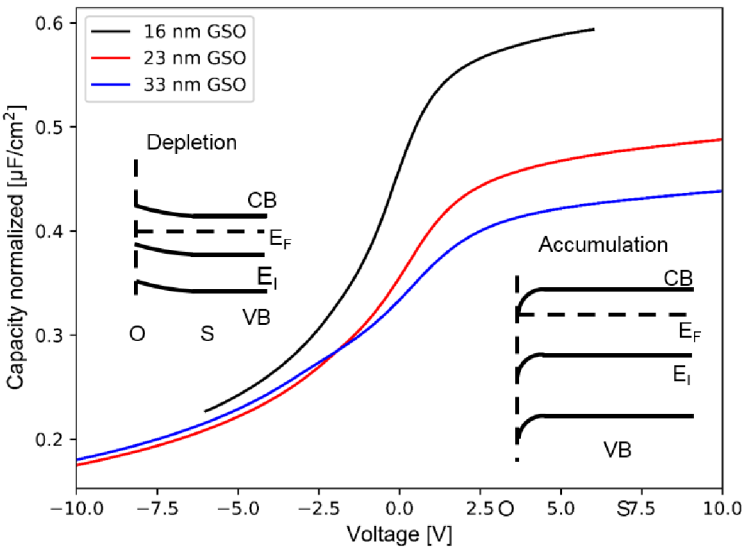

Figure 3.9: CV measurement of hexagonal GSO on GaN with layer thicknesses of 16, 23, 33 nm.

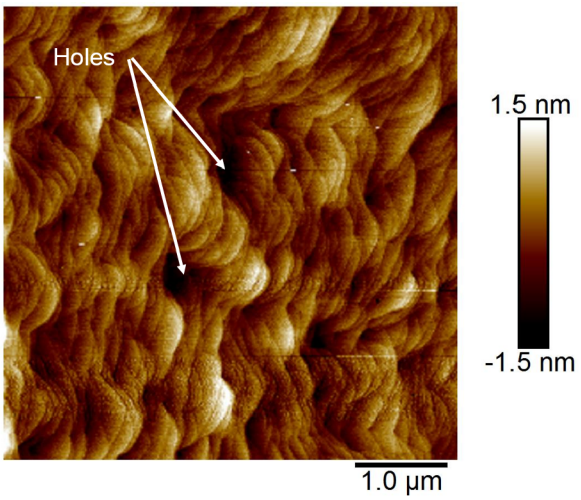

Figure 3.10: AFM image of the GaN substrate revealing a R_a of 0.3 nm.

The influence of the applied voltage on the capacitance was investigated (Figure 3.11 (a)) by applying a symmetric voltage shift from negative to positive voltage and backwards. With increasing applied voltage the CV curve shifts from negative (black curve) to positive voltages (blue curve). To achieve a shift of the curve to positive voltages, negative charges must be created [1]. The negative charges add an internal negative voltage to the applied one and in this way, the CV curve is shifted to a more positive applied voltage. By applying larger voltages on the sample, the amount of negative charges is increased, because the CV curve is shifted further to positive voltage. In order to investigate the stability of the negative charges, multiple CV measurements with the same voltage range were executed immediately and after 15 h and 64 h on the same pad. In Figure 3.11 (b) the first measurement reveals a hysteresis of 0.5 V. Further measurements run along the backwards sweep of the first measurement and exhibit a smaller hysteresis of 0.1 V as shown by the red curve. Thus, the charges are stable and cannot be reduced or extinguished by inverting the applied voltage. The measurements after 15 h and 64 h exhibit the same hysteresis and the same curve shape as the last measurement before waiting. This implies, that the charges are stable over time.

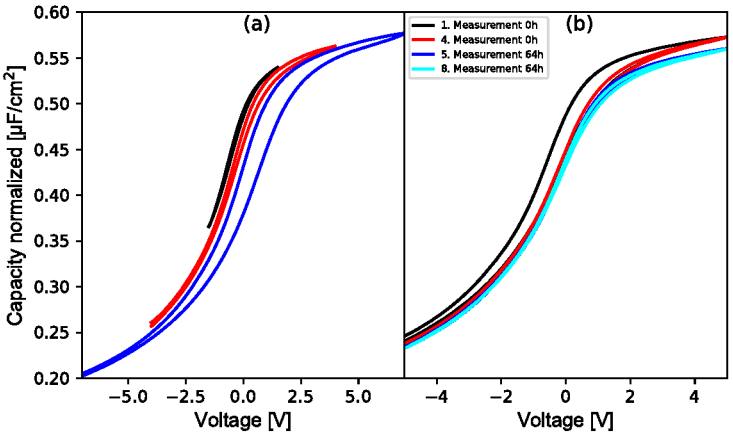

Figure 3.11: CV measurement of 16 nm thick hexagonal GSO on GaN: (a) CV characteristics for increasing applied voltage. (b) Multiple measurements of the layer immediately and after 64 h.

The electrical measurements are carried out for GSO on GaN, which is GaN grown on Al_2O_3, and on Novagan, which is GaN grown on Si. From the measured CV curves the capacitance equivalent thickness (CET) is determined for different layer thicknesses of hexagonal GSO on GaN and NovaGaN by the following formula:

$$CET = \frac{\kappa_{IL}}{\kappa_{oxide}} d_{oxide} + CET_{IL}, \tag{3.6}$$

where κ_{oxide} is the relative permittivity of the deposited oxide, κ_{IL} the relative permittivity of the interfacial layer and is assumed to be 3.9, d_{oxide} is the thickness of the deposited oxide and CET_{IL} is the thickness of the interfacial layer. To calculate the CET the capacity is extracted at V_{fB} + 1.5 V. The resulting CET plots are shown in Figure 3.12.

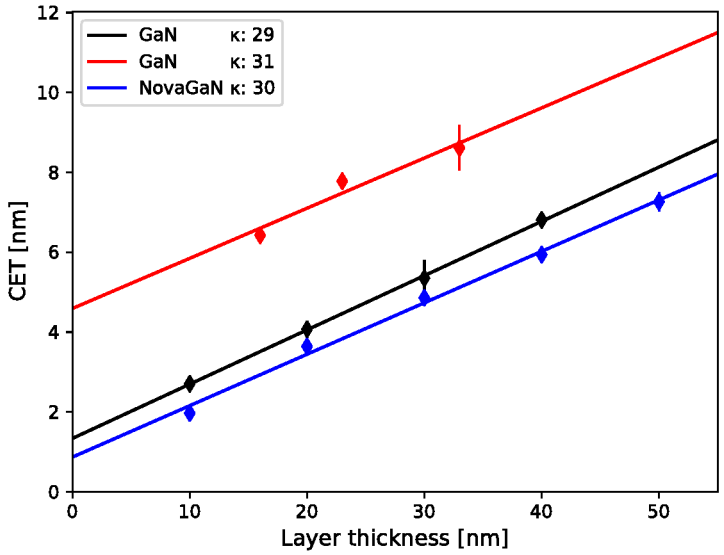

Figure 3.12: CET plot of hexagonal GSO on GaN (GaN on Al_2O_3) and on NovaGaN (GaN on SiO_2) with a κ of 30 $\pm$ 1.

For high-κ oxides on Si the CET value at a layer thickness of 0 nm is assigned to the native SiO_2 layer thickness. For the oxides on GaN the interfacial layer would vary from 1 nm up to 5 nm in thickness. The existence of a native, interfacial layer with a thickness of 1 nm or even thicker is unlikely, since no growth of a thick native oxide on GaN is known as for Si. Further, the interfacial layer should reveal a similar thickness for each CET plot and no interfacial layer is visible in transmission electron microscopy (3.2.3.1). Since the CET and the capacity are inversely proportional, a larger CET is related to a smaller capacity, which could be reduced by the varying substrate quality. Further, the calculated CET is influenced by the chosen κ_{IL} and can be shifted up and down by changing this value. The linear fit is shifted by the chosen κ_{IL}, and therefore the intersection of the linear fit with the y-axis

is arbitrary. Hence, the interfacial layer thickness determined from the CET plot can be influenced by the assumed κ of the interfacial layer, so that the theoretical thickness of the interfacial layer is arbitrary. Despite the varying interfacial layer thickness, the determined permittivity of the oxides is 30 ± 1 and it is independent of the substrate used.

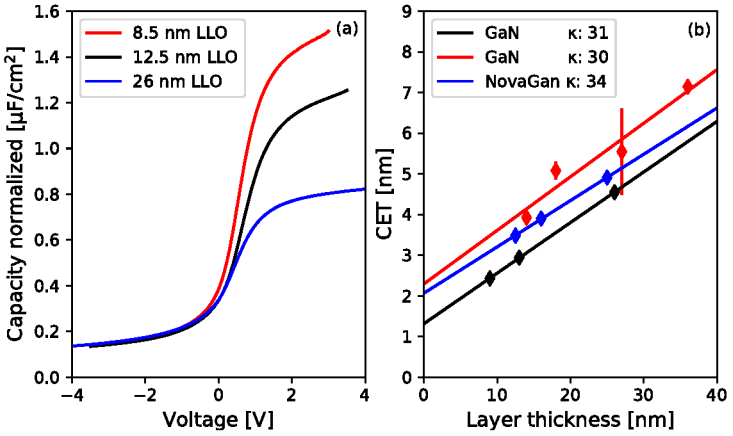

Figure 3.13: (a) CV measurements of hexagonal LLO on GaN with layer thicknesses of 16, 23, 33 nm and (b) CET plot of hexagonal LLO on GaN (GaN on Al_2O_3) and on NovaGaN (GaN on SiO_2) with a κ of 32 ± 2.

Hexagonal LLO layers with thicknesses from 8.5 nm up to 26 nm deposited on GaN are investigated by CV measurements as displayed in Figure 3.13 (a). As expected the capacity decreases with increasing layer thickness. Further, the V_{fB} is extracted by the inflexion point of the CV curve. The V_{fB} is 0.5 V, 0.7 V and 0.4 V for the 8.5 nm, 12.5 nm and 26 nm thick layer, respectively. Thus the V_{fB} is 0.7 V larger than the V_{fB} of hexagonal GSO and determined by the surface of the GaN. The capacity of hexagonal LLO with varying thickness deposited on GaN and NovaGaN is measured and the CET value is calculated. The CET values are plotted over the oxide thickness and a linear fit is determined as shown in Figure 3.13 (b). The permittivity is 32 ± 2, and slightly larger for the layers grown on NovaGaN and is comparable to the one of hexagonal GSO. The varying intersection of the linear fit with the CET axis results from the varying substrate quality.
Amorphous GSO with thicknesses of 9, 14, 35 nm is deposited on GaN and investigated by CV measurements. From the determined capacity the CET value is calculated, plotted over the oxide thickness and a linear fit is determined as displayed in Figure 3.14. From the slope of the linear fit the permittivity is determined. Amorphous GSO reveals a permittivity of 23, which is lower as the one of hexagonal GSO. The determined interfacial layer thickness of 5 nm is arbitrary and most

probably results from electrical defects at the interface.

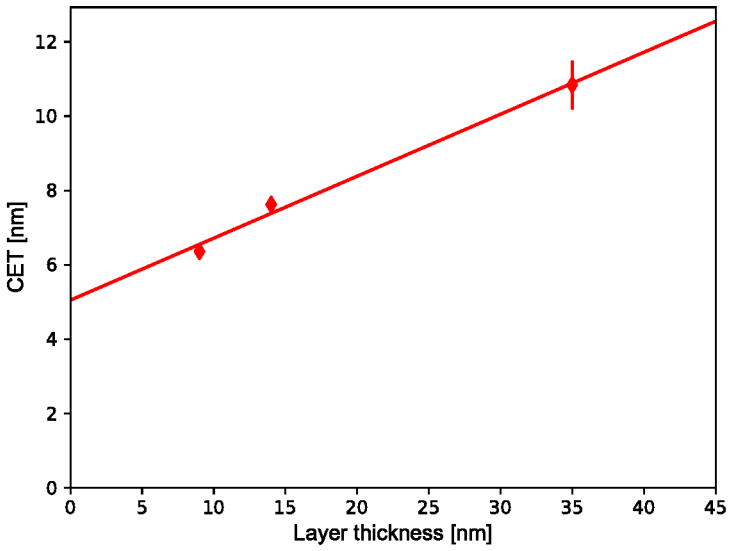

Figure 3.14: CET plot of amorphous GSO on GaN providing a κ of 23.

Current voltage (IV) measurements of the hexagonal GSO (black), amorphous GSO (red) and hexagonal LLO (blue) layers are shown in Figure 3.15. On a sample various pads were measured and the voltage is increased from 0 V either up to the maximum negative or positive voltage, where breakthrough occurs. The measured current is normalized to the area of the measured pad for comparison. For each sample the IV curves for a positive and a negative voltage sweep are combined and the current is plotted against the applied electric field. The electric field is calculated from the applied voltage and the layer thickness. The IV curves are shown in Figure 3.15. All measurements reveal an asymmetric curve with a smaller resistance at positive voltage than at negative voltage. The hexagonal GSO is the most stable oxide, which exhibits breakthrough at 7.2 MV/cm and -13.4 MV/cm. Three regions can be distinguished: a region of no leakage up to 3 MV/cm, a soft breakthrough with an increasing current proportional with the electric field and breakthrough at 7.2 MV/cm. Amorphous GSO exhibits the same behaviour, but breaks at lower electric field (5.5 MV/cm). Hexagonal LLO reveals the largest leakage current of all the oxides investigated. It exhibits a current at positive voltage of 312 µA/cm^2 at an electric field of 1 MV/cm. At negative voltage LLO exhibits the largest current, too, but breakdown occurs at -14.4 MV/cm comparable to hexagonal GSO.

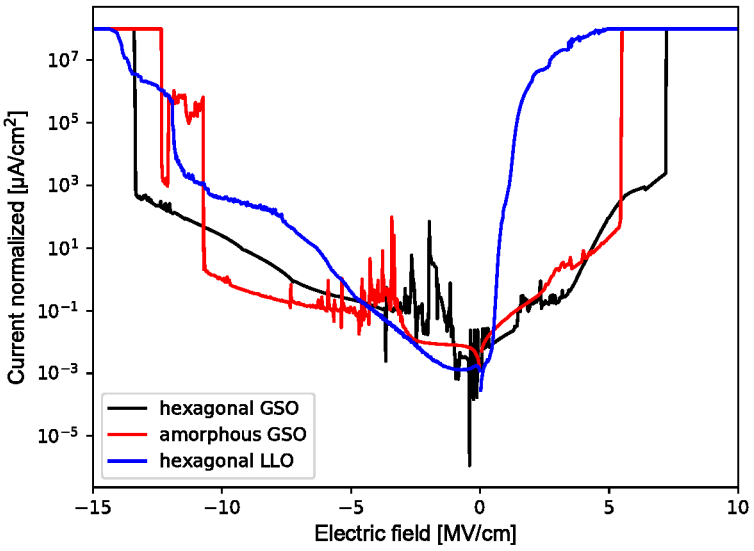

Figure 3.15: IV measurement of hexagonal GSO (black), amorphous GSO (red) and hexagonal LLO (blue) measured up to breakthrough at positive and negative electric field.

3.2.2 Bonding analysis and band alignment

The deposited amorphous and hexagonal GSO and the hexagonal LLO on GaN are investigated by X-ray photoelectron spectroscopy (XPS) to determine the bonds of GaN and the deposited oxides, and the band alignment of the GaN and the oxide. The measurments are performed at the Department of Materials Science and Engineering at the Technion in Haifa. XPS measurements are surface sensitive, because the spectra is recorded of a depth of approximately 10 nm. As a consequence either the bare substrate or the substrate with an additional 4 nm thick oxide layer is used. A XPS investigation of the bare NovaGaN at the Ga*3p* peak is displayed in Figure 3.16 (a). The black dots are the measured XPS intensities at different binding energies. The XPS measurement reveals two distinguishable peaks: One matches to the energy of Ga bound to N (Ga-N). A second peak at a binding energy of 100-102 eV is visible in the spectra. The XPS spectrum for a Ga-N reflection is fitted to the data and is depicted by the blue area in Figure 3.16 (a). The blue area does not fill the whole area underneath the measured XPS spectra. Thus, besides the Ga-N bond a second covalent bond of different nature contributes to the total intensity. The existence of a Ga-O bond is unlikely, because GaN is stable

in the enviroment and Ga_2O_3 is usually not formed [51]. Further, the Ga-O peak is at larger energies compared to Ga-N. The GaN is cleaned by HCl, so that the additional height could results from the energy of Ga bound to Cl (Ga-Cl). This bond is expected at lower energy than the Ga-N, which would match to the measured results. The XPS spectra for a Ga-Cl reflection is fitted to the data and shown by the red area in Figure 3.17 (a). The sum of contributions of Ga-N and Ga-Cl, displayed by a dark line, fits to the measured XPS spectra. Further the existence of the Cl is proven by the Cl*3s* peak at 16-17 eV. [49]

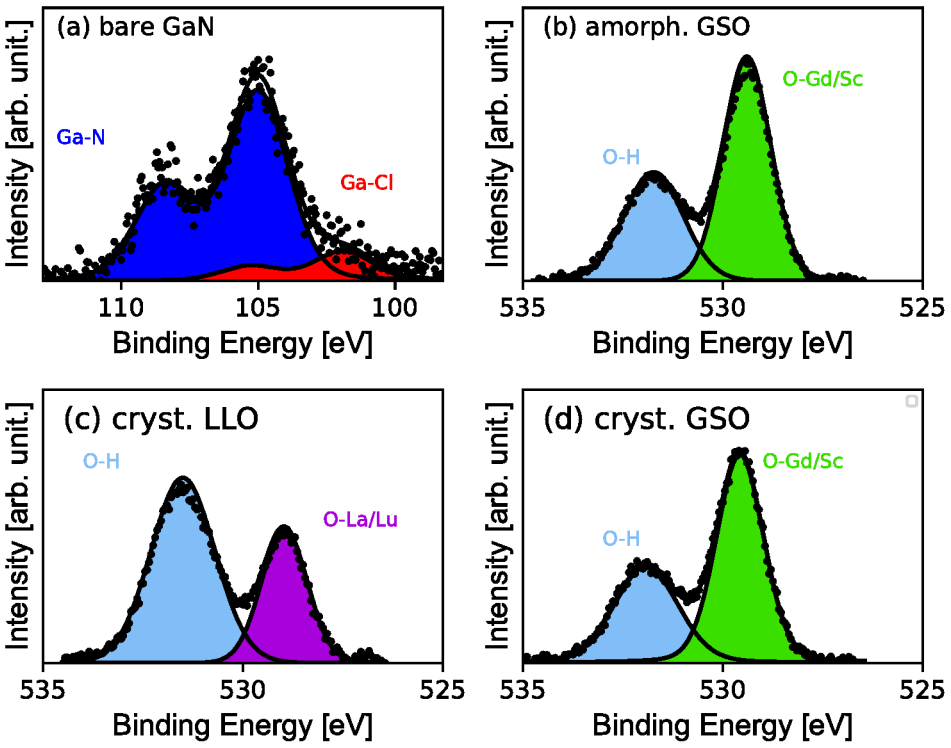

Figure 3.16: XPS measurement at the Ga*3s* peak on bare NovaGaN (a). [49] XPS measurements at the O*1s* peak for amorphous GSO on NovaGaN (b), crystalline LLO on NovaGaN (c) and crystalline GSO on NovaGaN (d). The black dots show the measured intensity of the XPS spectra. The coloured areas indicate the contribution to the spectra of the different bondings.

In Figure 3.16 XPS measurement of the O*1s* peak of amorphous GSO (b), hexagonal

LLO (c) and hexagonal GSO (d) deposited on GaN are shown. In each spectrum two peaks can be distinguished. The shift of the peak position for O*1s* is related to the electronegativity of the binding atom of O. However, Sc and Gd have nearly the same electronegativity and therefore the shift of the O*1s* peak on the GSO samples is similar for a Gd or a Sc bond. Thus, the peak of O bound to Gd (O-Gd) can not be distinguished from the peak of O bound to Sc (O-Sc). Hence, the peak at 529 eV in Figure 3.16 (b) and (d) is related to O-Gd and O-Sc, displayed by the green area. The shift of the O*1s* peak due to the binding of O to either La (O-La) or Lu (O-Lu) can not be distinguished, too, because of the same electronegativity. Hence, the peak at a binding energy of 529 eV in Figure 3.16 (c) is related to O-La/Lu, coloured purple. The second peak at 532 eV is most likely related to O bound to H (O-H) coloured blue, because rare-earth oxides are highly hygroscopic. From the ratio between the O-Gd/Sc and the O-H peaks a qualitative conclusion on the quality of the oxide can be drawn, because at structural defects H can be absorbed. The amorphous GSO reveals a lower ratio compared to crystalline GSO, because amorphous layers are not stressed and are less influenced by structural defects in the GaN. Consequently, the LLO with the largest mismatch reveals the largest amount of H due to more structural defects.
The band gap of the rare-earth oxides is determined from the O*1s* fitted peak and the related electron energy loss onset as displayed in Figure 3.17 (a) for hexagonal GSO on NovaGaN. The XPS spectra reveals the O*1s* energy ($E_{O1s(max)}$) at 531.9 eV. The related electron energy loss onset (E_{onset}) is the lowest electron energy loss contribution and is determined from the intersection of the linear fit of the inelastic scattering tail with the minimum intensity and is at 537.2 eV. The band gap is determined by

$$E_{gap} = E_{onset} - E_{O1s(max)}, \tag{3.7}$$

where E_{gap} is the band gap and is 5.3 eV.
The valence band offset (VBO) is determined from the onset of the valence band of the oxide ($E_{VB\,oxide}$) and the semiconductor ($E_{VB\,semiconductor}$). Here the onset is defined as the intercept of the linear interpolation of the valence band (VB) peak and the average background. The average background is fixed to 0 eV, because no electrons are emitted at any energy lower than E_{gap}. The VBO is calculated by

$$VBO = E_{VB\,Semiconductor} - E_{VB\,Oxide}. \tag{3.8}$$

In Figure 3.17 (b) the XPS spectra with the onsets of the oxide and the semiconductor of hexagonal GSO on NovaGaN is shown. The linear fit to the onset of the

semiconductor intersects with the average background at 2.6 eV, while the linear fit to the onset of the hexagonal GSO intersects with the average background at 6.3 eV. Thus, the VBO offset is 3.7 eV. [49] The VBO and the E_{gap} for amorphous and hexagonal GSO, and hexagonal LLO are listed in table 3.2.

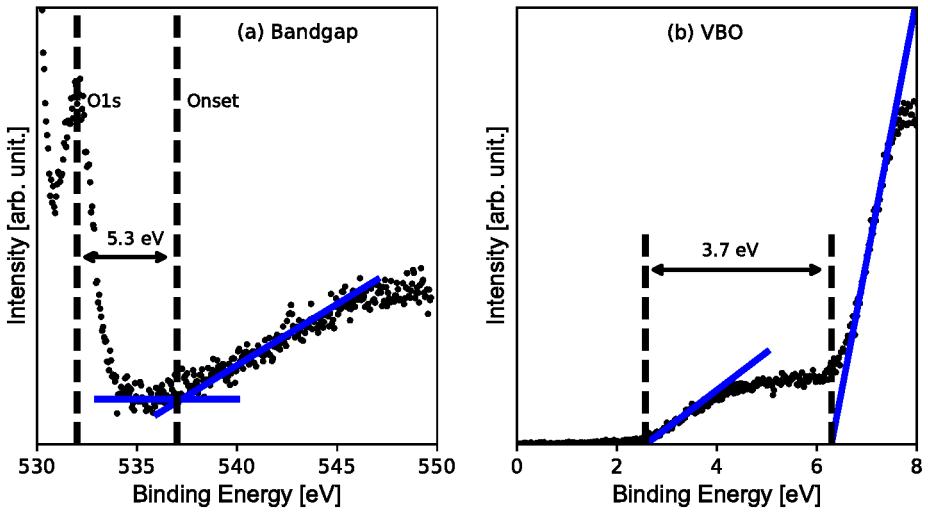

Figure 3.17: (a) Determination of the band gap of hexagonal GSO on NovaGaN from the distance of the the O*1s* fitted peak and the related electron energy loss onset. (b) Valence band offset determination from the onset of the valence band of the oxide and the semiconductor. [49]

The band structure of amorphous GSO, hexagonal GSO and hexagonal LLO on NovaGaN is constructed from the E_{gap} of the oxides, VBO and E_{gap} of GaN (3.4 eV [5]) as shown in Figure 3.18. Therefore, the VB of the oxide is plotted in relation to the VB of the GaN by the VBO, whereby the VB of the GaN is the upper one. The conduction band (CB) band of the semiconductor and the oxide can be plotted from the known E_{gap} of the semiconductor and the oxide, respectively. From the calculated band structure the conduction band offset (CBO) is determined. The values for all investigated structures are shown in table 3.2. All investigated phases of the ternary rare-earth oxides GSO and LLO reveal a CB in the band gap of the semiconductor. This staggered band alignment causes a high potential barrier at negative voltage at the metal electrode and thus no or small current. In contrast, at positive voltage no barrier exists in between the semiconductor and the oxide. Hence, a current will flow. The different behaviour of the current is shown in Figure 3.15, revealing an asymmetric shape of the current voltage characteristic.

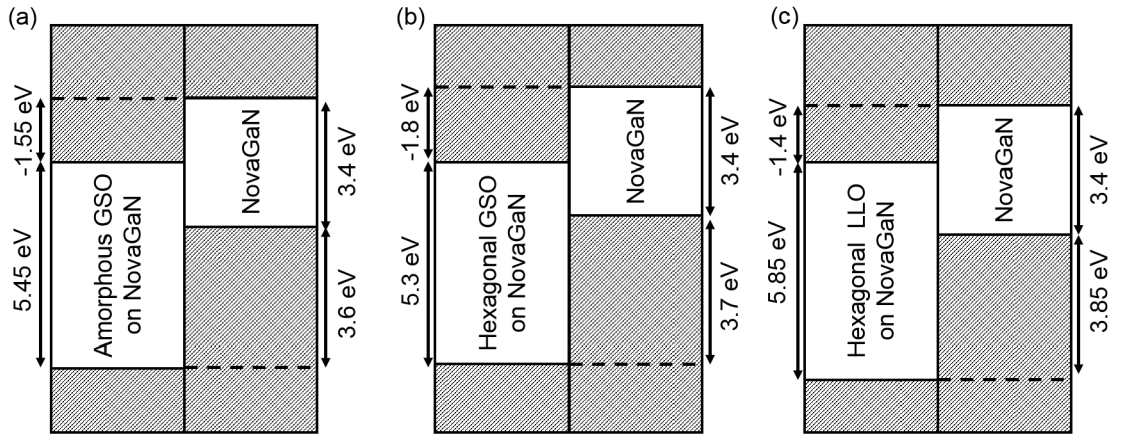

Figure 3.18: Determined band alignment of amorphous GSO (a), hexagonal GSO (b) [49] and hexagonal LLO (c) on NovaGaN.

Table 3.2: Valence band offset (VBO), conduction band offset (CBO) and band gap (E_{gap}) for amorphous and hexagonal GSO, and hexagonal LLO on GaN and NovaGaN

Crystal system	VBO	CBO	E_{gap}
hexagonal GSO on GaN	3.75 ± 0.15	-2 ± 0.15	5.15 ± 0.15
hexagonal GSO on NovaGaN [49]	3.7 ± 0.15	-1.8 ± 0.15	5.3 ± 0.15
amorphous GSO on GaN	3.7 ± 0.15	-2.1 ± 0.15	5 ± 0.15
amorphous GSO on NovaGaN [49]	3.6 ± 0.15	-1.55 ± 0.15	5.45 ± 0.15
hexagonal LLO on NovaGaN	3.85 ± 0.15	-1.4 ± 0.15	5.7 ± 0.15

3.2.3 Structural characterization of rare-earth oxides on GaN

According to ab-initio calculations the hexagonal rare-earth oxides $LaLuO_3$ (LLO) and $GdScO_3$ (GSO) exhibit a non-thermodynamic equilibrium phase [4]. Since X-ray diffraction and diffraction patterns of the layers proof the existence of an hexagonal phase, further structural investigations are necessary, to understand the stabilization

of the hexagonal phase. Therefore, the layers are investigated by transmission electron microscopy, scanning transmission electron microscopy, reciprocal space maps and energy dispersive X-ray spectroscopy. In this thesis only hexagonal and amorphous layers are investigated, so that instead of four indices only three indices are used for lattice planes.

3.2.3.1 $GdScO_3$

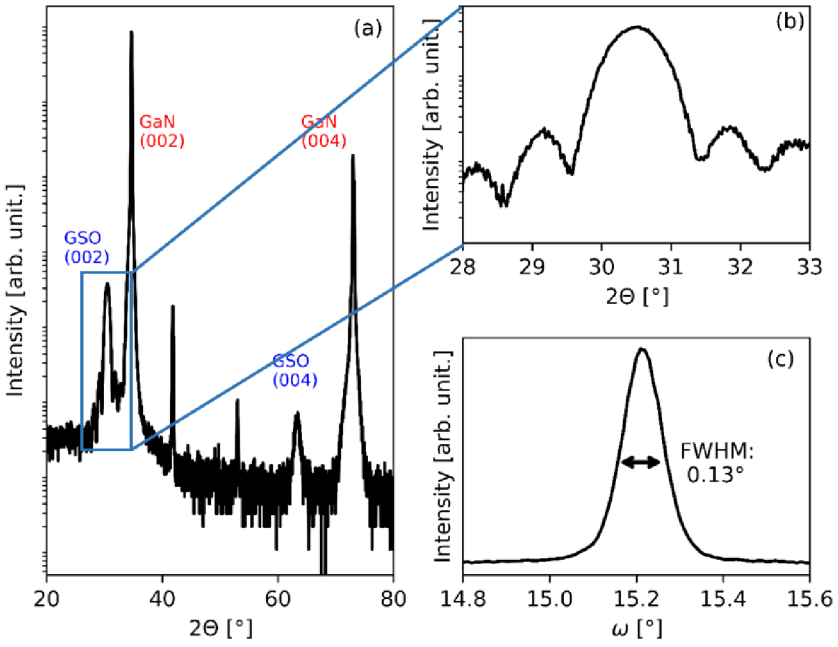

Figure 3.19: (a) XRD $\omega - 2\Theta$ out-of-plane scan showing the (002) and (004) reflections of GaN and GSO. (b) Enlargement of the (002) reflection of GSO showing oscillations and (c) rocking curve of the (002) GSO reflection. Note the different scaling of $q \parallel$ and $q \perp$.

The grown GSO layers are investigated by X-ray diffraction (XRD) in a X-ray diffractometer, to determine the crystal structure and the crystal quality (compare section 2.1.4). In Figure 3.19 (a) an out-of-plane $\omega - 2\Theta$ scan of a 10 nm thick GSO layer on GaN is displayed. The measured intensity is plotted against the angle of the detector (2Θ). Six reflections are identified, from which the ones at 30.5°, 34.6°, 63.3° and 73° are the GSO (002), GaN(002), GSO (004) and GaN (004)

reflections, respectively. The two reflections between 40° and 60° result from the top metal contacts. The out-of plane lattice parameter determined from the XRD measurement is 5.9 Å, which fits to the c-axis of the hexagonal phase of GSO [4]. Thus, the c-axis is perpendicular to the surface, while the a-axis is in-plane and is not determined by this measurement. An enlargement of the (002) GSO reflection is shown in Figure 3.19 (b) revealing layer thickness oscillations besides the main peak in the center at 30.5°. Layer thickness oscillations only occur, if the X-ray reflected at the surface and at the interface interfere. Layer thickness oscillations require an almost perfect crystal and therefore the crystal quality of the GSO layer is high. Since the measurement is out-of-plane and only the reflections along the (00l) direction are measured, the crystal quality is only determined for planes parallel to the surface. To quantify the crystal quality a rocking curve is measured as shown in Figure 3.19 (c). The measured intensity is plotted against ω. The full width half maximum (FWHM) is 0.13°, which is similar to the quality of the GaN substrate.

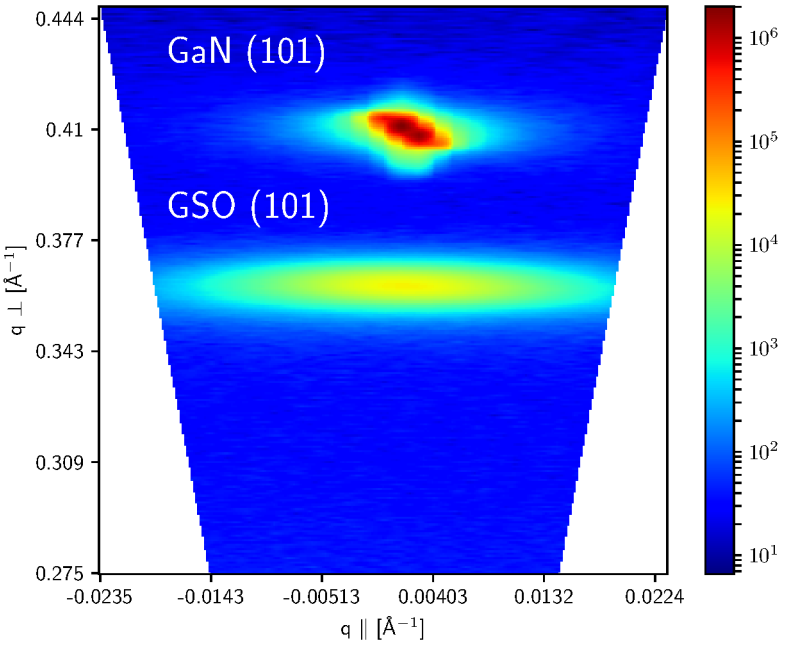

Figure 3.20: Reciprocal space map of the (101) reflection of a 150 nm hexagonal GSO layer and the GaN substrate.

In order to understand the epitaxial relationship between the GaN substrate and the GSO layer and to check the in-plane crystal quality, reciprocal space maps (RSM) of the (101) reflection have been recorded (compare section 2.1.5). In the map shown in

Figure 3.20 the intensity of the GaN (101) and GSO (101) reflection are colour coded and plotted against the parallel ($q \parallel$) and the perpendicular ($q \perp$) reciprocal vectors. The reflections of the GaN is well localized within 0.02 Å^{-1}, which reflects its perfect crystallinity. In contrast, the reflection of the GSO is spread by 0.05 Å^{-1} along $q \parallel$, while the vertical broadening exhibits the same width as the GaN substrate. Thus, the lattice planes parallel to the surface are perfectly ordered. The spread in $q \parallel$ corresponds to the lattice planes perpendicular to the surface, indicating local variations in orientation for example the presence of grains [12]. From the known lattice parameters the reciprocal space vector of a perfect crystal is calculated. In a next step for each deviation of $q \parallel$, the deviation is added to the reciprocal space vector and the angle between the reciprocal space vector of a perfect crystal and the reciprocal space vector with the added deviation is determined and plotted against the intensity of the added deviation of $q \parallel$. The result is a peak function, that is fitted by a Gaussian fit and the FWHM is calculated. The FWHM of the horizontal broadening is 0.12°, which refers to the in-plane tilt of the grains.

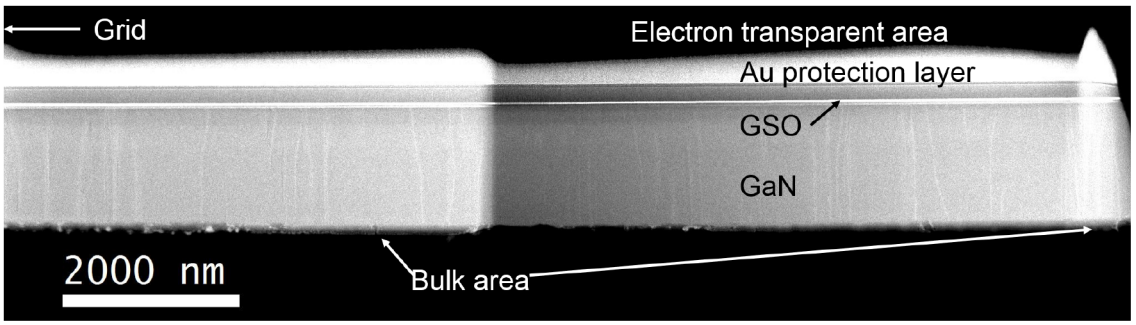

Figure 3.21: Lamella structure of hexagonal GSO on GaN showing the improved structure with bulk areas at the beginning and the end of the lamella. On top of the GSO a Au protection layer is deposited.

A lamella of hexagonal GSO on GaN was investigated by transmission electron microscopy (TEM) and scanning transmission electron microscopy (STEM) with energy dispersive X-ray (EDX) analysis (see Figure 3.21). The lamella was fabricated using the improved lamella structure with a bulk area at the beginning and a smaller one at the end to stabilize the oxide on the GaN. The big bulk area of the lamella is fixed to the grid as indicated by the white arrow in the image. Further, the electron transparent area was reduced to a width of approximately 5 µm. The lamella contains three different materials. The large part at the bottom is GaN, on which the GSO layer is grown. To protect the sample during preparation an Au layer is deposited on top. The Au layer is grown in two steps: A first layer is

deposited by Au evaporation, while the second layer is sputtered on top. Therefore, the layers exhibit a different density, which is visible by the different contrast.

The high-resolution transmission electron microscopy image displayed in Figure 3.22 (a) recorded at an acceleration voltage of 300 kV reveals the atomic structure of the GaN substrate and the GSO film. The GaN is oriented along the $[2\bar{1}0]$ zone axis. While the contrast within the GaN is constant, within the GSO local contrast variations occur. In the upper part a perfect hexagonal pattern is seen. An enlargement of the area is displayed in Figure 3.22 (b). Towards the interface and on the right hand side, only one lattice plane is oriented parallel to the electron beam, indicated by the fringe-like contrast. In accordance grains with different orientations are seen. The interface to the substrate is well defined. However, along the interface the contrast varies due to orientation change. From the oriented hexagonal pattern a fast Fourier transformation (FFT) is calculated and shown in Figure 3.22 (c). The FFT shows the bright spots, which refer to the reciprocal space vectors of the GSO layer, from which the crystal structure and the orientation is determined. The FFT reveals an hexagonal crystal structure and the same orientation as the GaN along the $[2\bar{1}0]$ zone axis.

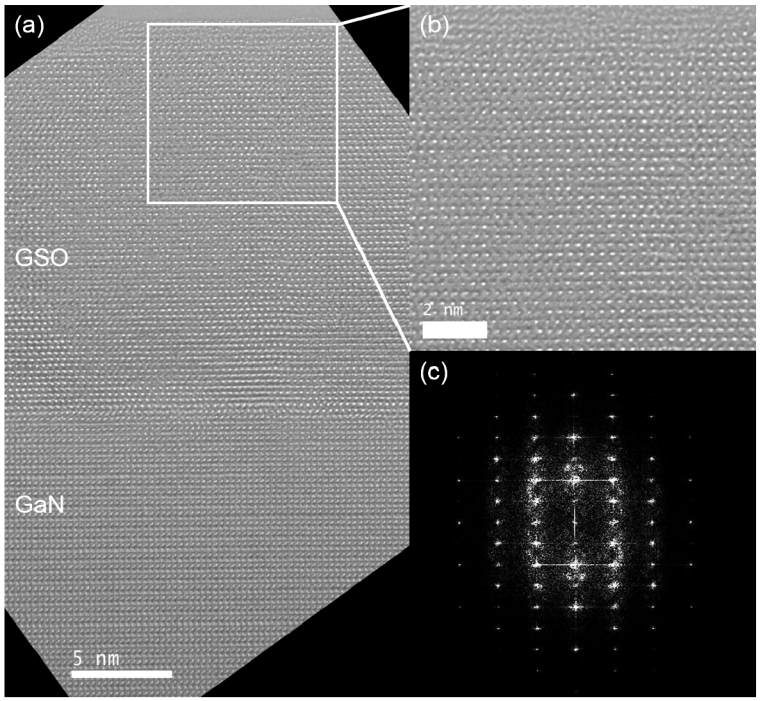

Figure 3.22: HRTEM image of hexagonal GSO on GaN (a). Enlargement of the oriented grain in the GSO (b) and a FFT of the oriented grain (c).

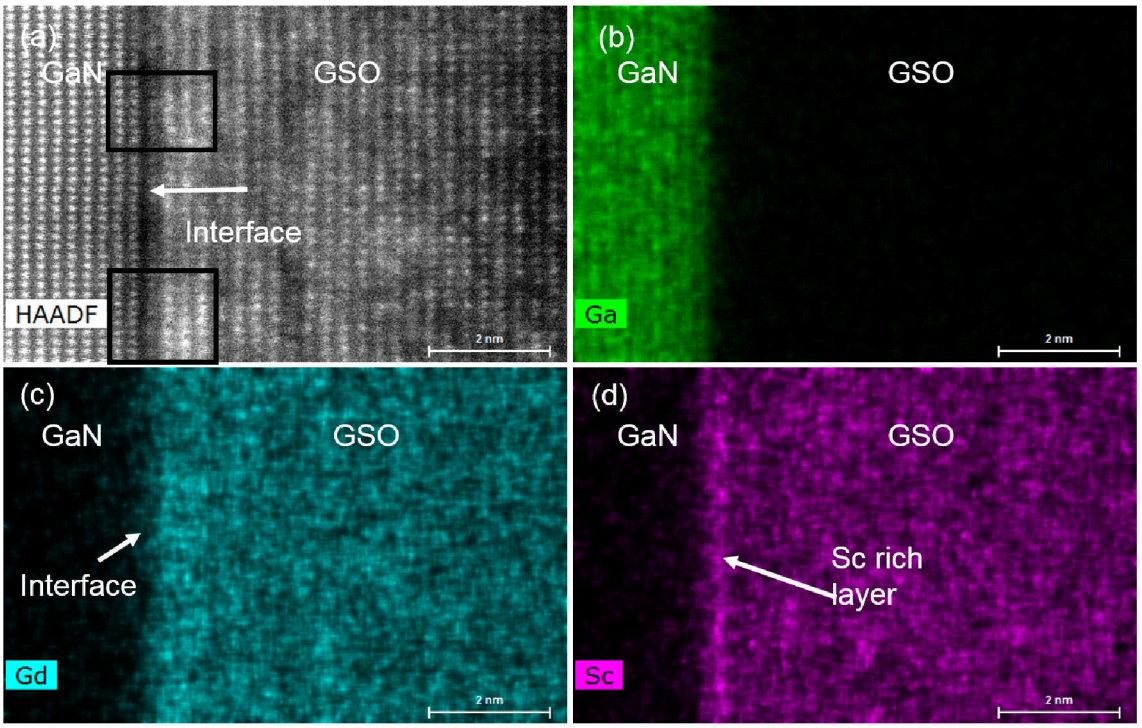

Figure 3.23: (a) HAADF image of hexagonal GSO on GaN. The GSO at the interface exhibits a blurry contrast, except at two regions, where individual atoms are identified (black boxes). EDX distribution maps of the elements Ga (b), Gd (c) and Sc (d).

In order to access the local chemical composition energy dispersive X-ray (EDX) spectra and high angle annular dark field (HAADF) images were recorded simultaneously. Due to the large angle of the detector only electrons scattered into large angles are visible. Since the scattering of electrons scales approximately proportional to $Z^{1.7}$, heavier atoms are brighter [16]. The lamella was investigated at an accelerating voltage of 200 keV and remained stable during the investigation. An HAADF image of the investigated region is shown in Figure 3.23 (a). The atom positions of the Ga in the [010] oriented GaN are seen on the left, whereas the N is invisible due to its low atomic number. While the GaN is oriented along the zone axis, the GSO exhibits regions with different orientation. The contrast in the GSO varies, but the individual atoms are visible, although the contrast becomes blurry in the first three atom rows at the interface, indicating changes in orientation. At two regions at the interface (indicated by black boxes in Figure 3.23) the GSO is oriented and individual atoms are identified, while the residual interface region is smeared. At the interface a dark layer is visible, followed by three brighter atom

rows. Since HAADF imaging is sensitive to atomic mass, heavier atoms appear brighter. Thus, at the interface a lighter element is expected, while the following three atom rows exhibit heavier elements. After the three bright atom rows the GSO appears homogeneous, since the difference in contrast is smaller compared to the interface and the three following atom rows.

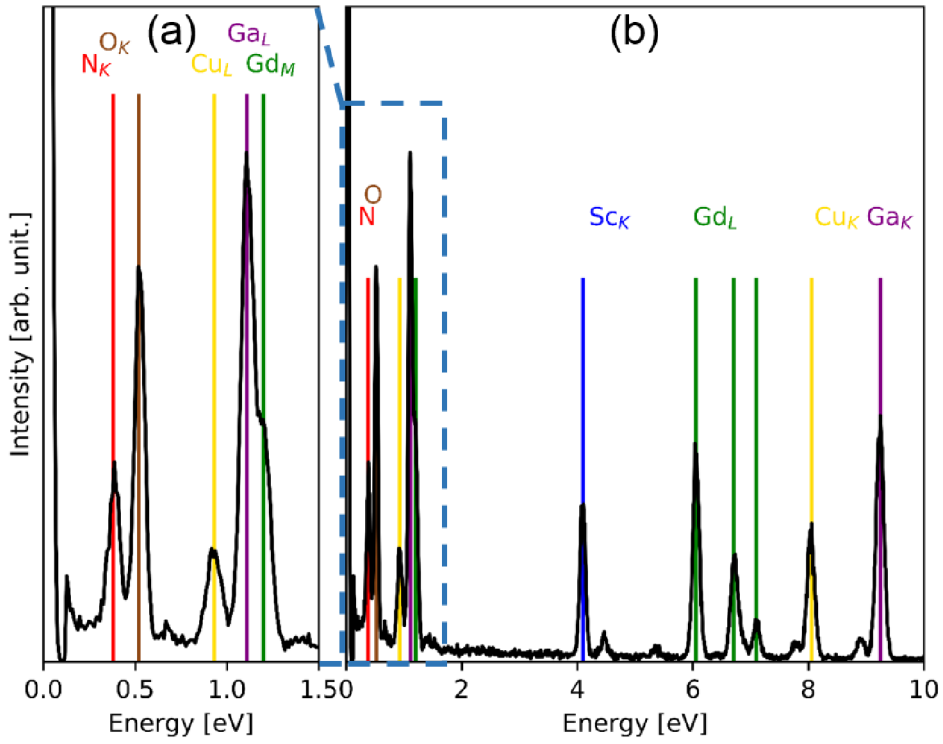

Figure 3.24: (a) EDX spectra in the region from 0 to 1.5 eV. (b) Energy dispersive X-ray spectrum of GSO on GaN revealing the characteristic X-ray energies for N, O, Sc, Gd, Cu, and Ga.

For the EDX measurement the area shown in the HAADF is measured and the characteristic X-rays were recorded up to 20 keV. In Figure 3.24 the EDX spectrum of the whole image is shown and the measured intensity is plotted against the energy of the X-rays. The characteristic X-ray energies for N, O, Sc, Gd, Cu and Ga are colour-coded. Besides the expected elements, Cu is identified, which is a background signal arising from the grid, the lamella is attached to. In Figure 3.23 (b-d) the qualitative EDX intensity distribution maps are shown for the characteristic X-ray

energies of the Ga K line, the Gd L line and the Sc K line, respectively. On the left hand side of the interface Ga but neither Gd nor Sc are detected and vice versa to the right hand side of the interface. Thus, Ga does not diffuse into the GSO neither do Gd or Sc diffuse into the GaN. In the EDX distribution map of Sc a higher intensity of the characteristic X-rays of Sc is detected at the interface (Figure 3.23 (d)). Since Sc is lighter than Gd, the larger Sc content at the interface fits to the darker contrast in the HAADF at the interface.

The measured EDX intensities of the Gd, Sc and Ga are qualitatively evaluated. Each pixel in the EDX map contains an EDX spectrum, but the measured intensities of the characteristic X-rays are to weak for evaluation. Therefore, the EDX intensities of all pixels on a line parallel to the interface are summed up to improve the signal to noise ratio. The Ga intensity is normalized to the average intensity of Ga in the first nm and the Gd and Sc intensity is normalized to the Gd and Sc intensity of the last nm of the measured area. The resulting intensities of the Gd, Sc and Ga are displayed as a linescan over the HAADF image of the measurement area in Figure 3.25 (a). In the linescan the atomic resolution of the EDX intensities is visible by the Ga peaks, corresponding to the positions of the atom rows of Ga. The Ga intensity at the interface decreases from 90% of its value in the GaN to 10% within 0.5 nm, thus a sharp interface exists. The Gd and Sc characteristic X-ray intensities are about zero in the GaN. The Sc intensity increases from the GaN in the direction of GSO before the one of Gd. At the interface the Sc intensity reaches a 2.5 times larger intensity compared to the average one, while the Gd intensity is below the average. At the first atom row the Gd exhibits a larger and the Sc a lower intensity compared to the average. 2 nm away from the interface into the GSO the intensities of Gd and Sc are about average. The larger Sc and Gd intensity are reflected in the HAADF by a brighter contrast of the first atom row of GSO at the interface compared to the GSO 2 nm away from the interface.
The EDX intensities of Sc and Gd were used to quantitatively determine the Gd / Sc ratio perpendicular to the interface. The investigated area is about 12 x 6 nm^2, so that a constant thinning is to be expected. Hence, the investigated area exhibits a constant thickness, so that changes in the EDX intensities due to thickness variations are excluded and only occur due to changes in the chemical composition. In the linescan in Figure 3.25 (a) 2 nm away from the interface into the GSO the Gd and the Sc intensity reveal a constant value. Because Rutherford backscattering spectrometry as well as the pulsed laser deposition target reveal a Gd / Sc ratio of 1:1, the amount of Gd and Sc 2 nm away from the interface are defined equal. In this area the intensity of the characteristic X-ray of Gd were integrated in the range from 5.8 eV to 6.3 eV and of the Sc in the range from 3.92 eV to 4.25 eV, and their ratio is defined as reference for a 1:1 composition. Subsequently, the Gd / Sc ratio for each line of the linescan was calculated and normalized to this reference. The resulting ratio is plotted against the position of the line as shown in Figure 3.25

(b) laid over the HAADF image of the investigated area. On the left side of the HAADF image the GaN is shown. In this area the Gd / Sc ratio is not determined, since neither Sc nor Gd intensities were measured.

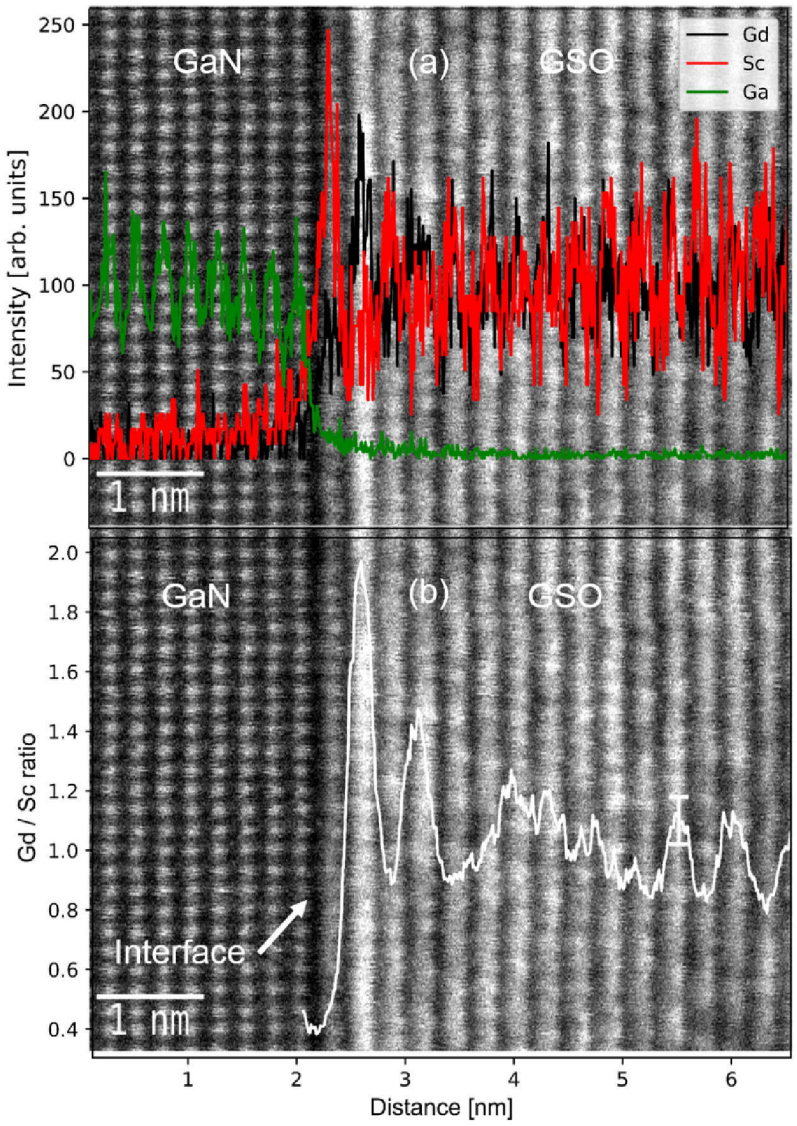

Figure 3.25: Linescan of the characteristic X-ray intensities for Gd (green), Sc (red), Ga (blue) (a) and quantitative analysis of the Gd / Sc ratio from the linescan (b) over a HAADF image showing the measuring area.

Beginning at the interface the Sc and Gd signals were recorded and the Gd / Sc ratio was calculated. At the interface the Gd / Sc ratio is about 0.4 and the HAADF image shows a dark contrast compared to the GSO away from the interface. Within

the following atom rows in the GSO an increased Gd / Sc ratio is measured. It amounts up to twice larger ratio than in the bulk, revealing twice as much Gd than Sc. Due to the larger atomic mass of the Gd than the Sc the HAADF image reveals bright atom rows. Further EDX investigation of the oxygen revealed a very noisy signal, since ionisation cross sections are small. Within the margin of error no local variations in oxygen within the GSO are detected.

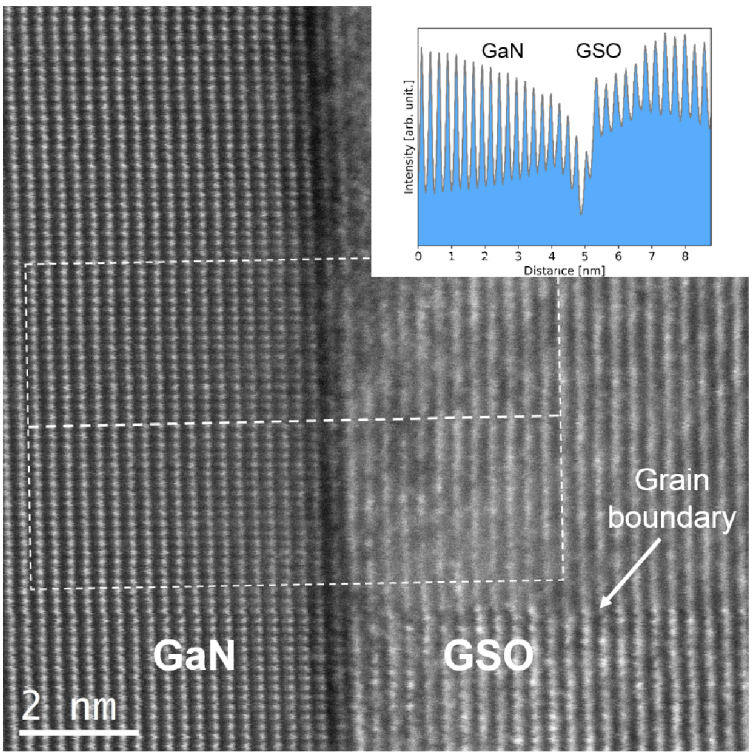

Figure 3.26: HAADF image of hexagonal GSO on GaN with the area marked for the linescan of the signal intensity. In the inset the signal intensity of the linescan is shown, revealing the positions of the lattice planes parallel to the interface of the GaN and the GSO.

Besides the change in contrast, an enhanced distance in between the atom rows at the interface in between the GaN and the GSO is visible in the HAADF image in Figure 3.25. The distance in between the atom rows is calculated from the HAADF image as shown in Figure 3.26. On the left hand side the GaN is visible and on the right hand side the GSO is displayed, in which two different grains can be distinguished by a change in orientation and consequently a change in contrast. The grain boundary is indicated by a white arrow in Figure 3.26. The signal intensity along a line parallel to the interface were summed up and plotted against the position of

the line. The area for the measurement is indicated by white lines in Figure 3.26 and the plotted intensities against the positions are shown in the inset. Therefore, the intensity summed up along those lines, that are on a lattice plane, reveal a large signal intensity, while those lines in between the lattice planes show a low signal intensity. In the inset of Figure 3.26 the determined intensity is plotted against the position of the line, displaying peaks, which correspond to the center of the lattice planes. To determine the exact position of the center of the peak, a Gaussian is fitted. The distance between two maxima reflects the lattice plane distance. The determined distances are 0.26 ± 0.001 nm, 0.29 ± 0.002 nm for the GaN and GSO atom rows, respectively. The determined distances matches to the c-axis of hexagonal GaN and to the length of the c-axis of hexagonal GSO determined by XRD. At the interface a distance of 0.31 nm is identified, which is larger than the c-axis of GaN or GSO.

Depending on the substrate temperature during the growth the GSO exhibits different crystal structures on the GaN. For high temperatures of approximately 650 °C the GSO becomes hexagonal, while at room temperature the GSO is grown amorphous. The local chemical composition of the amorphous GSO grown on GaN was investigated by high angle annular dark field (HAADF) images, while energy dispersive X-ray (EDX) measurements were performed by scanning transmission electron microscopy (STEM). The properties of the amorphous GSO were compared to the ones of hexagonal GSO. In contrast to the hexagonal GSO the amorphous GSO is destroyed by electron irradiation at an accelerating voltage of 200 kV and therefore needs to be investigated at 80 kV.

HAADF images obtained at 80 kV are shown in Figure 3.27 with the GaN oriented along the $[2\bar{1}0]$ zone axis. The upper images are recorded at position 1 and display the same area before (a) and after (b) the EDX measurement. Before the EDX measurement (Figure 3.27 (a)) the GSO reveals a bright layer at the interface, above which darker spots are visible. The layer is amorphous and does not reveal any crystalline area, although some small crystals in the darker area could be surmised. In Figure 3.27 (b) the same area as in (a) is shown, but after the EDX measurement. Due to sample drift during the measurement, the sample is slightly displaced. A red cross in the images marks the same position on the lamella. In the image after the EDX measurement the GSO layer has changed. The dark spots in the upper and lower part of the image are faded, but the layer is still amorphous. The brighter layer at the interface is still present. In Figure 3.27 (c and d) a different position on the same lamella is shown, revealing a crystalline grain (indicated by the white circle) at the interface in the GSO. The stacking sequence is ABC, so that the crystal seems to be cubic and the distance in between the atom rows is 0.3 nm. The grain and the brighter layer at the interface exists before and after the EDX measurement. A change of the amorphous part is not visible.

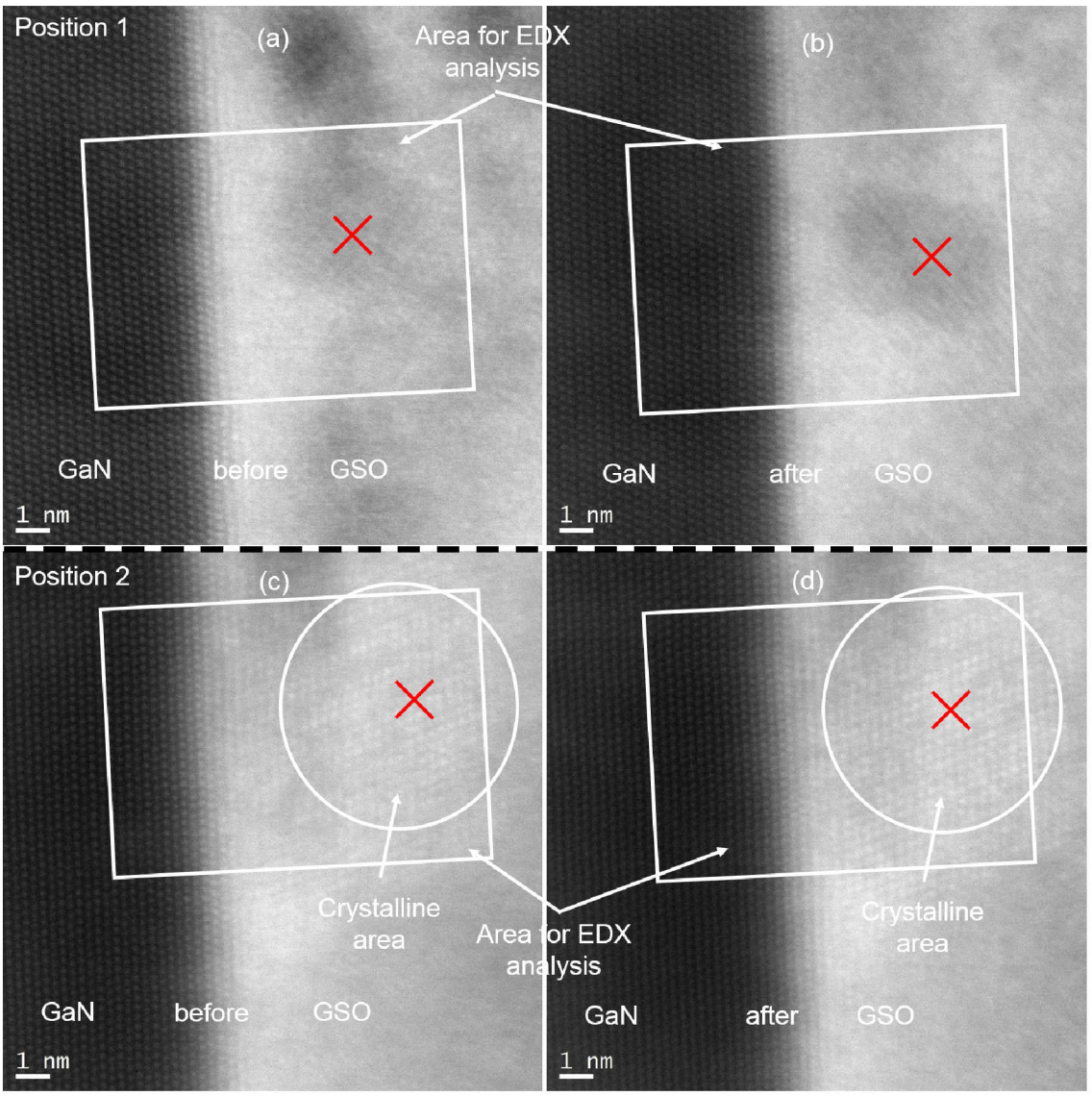

Figure 3.27: HAADF image of amorphous GSO deposited on GaN at room temperature without a crystalline grain before (a) and after (b) the measurement and with a crystalline grain before (c) and after (d) the measurement.

EDX spectra are recorded in areas with amorphous and crystalline GSO, respectively, as indicated by the white boxes in the HAADF images in Figure 3.27. A linescan of the determined EDX spectra is shown in Figure 3.28 for the amorphous region (a) and the crystalline region (b). Above the plotted linescan a section of

the investigated area is displayed. No significant difference of the two linescans is visible. In the GaN only the Ga exhibits a large intensity, while the Gd and Sc X-ray intensity is about 0. In the GSO the only characteristic X-ray signals are from the Gd and the Sc atoms. Further, the intensity of the Gd and the Sc increase parallel to each other from the GaN into the GSO. Thus, independent of the region no decomposition of Sc or Gd occurs in GSO deposited at room temperature. The Ga intensity at the interface decreases from 90% of its maximum value to 10% of its maximum value within 1.5 nm.

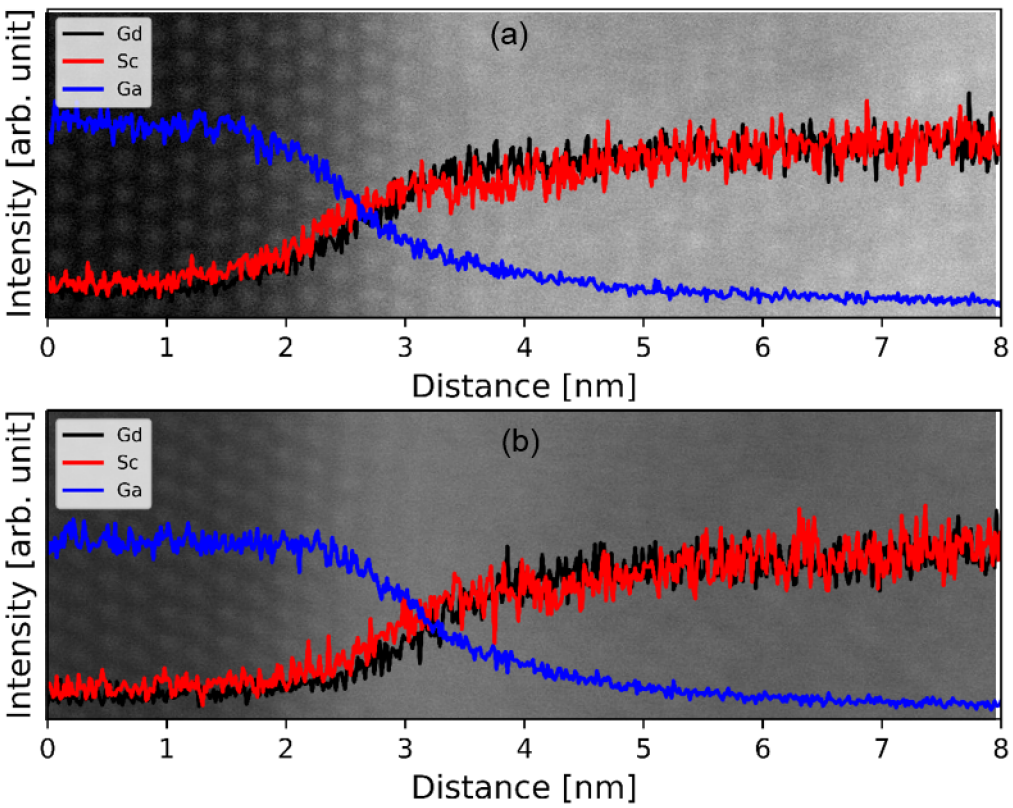

Figure 3.28: Linescan of amorphous GSO on GaN with the EDX intensities of Gd (black), Sc (red) and Ga (blue) in the amorphous region (a) and in the crystalline region (b).

3.2.3.2 $SmScO_3$

$SmScO_3$ (SSO) is another ternary rare-earth scandate, that reveals the hexagonal phase, when grown at elevated temperatures by pulsed laser deposition. In the following the crystal structure and the chemical composition of the SSO layers were investigated and compared to the hexagonal GSO. In Figure 3.29 (a) a $\omega - 2\Theta$ scan is shown. The reflection at 32.5° and 68° are the (101) and (202) reflection of SSO, respectively, and the reflections at 36° and 78.4° are the (101) and (202) reflection of GaN, respectively. The reflections of the SSO reveal the lattice parameters of hexagonal SSO found in literature (a=3.6 Å and c=5.9 Å [4]). In Figure 3.29 (b) the rocking curve of the (002) reflection of SSO is determined. The FWHM is 0.13°, which is in the same range as the underlying GaN and reveals a good crystal quality.

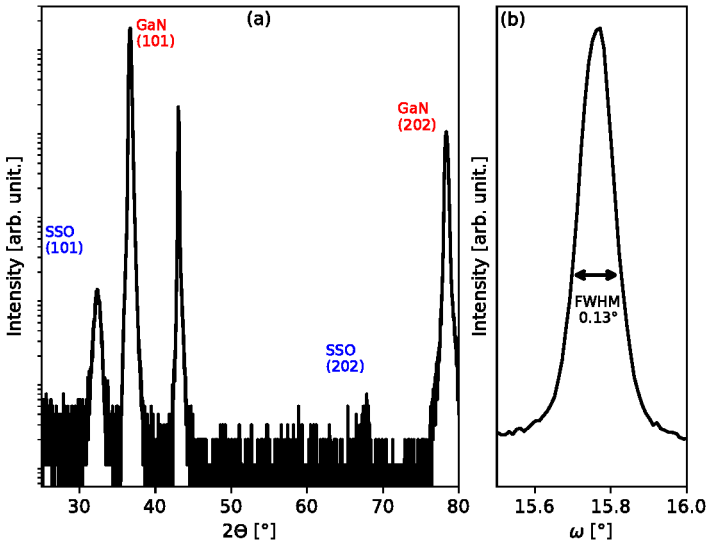

Figure 3.29: (a) XRD $\omega - 2\Theta$ scan revealing the (101) and (202) reflections of GaN and $SmScO_3$. (b) Rocking curve of the (002) $SmScO_3$ reflection.

To investigate the chemical composition, especially at the interface HAADF images and EDX spectra are simultaneously recorded. In Figure 3.30 (b) a HAADF image recorded at 200 kV is shown, displaying the GaN substrate, the interface and the SSO oxide. The GaN is oriented along the $[2\bar{1}0]$ zone axis and the Ga atoms are visible. The lattice planes of the SSO parallel to the interface run from the left side of the image to the right side and are easy to distinguish. Hence, the SSO reveals a high quality crystal growth in the out-of-plane direction in agreement with XRD

(compare Figure 3.29). The contrast pattern of the lattice planes varies over the whole width (50 nm) of the HAADF image. The contrast fluctuations on a 10 nm scale seen within the SSO layer arise from thickness fluctuations of the FIB lamella, which is called curtaining effect. Further, a variation of the contrast results from the tilt of the grains along the c-axis. On the left hand side and on the right hand side of the image individual atoms of the SSO are distinguished (indicated by the black box in Figure 3.30 (b)), of which an enlargement is shown in Figure 3.30 (a). In between the oriented areas the contrast is blurry.

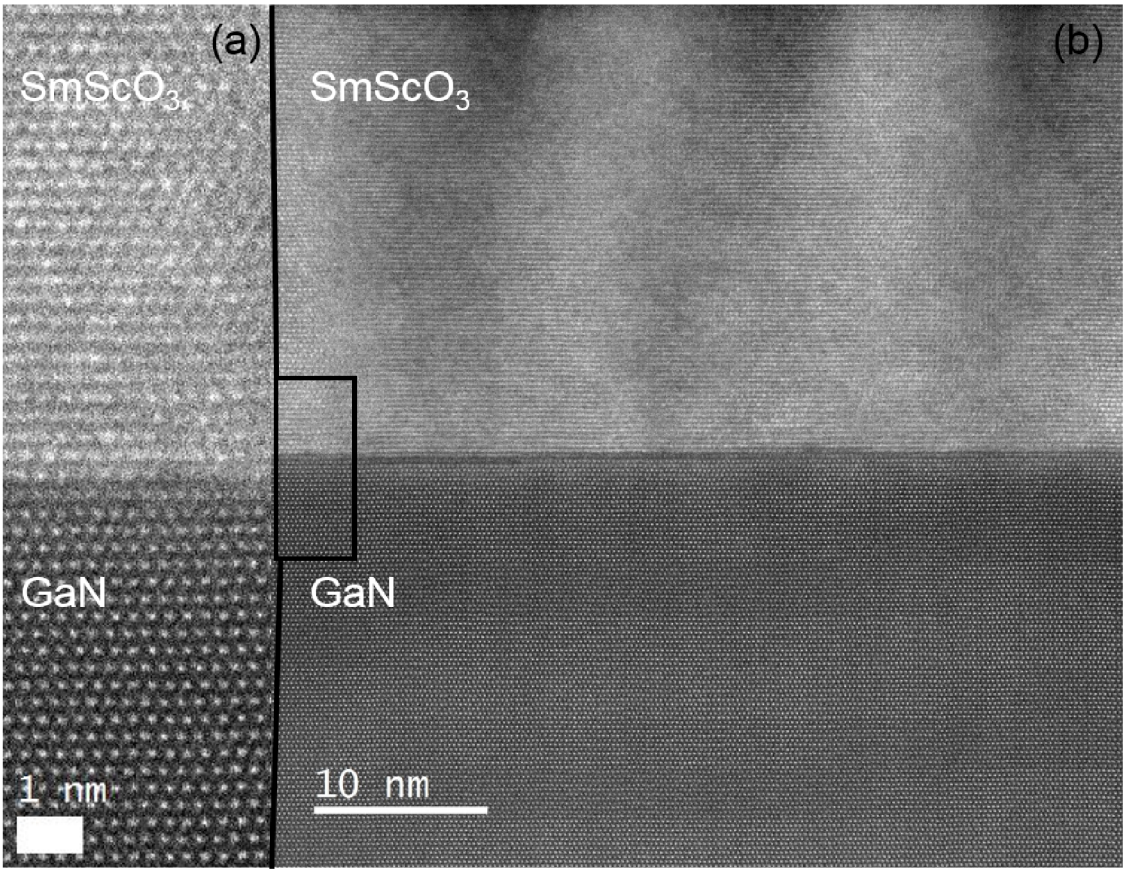

Figure 3.30: (a) Enlargement of the oriented SSO region. (b) HAADF image of hexagonal SSO on GaN revealing an enhanced distance and a dark contrast at the interface.

The inter-atomic distance at the interface of SSO grown on GaN is determined the same way as for the hexagonal GSO (section 3.2.3.1). The measured distance of the atom rows is 0.26 nm, 0.29 nm in the GaN and the SSO, respectively. The measured

lattice distance in the SSO fits to the length of the c-axis of the SSO determined by XRD, so that this axis is perpendicular to the interface. The interface between the SSO and the GaN exhibits a distance of 0.31 nm and is larger than the c-axis of the SSO and the GaN. At the interface a dark line is visible over the total width of the HAADF image, which can result from changes in the chemical composition. Therefore, EDX spectra are recorded at an accelerating voltage of 200 kV up to an X-ray energy of 20 keV.

In Figure 3.31 an EDX spectrum of the SSO film on GaN is displayed. The measured intensity of the X-rays is plotted against their energy. Besides the characteristic peaks of GaN and $SmScO_3$ a Cu signal is detected, which is caused by the Cu grid the lamella was mounted on. Below an energy of 2 eV the characteristic X-rays of O, N, Cu and Ga are visible. Above an energy of 3 eV the characteristic Sc_K, Sm_L, Cu_K and the Ga_K occur in this order, which are used for further analysis except for Cu.

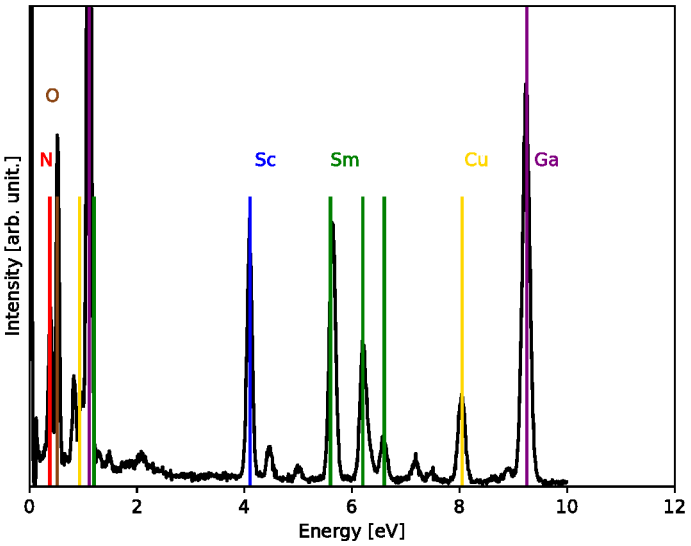

Figure 3.31: Energy dispersive X-ray spectrum of SSO on GaN revealing the characteristic X-ray energies for N, O, Sc, Sm, Cu, and Ga.

For the EDX maps an EDX spectrum of the area shown in the HAADF image in Figure 3.32 (a) is measured for each pixel. In the HAADF image the GaN is on the left hand side and the SSO on the right hand side. In the GaN individual atoms are recognisable, which is oriented along the $[2\bar{1}0]$ zone axis. In the SSO, lattice planes parallel to the interface are visible, and individual atoms are distinguishable. The

first three atom rows are blurry in comparison to the remaining SSO. In the upper half the contrast becomes blurry, because the orientation of the SSO is changed. In Figure 3.32 (b-d) the intensity of the Sc, Sm and Ga signal for each pixel is colour-coded over the investigated area. The Sc and the Sm signal are most intense in the SSO, but still some EDX signal of Sm is detected in the GaN, which results from noise during the measurement. Still the EDX signals of Sc, Sm and Ga do not show an abrupt decrease at the interface.

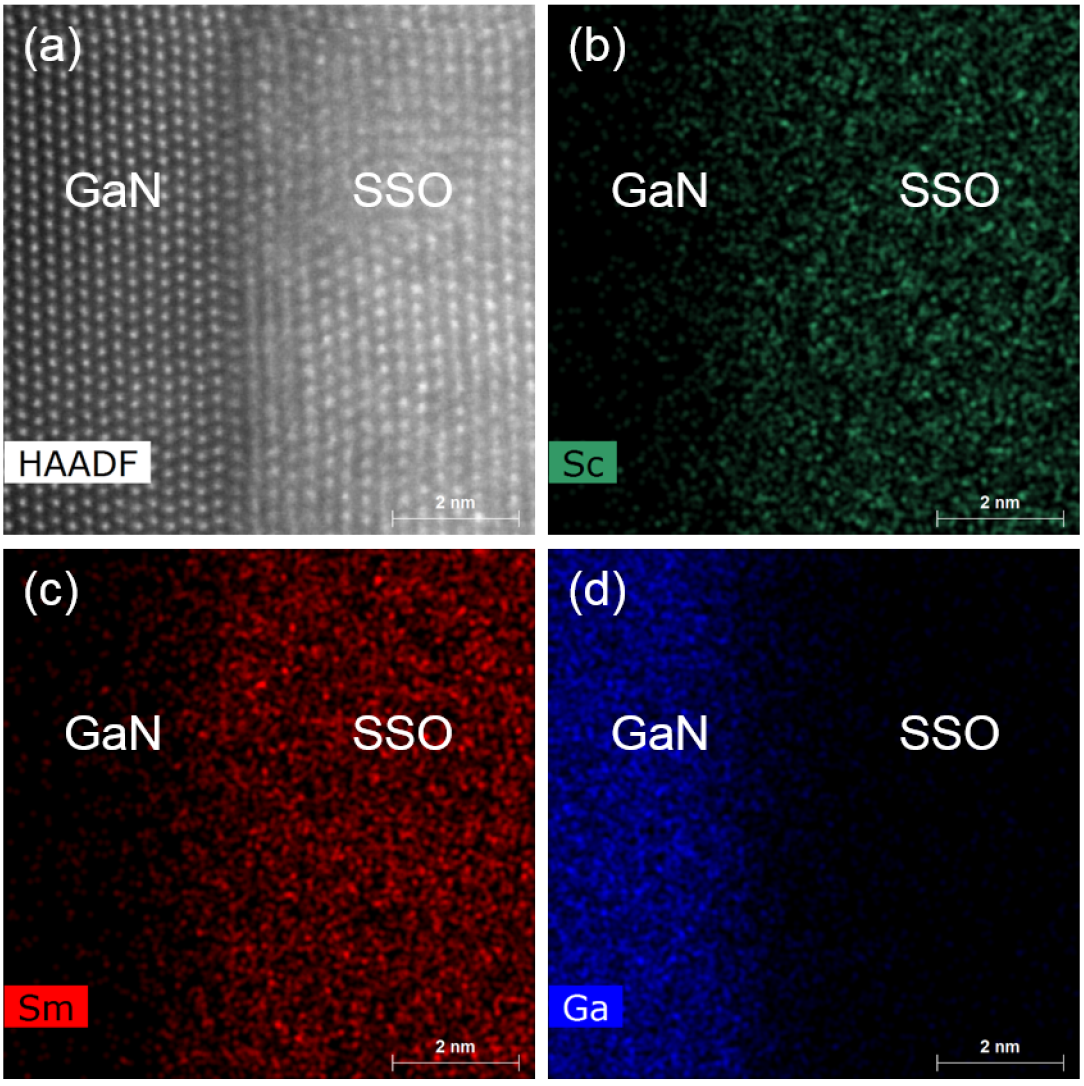

Figure 3.32: HAADF image of the investigated area (a). EDX maps of Sc (b), Sm (c) and Ga (d).

From the EDX maps the EDX intensities of each pixel on the lines parallel to the

interface were summed up and normalized. The intensities of the Sm_L, Sc_K and Ga_K line are plotted against the horizontal position of the line in the measurement area as displayed in Figure 3.33. The two linescans are measured on the same sample at different positions. In the Ga signal peaks are identified, which correspond to the positions of the Ga atoms. The Sm and Sc signal are about 0 in the GaN and increase at the interface. The first linescan (Figure 3.33 (a)) exhibits an increased Sc intensity at the interface, which is larger than the Sm one at the interface and the average one of Sc in the SSO. Further, the Sc intensity increases earlier and steeper than the one of Sm. Few nm away from the interface the Sc and the Sm intensity are similar. Thus, at the first position the SSO layer exhibits a Sc rich interface.

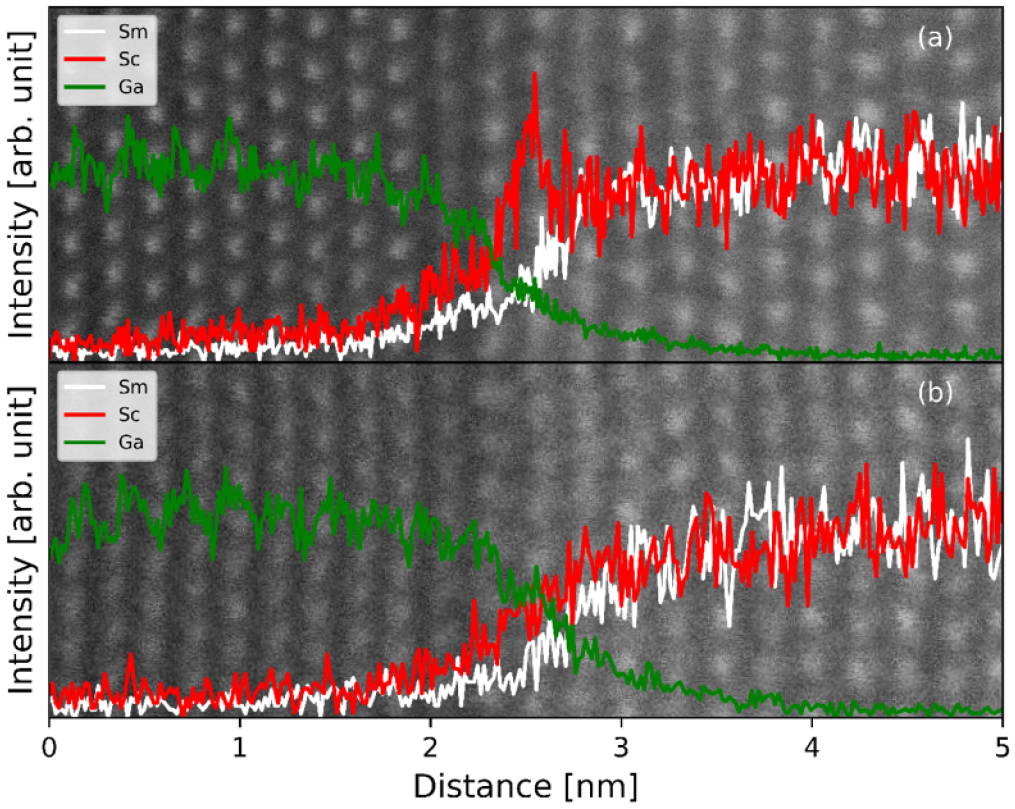

Figure 3.33: Linescan of hexagonal SSO on GaN at two different positions with the intensities of Sm, Sc and Ga plotted: (a) SSO exhibiting increased Sc concentration and (b) only slightly increased Sc concentration at the interface.

In contrast the second linescan reveals only a slight increase of the Sc intensity at the interface, which can be deduced from the shift to the left of the red curve with respect to the white one. The Sm and the Sc intensity increase at the interface with the same slope. Hence, along the interface local variations of the Sc concentration occur. However, everywhere the region close to the interface is rich in Sc. At the interface the Ga signal decreases from 90% of its intensity to 10% within 1.5 nm from the GaN into the SSO. The intensity of the Sc and the Sm signal increases from 10% of its average intensity up to 90% within 1.5 nm. As already seen in the EDX maps (compare Figure 3.32) the Ga diffuses into the SSO and the Sm and the Sc into the GaN.

3.2.3.3 $LaLuO_3$

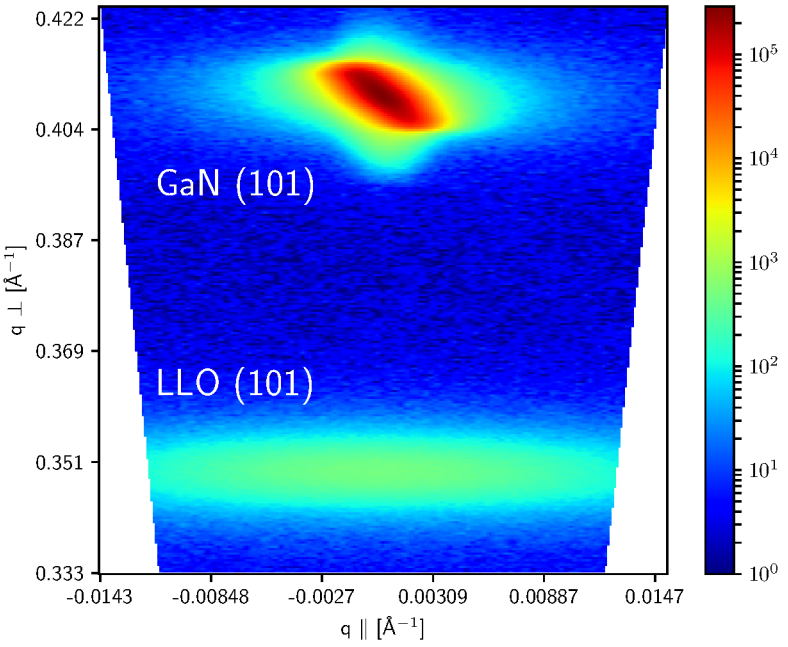

Figure 3.34: RSM of the (101) reflection of 26 nm thick hexagonal LLO and the GaN substrate.

To determine the crystal quality in-plane and out-of-plane of the hexagonal $LaLuO_3$ (LLO) film on GaN a reciprocal space map (RSM) along the (101) reflection of a 26 nm thick LLO oxide and the GaN substrate was recorded as shown in Figure 3.34.

The reflection of the GaN is visible above the one of LLO. The vertical broadening of the LLO is 0.02 $Å^{-1}$, which is in the same range as GaN (0.02 $Å^{-1}$). The horizontal broadening of the LLO is 0.05 $Å^{-1}$ and thus 5 times larger as the one of GaN 0.01 $Å^{-1}$ and 2.5 times larger as the vertical broadening. The increased horizontal reflection is related to titled grains in the hexagonal LLO layer [12]. From the measured data the full width half maximum (FWHM) of the horizontal broadening in degrees is calculated as for the hexagonal GSO in subsubsection 3.2.3.1.
The FWHM of the horizontal broadening is 0.17°.

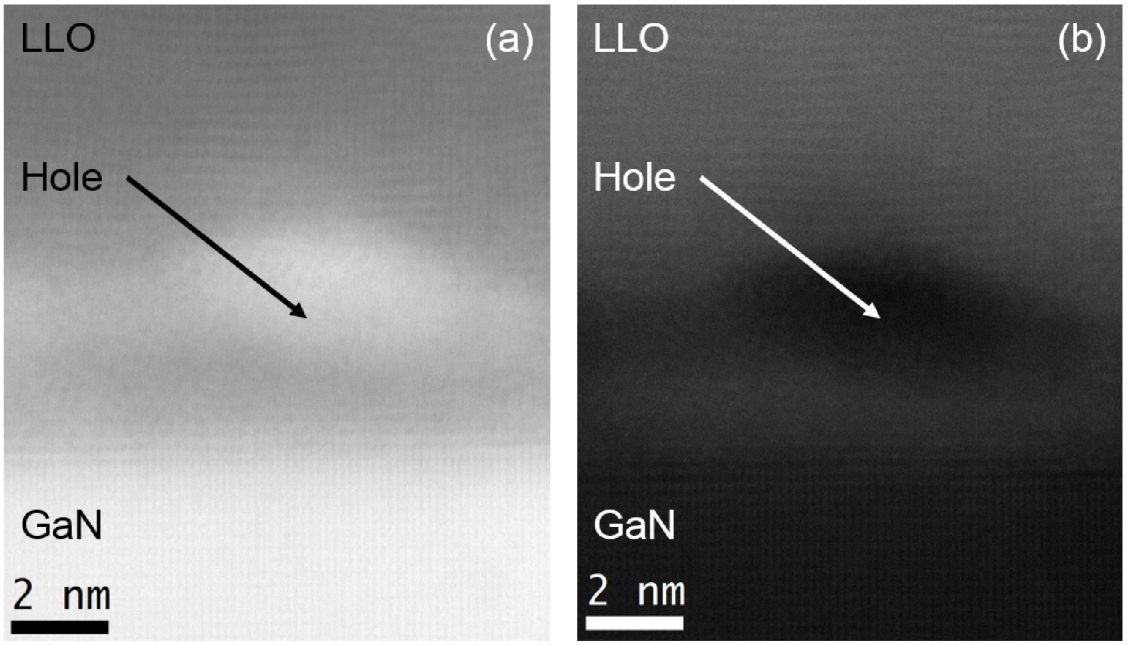

Figure 3.35: Bright field (a) and HAADF (b) image of the interface between hexagonal LLO and GaN.

In order to investigate the chemical and structural composition of hexagonal LLO on GaN the grown layers were analysed by high angle annular dark field (HAADF) images at an accelerating voltage of 200 kV, while energy dispersive X-ray (EDX) spectra were recorded simultaneously. The interface between LLO and GaN was investigated to analyse the chemical composition and the structure. In Figure 3.35 a bright field (BF) and a HAADF image of the interface is displayed. At the bottom of the image the GaN is shown, which is orientated along the $[2\bar{1}0]$ zone axis. On top the hexagonal LLO is grown. At the interface a layer with a width of 5 nm with a blurry contrast is visible. The layer exhibits no crystalline structure and seems to be amorphous. Further, a bright spot in the BF image and a dark spot

in the HAADF image are present. Thus, in this spot less electrons are scattered, so that more electrons hit the BF detector than the HAADF detector, compared to the ambient area, i.e. this area comprises a reduced thickness. Above the blurry layer the crystalline structure of the LLO is visible. Hence, the amorphous areas of reduced thickness occur during investigation by scanning transmission electron microscopy, by which the crystalline interface is destroyed. A destruction of the interface during the growth by pulsed laser deposition is excluded, because if an amorphous layer is formed at the interface, no epitaxial growth above is possible, which, however, has been proven by XRD.

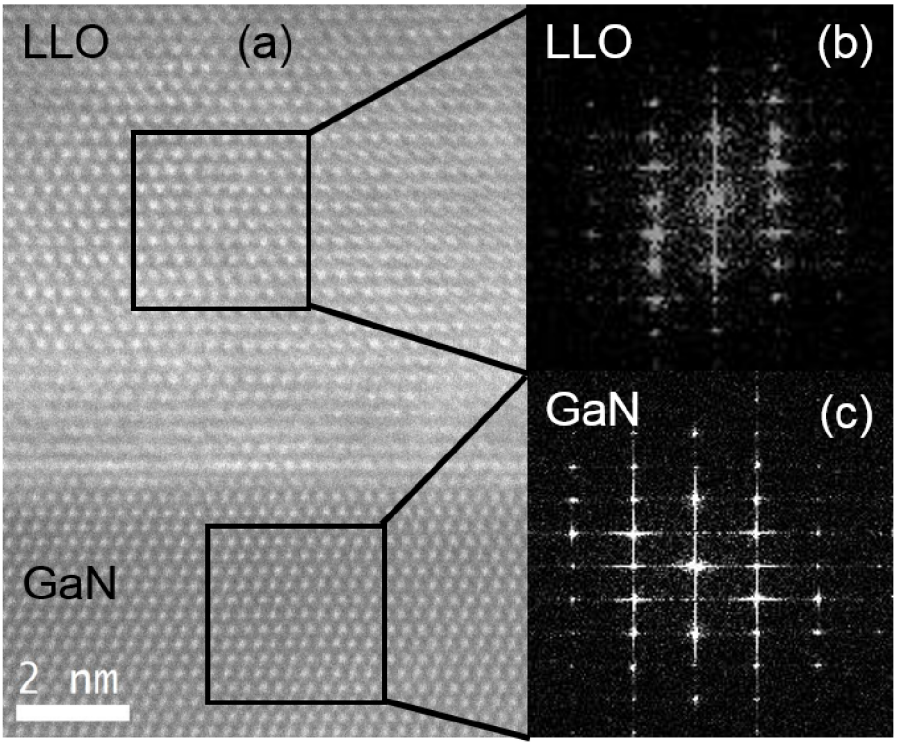

Figure 3.36: HAADF image obtained at 80 kV of hexagonal LLO on GaN with a crystalline interface (a). Fast Fourier transformation of the crystalline LLO (b) and of the GaN (c).

To prevent damage of the lamella the accelerating voltage was reduced to 80 kV. In Figure 3.36 (a) a HAADF image of the hexagonal LLO on GaN is shown. The GaN at the bottom of the image is oriented along the $[2\bar{1}0]$ zone axis and individual atoms are visible. The LLO layer above the GaN reveals a region, which is oriented along a low index zone, too, because individual atom columns are identified. At the interface the contrast becomes blurry, but still individual atoms can be recognized and at least the lattice planes parallel to the interface are distinguishable.

Thus, the interface is crystalline and does not exhibit any hole, so that the areas of reduced thickness observed in the HAADF image recorded at 200 kV are beam induced damage. From the oriented grain in the LLO a fast Fourier transformation (FFT) is calculated and displayed in Figure 3.36 (b). In the FFT spots are visible, which correspond to the spatial frequencies. In Figure 3.36 (c) the FFT of the GaN is shown, which exhibits the same pattern as the one of the hexagonal LLO. Thus, the FFT calculated from the LLO matches to an hexagonal pattern with the same orientation as the GaN.

To determine the chemical composition across the interface EDX spectra were recorded. The investigated area is shown in the HAADF image in Figure 3.38 (a). The recorded EDX spectrum over the whole image is shown in Figure 3.37. The La_L, the Lu_L and the Ga_K line are used for further analysis.

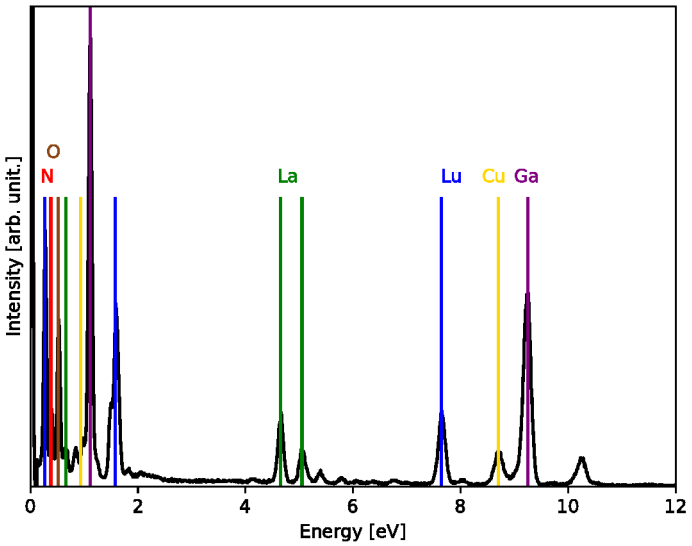

Figure 3.37: Energy dispersive X-ray spectrum of LLO on GaN revealing the characteristic X-ray energies for N, O, La, Lu, Cu, and Ga.

In the overview image of the EDX maps (see Figure 3.38 (a)) the GaN, oriented along a low-index zone, is visible at the left hand side of the image. At the right hand side the LLO is displayed. The brightness of the LLO is reduced from the left hand side to the right hand side, which is caused by a reduction in thickness. While individual atom columns can be identified in the LLO away from the interface, the contrast of the LLO at the interface is blurred. Further, the individual atoms are distinguishable in the LLO, while at the interface the contrast becomes blurry, indicating a change of

orientation, which could result from tilted grains. In Figure 3.38 (b-d) for each pixel in the HAADF image, the measured intensity of the characteristic X-rays of Ga, La and Lu are shown, respectively. The Ga intensity in Figure 3.38 is concentrated in the area of the GaN, while only little intensity is measured in the LLO region. The La and Lu in Figure 3.38 (c) and (d) exhibit small intensity in the GaN region and in the LLO the intensity of both is larger. At the first 3 nm from the interface into the LLO the intensity of La as well as of Lu is homogeneous. Further, to the right side, the intensity of the characteristic X-rays is reduced, because due to the lower thickness less electrons scatter inelastically and consequently less characteristic X-ray are generated.

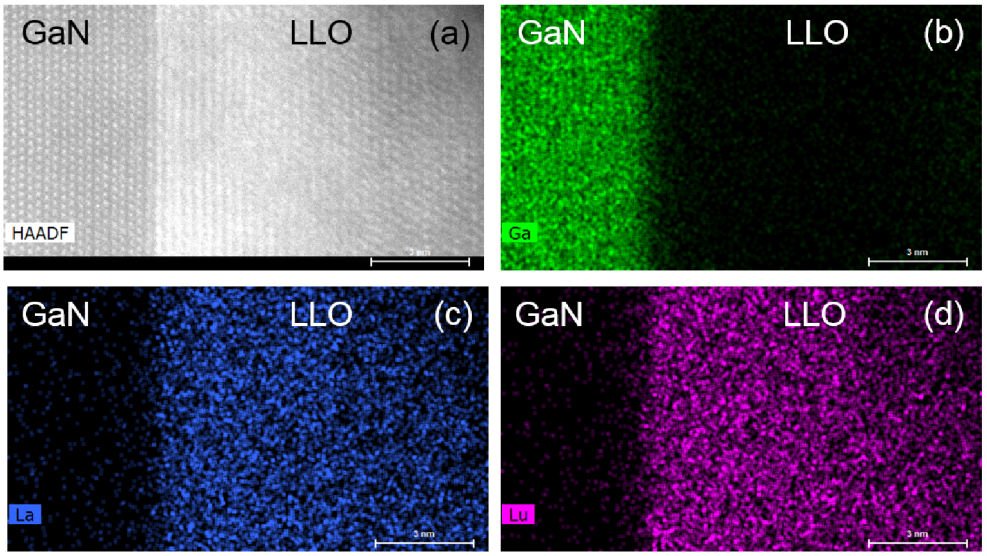

Figure 3.38: (a) HAADF image of the investigated area of hexagonal LLO on GaN. EDX map of Ga (b), La (c) and Lu (d). To the right side the lamella gets thinner, which is shown by the darker contrast in the HAADF image and the lower EDX intensities.

From the measured EDX maps a linescan perpendicular to the interface is calculated, which is displayed as an overlay in Figure 3.39. In the GaN the only measured element is Ga and the peaks in the EDX linescan correspond to the position of the Ga atom columns, that are visible in the HAADF image. The Ga intensity increases from 90% of the average intensity to 10 % within 1 nm, showing a sharp interface and no diffusion. The La and Lu intensity is negligible within the GaN. At the interface the La and the Lu intensity increase at the same position, but the intensity of the Lu is slightly larger than the one of La, so that small decomposition is possible. Closer to the edge the intensity of the La and the Lu decrease, due to

the reduced thickness of the lamella, also visible in the HAADF by a decrease in contrast.

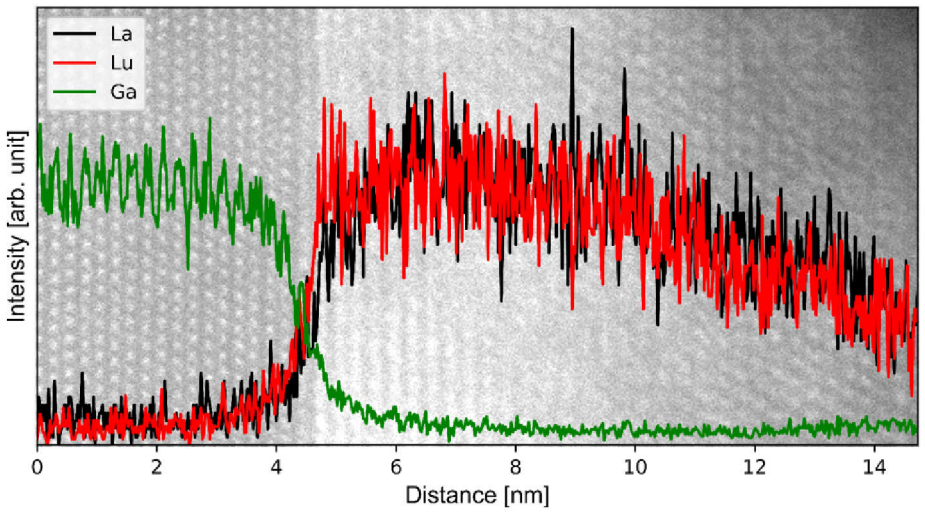

Figure 3.39: Linescan of hexagonal LLO showing the EDX intensity of La (black), Lu (red) and Ga (green) concentration. To the right side the LLO layer gets thinner, resulting in a weaker EDX signal.

3.2.3.4 Automated diffraction tomography

Automated diffraction tomography (ADT) (compare section 2.2.2) of the hexagonal LLO and GSO on GaN was applied to determine the crystal structure of the hexagonal GSO and hexagonal LLO in particular the space group and the atom position within the unit cell. The ADT characterization was done by Dr. Ute Kolb and Sergi Plana Ruiz from the Institut für Physikalische Chemie in Mainz. First results give a hint on the crystal structure. For the hexagonal LLO a lamella, prepared by focused ion beam (FIB), with 20 nm hexagonal LLO on GaN substrate is investigated by a manual nano beam diffraction (NBD). Diffraction patterns (DP) were recorded between -60° and 60° with a tilt step of 1° and a 5 nm electron beam. From the measured DP the reciprocal space is reconstructed and the found LLO unit cell is overlapped. In Figure 3.40 (a-c) the diffraction spots in the reconstructed reciprocal space are shown along the a*, b* and c* axis, respectively. The hexagonal unit cell of LLO, marked by yellow lines, is overlaid to the reciprocal space map. The reciprocal space vectors are plotted in the unit cell. The determined lattice parameters are

a=3.79 Å, b=3.87 Å and c=6.15 Å, and α=90.3°, β=89.1° and γ=119.9°, which fit to the previously reported lattice parameters by XRD [4]. In Figure 3.40 (d-f) cuts of the reciprocal space reconstruction are shown, which correspond to the (000l), ($h\bar{h}0l$), and the ($hh\bar{2}hl$) crystallographic planes, respectively. The diffraction spots along the axes are coloured red and the hexagonal unit cell of LLO is marked by yellow lines. From those images the symmetry is analysed. It can be seen that along the c*-axis there is a reflection condition given by l = 2n and the same rule is found for the ($hh\overline{2h}l$). Using the International Tables for Crystallography [52] the found symmetry fits to the extinction symbol P–c (a c-glide plane along the b-axis), so that possible space groups for the hexagonal phase are $P6_3mc$, P-62c and $P6_3|mmc$.

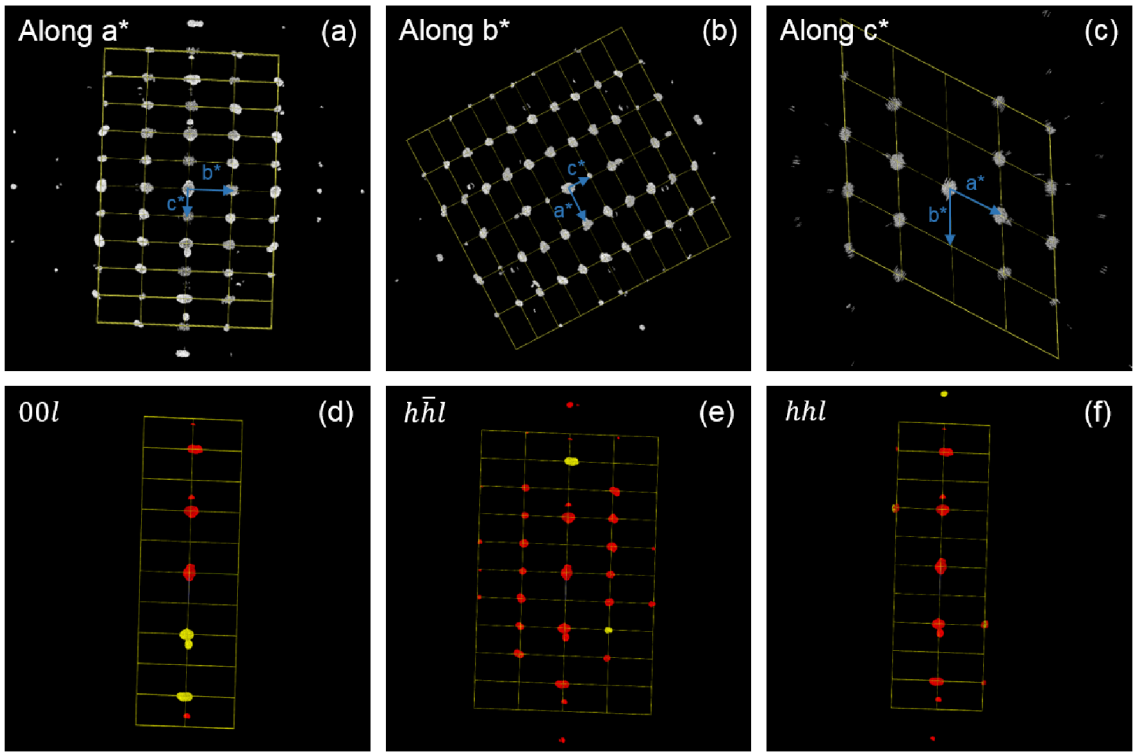

Figure 3.40: Projections of the reconstructed reciprocal space overlapped with the found LLO unit cell along a* (a), along b* (b) and along c* (c). Cuts from the reciprocal space reconstruction corresponding to the planes ($h\bar{h}0l$) (d), ($hh\overline{2h}l$) (e) and (000l) (f).

For the hexagonal GSO the same procedure is applied. The GSO lamella was cut out of a 20 nm thick hexagonal GSO layer on GaN. The reconstructed reciprocal space and the determined unit cell for hexagonal GSO is shown in Figure 3.41 (a-c)

along the a*, b* and c* axis, respectively. The determined lattice parameters for the hexagonal unit cell are a=3.65 Å, b=3.74 Å and c=5.89 Å, and α=90.9°, β=89.3° and γ=120.4°, which fits to the results from XRD as well (see section 3.2.3.3). In Figure 3.41 (d) a cut of the reconstructed reciprocal space is shown corresponding to the $(hh\bar{2}hl)$ plane. Due to the measurement geometry, it was not possible to acquire reflections related to the $(h\bar{h}0l)$, but other measurements (not shown here) confirm, that the hexagonal GSO exhibits the same symmetry as the hexagonal LLO. Therefore, the possible space groups are $P6_3mc$, P-62c and $P6_3|mmc$ for the hexagonal phase as well. Unfortunately, the measurement set did not allow for an unambiguous determination of the space group, since the data are too noisy. This may be attributed to the mosaic-structure of the films, where only small domains in the order of 20 nm exist. Most likely the measurements are not taken from a single domain. Hence, the measurements have to be repeated with a better lateral positioning of exactly the same specimen area into the electron while tilting the specimen.

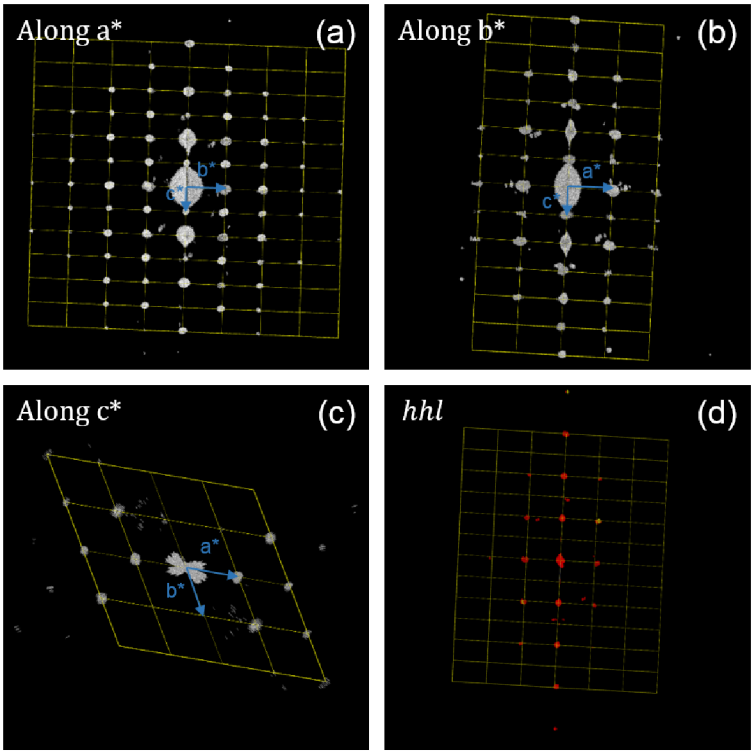

Figure 3.41: Projections of the reconstructed reciprocal space overlapped with the determined GSO unit cell along a* (a), along b* (b) and along c* (c). Cut from the reciprocal space reconstruction corresponding to the plane $(hh\overline{2}hl)$ (d).

3.2.4 Alternative growth substrates

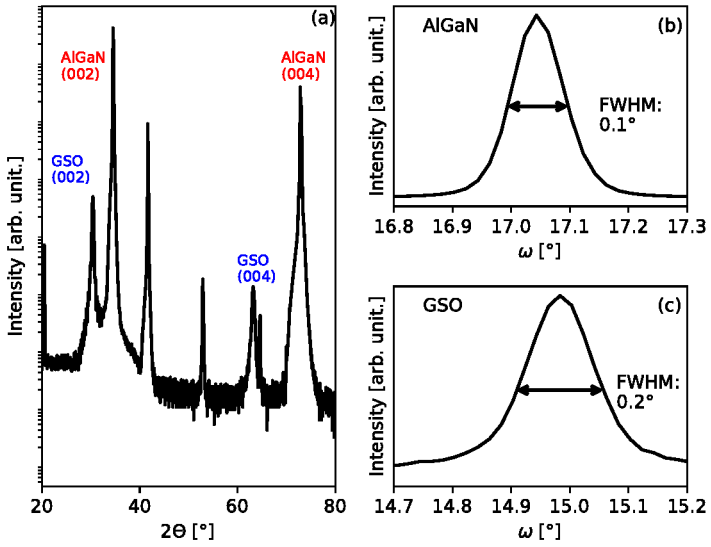

Figure 3.42: $\omega-2\Theta$ scan of the GSO layer on the AlGaN substrate in the out-of plane direction revealing the GSO and GaN (002) and (004) reflection (a). Rocking curve measurement of the AlGaN substrate with an FWHM of 0.1° (b) and of the GSO oxide with an FWHM of 0.2° (c).

Hexagonal $GdScO_3$ (GSO) and hexagonal $LaLuO_3$ (LLO) were grown on GaN by PLD and revealed good electrical properties in particular a large relative permittivity and a larger band gap. Besides GaN the ternary rare-earth oxides are deposited on InGaN and AlGaN. The AlGaN or InGaN layer is grown on GaN, so that a two dimensional electron gas (2DEG) in between the layers is formed (compare section 3.1.1.3), which can be used for heterostructure field-effect-transistors. By depositing an oxide on top of the AlGaN or the InGaN the substrate can be passivated to improve the function of the device. Therefore, hexagonal GSO and hexagonal LLO were deposited on AlGaN and the properties of the oxide layer was investigated by XRD. In Figure 3.42 (a) a out-of-plane $\omega - 2\Theta$ scan of a GSO layer deposited on AlGaN is shown. The intensity of the scattered X-ray measurement is plotted against the angle 2Θ. In the image six peaks are identified. The first two peaks are the (002) reflections and the last ones are the (004) reflections of GSO and AlGaN. The determined out-of-plane lattice parameter is 5.9 Å, fitting to the c-axis of hexagonal GSO. In between two additional peaks are visible, which result from the complex buffer structure underneath the AlGaN. In Figure 3.42 (b) a rocking

curve measurement of the AlGaN and in Figure 3.42 (c) a rocking curve measurement of the GSO is shown. For both the full width half maximum (FWHM) is determined. The FWHM of the AlGaN is 0.1°, which is comparable to the used GaN. The FWHM maximum of the GSO is 0.2°, which is slightly larger than the FWHM of GSO on GaN, but still offers a good crystal quality. Electrical characterization of the samples failed, because the sample were conductive from the beginning.

InGaN is another alternative growth substrate and offers also the possibility to use a 2DEG. Hexagonal LLO and GSO were deposited on InGaN. In Figure 3.43 (a) a $\omega - 2\Theta$ scan of hexagonal LLO on InGaN in the out-of plane direction is shown. The (002) and (004) reflections of LLO and InGaN are visible, beside another reflection of the underlying buffer layers. The out-of-plane lattice parameter is 6.1 Å, which matches to the c-axis of hexagonal LLO determined for hexagonal LLO on GaN. In Figure 3.43 (b) and (c) the rocking curve measurement of the (002) reflection of the InGaN and the LLO are shown, respectively. The InGaN reveals a FWHM of 0.26° and the LLO a FWHM of 0.5°. Thus, the crystal quality of the LLO is lower than that of the InGaN. The sample exhibits a large leakage current from the beginning, hindering any electrical characterization.

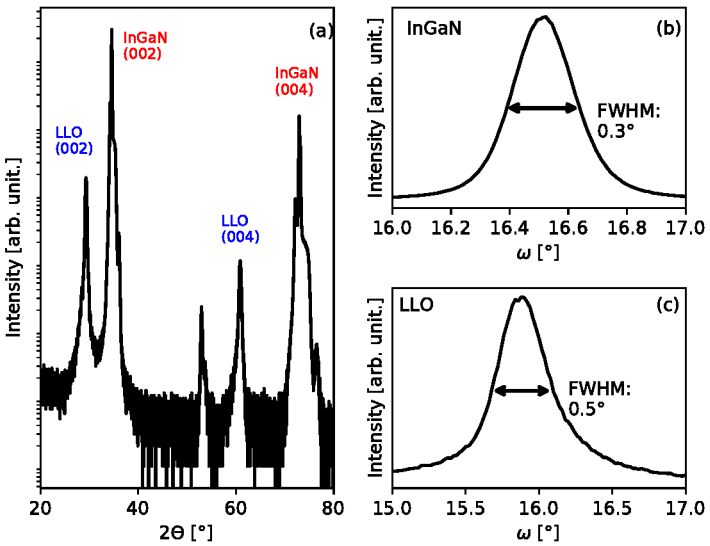

Figure 3.43: (a) $\omega - 2\Theta$ scan of the LLO layer on the InGaN substrate in the out-of plane direction revealing the LLO and GaN (002) and (004) reflection. Rocking curve measurement of the InGaN substrate with an FWHM of 0.3° (b) and of the LLO oxide with an FWHM of 0.5° (c).

Due to the failed electrical characterization of the samples, the reason for the large leakage currents was looked for. The bare substrates were investigated by scanning electron microscopy. The recorded images are shown in Figure 3.44 for NovaGaN (a), AlGaN (b) and InGaN (c). The NovaGaN reveals a smooth surface, with sporadic pinholes. The pinholes density is about $2/\mu m^2$. Pinholes are structural defects in the surface, which begin in the GaN and continue into the oxide layer. Pinholes can be reduced by optimizing the growth parameters of the GaN. On the AlGaN the surface shows $20/\mu m^2$ pinholes. The pinholes hinder a continuous growth of the oxide, because structural defects in the substrate continue in the grown oxide for epitaxial growth. Thus, during metallization a direct contact between the metal and the substrate is established. The GaN exhibits pinholes, too, but due to their lower density and the small size of the metal contacts, only occasionally leakage occurs. The InGaN in Figure 3.44 (c) reveals a lot of pinholes ($50/\mu m^2$), which seem to be aligned. The pinholes may be oriented along the grains boundaries of the grown InGaN grains. Here, the pinholes prevent electrical characterization, too. In conclusion growth of ternary rare-earth oxides in a good crystal quality on InGaN and AlGaN is possible, but structural defects in the substrate used, prevent electrical characterization.

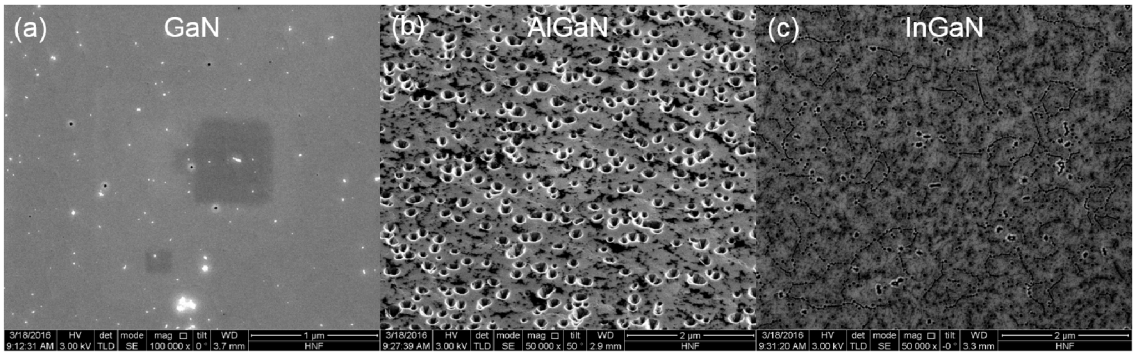

Figure 3.44: Scanning electron microscopy images of the surface of the GaN (a), AlGaN (b) and InGaN (c) substrates.

3.3 Discussion

The results shown in the previous sections are discussed in the following part beginning with the electrical properties, followed by the structural analysis. The ternary rare-earth oxides hexagonal GSO and LLO on GaN are recently found high-κ dielectrics, that are for the most part unexplored. So far the only electrical character-

ization reported, was on Si/Y_2O_3 buffer layers, because the GaN substrate revealed too many defects, causing leakage. [4] This problem was overcome by new GaN substrates, so that the GSO and LLO are electrically validated for the first time as high-κ gate dielectric on GaN for power electronic applications. According to the requirements for gate dielectrics (section 3.1.1) the determined relative permittivity (κ) and the band gap (<5 eV) of the amorphous and hexagonal GSO as well as hexagonal LLO make them suited for implementation into devices. The hexagonal GSO exhibits a larger permittivity than the amorphous phase, so that the hexagonal crystal structure increases the permittivity of the oxides. In the following the investigated GSO and LLO layers are compared to other rare-earth oxides, which are listed in table 3.3.

Table 3.3: Determined relative permittivity and band gap of amorphous and hexagonal GSO and hexagonal LLO on GaN. For comparison the properties of GSO and LLO grown on Si/Y_2O_3 and of the binary oxides Sc_2O_3, Gd_2O_3, La_2O_3 and Lu_2O_3 are listed, too.

Material	Crystal structure	Relative permittivity	band gap
$GdScO_3$ on GaN	hexagonal	30	4.2
$GdScO_3$ on GaN	amorphous	23	5.2
$LaLuO_3$ on GaN	hexagonal	32	5.7
$GdScO_3$ on Si/Y_2O_3	hexagonal	24 [4]	5.9 [4]
$GdScO_3$ on Si/Y_2O_3	cubic	14 [4]	5.2 [4]
$LaLuO_3$ on Si/Y_2O_3	hexagonal	26 [4]	5.8 [4]
$LaLuO_3$ on Si/Y_2O_3	cubic	23 [4]	6 [4]
$LaLuO_3$	orthorhombic	30 [43]	-
$GdScO_3$, $DyScO_3$, $LaScO_3$	amorphous	22 ± 3 [30]	5.7 ± 0.1 [53]
Lu_2O_3	cubic	30 [42]	-
Gd_2O_3	cubic [31]	12 [31]	6 [54]
Sc_2O_3	-	14 [54]	-
La_2O_3	-	23.5 [55]	6 [56]
Lu_2O_3	-	15 [57]	5.5 eV [58]

Due to Engström ternary rare-earth oxides can overcome the disadvantage of binary rare-earth oxides, i.e. either a low permittivity or a low band gap [1], which is true

for GSO and LLO, that exhibit a sufficient band gap and a larger permittivity than the binary oxides (12-30). In comparison to other reported electrical properties of ternary rare-earth oxides, the hexagonal GSO and LLO reveal improved properties. Zhao et al. investigated amorphous $GdScO_3$, $DyScO_3$ and $LaScO_3$ and reported a permittivity of 22 comparable to amorphous GSO measured in this thesis. Therefore, the hexagonal crystal structure seems to increase the permittivity of the oxides. The amorphous as well as the hexagonal GSO exhibit a larger permittivity than the GSO and LLO on Si/Y_2O_3, although the band gap is slightly reduced [4]. Liu et al. investigated cubic LLO on GaAs and determined a κ of 30 [42], which is also larger compared to the value reported by Schäfer [4]. Thus, the κ determined on the Si/Y_2O_3 is lower compared to GSO and LLO deposited on bare GaN.

Besides a sufficient large band gap, the band alignment of the oxide in relation to the substrate was investigated, revealing a staggered band alignment, so that the conduction band of the GSO and LLO is in the band gap of the GaN. Consequently, if a positive gate voltage is applied, the electrons face no potential barrier, so that a current flows already at low voltages. In contrast to a positive gate voltage, at a negative gate voltage a high barrier exists for holes and electrons, preventing any current up to a large applied gate voltage. [49] The staggered band alignment results in an asymmetric shape of the current voltage (IV) curve (compare Figure 3.15), which reveals larger currents at positive voltage than at negative voltage. Further, different IV characteristics are determined for amorphous GSO, hexagonal GSO and hexagonal LLO. Leakage is induced by electrical defects, that form leakage paths, so that a larger current indicates more defects [39]. The amorphous GSO reveals a lower current at negative bias in the region from 0 MV/cm to -10 MV/cm than the hexagonal ternary rare-earth oxides, indicating less electrical defects in amorphous than in hexagonal GSO. Due to the large bond length mismatch of hexagonal GSO with the GaN, more structural defects and subsequently electrical defects are generated than in amorphous GSO [39]. Consequently, the hexagonal LLO, which exhibits the largest lattice mismatch and thus the most structural defects, exhibits the largest current. Proof for the different concentrations of structural defects is given by X-ray photoelectron spectroscopy (XPS) measurements. A hydrogen contamination of the oxide layers is measured, which is absorbed at structural defects, so that a larger hydrogen amount implies more structural defects. The hydrogen concentration increases from amorphous GSO to hexagonal GSO to hexagonal LLO. Since amorphous GSO has no lattice mismatch, less structural defects are expected than for hexagonal GSO, and the lower lattice mismatch of hexagonal GSO than the one of hexagonal LLO produces less structural defects.
Apart from the band gap and the permittivity, electrical defects influence the performance of the gate dielectric. Due to the varying substrate quality (see Figure 3.10 and section 3.2.1) no quantitative analysis is possible, but a qualitative evaluation of the defects by the change of the CV characteristics. Capacitance-voltage (CV)

measurements of the deposited layers reveal a shift of the V_{fB} during measurement (compare section 3.2.1), indicating the existence of electrical defects. Due to the shift to positive voltage during the measurement (see Figure 3.11), the electrical defects are negative charges, that screen the applied gate voltage [1]. By applying a larger voltage a larger shift of the CV curve occurs. Most probably the traps are acceptor-type, that are neutral at the initial state, and are filled by electrons, when the bands are bended downwards by applying a positive voltage. Thus, the applied voltage is screened by the negative charges. A larger bending of the bands by a larger applied voltage, fills more traps deeper in the bandgap. [1, 59] Further, the electrical defects in the oxides are stable as can be seen in Figure 3.11 (b), since the hysteresis caused by the charges only occurs during the first cycle. Subsequent cycles exhibit a negligible hysteresis, so that the traps are not emptied by a negative applied voltage nor by time, i.e. after 64 h. The existence of electrical defects is also indicated by the large hydrogen concentration measured by XPS. The hydrogen is absorbed at structural defects, that also create electrical defects. Beside the shift of the CV curve the intersection of the linear fit to the capacitance equivalent thickness (CET) plots with the y-axis, varies for all the measured CET plots (see Figure 3.12). To calculate the CET the relative permittivity of SiO_2 (3.9) is used. In this way the interfacial layer thickness of a SiO_2 layer can be identified for an oxide deposited on Si. Although the relative permittivity of a native oxide or contamination of the GaN surface is not 3.9, the variation of the intersection of the linear fit with the y-axis indicates a existence of a varying interfacial layer. Various surface contaminations are possible. Despite the substrate cleaning a carbon contamination [60] of the GaN is possible and due to the high substrate temperature (~600 °C) the oxidization of the GaN is likely [38]. Further, by XPS a Cl contamination was measured (compare section 3.2.2), which results from the cleaning of the GaN by HCl [49]. Due to the rough interface and the substrate quality deviations on a 2 inch wafer, the contamination and oxidization on the GaN varies. Therefore, the intersection of each CET plot with the y-axis and in order the formation of an interfacial layer depends on the chosen GaN substrate.

Taking the lattice constants measured by XRD, a large lattice mismatch of 13% and 18% for GSO and LLO, respectively, is detected, where the lattice mismatch (Δ) is defined as:

$$\Delta = \frac{a_L - a_S}{a_L} \text{ [28]}, \tag{3.9}$$

where a_L and a_S are the lattice parameters of the epitaxial layer and the substrate, respectively. As a consequence the critical thickness t_c, up to which strained, epitaxial growth occurs, is given by the empirical formula

$$t_c = \frac{a_L}{2 \cdot \Delta} \text{ [28]}, \tag{3.10}$$

is as low as 1.5 nm for GSO and 1 nm for LLO. Since all investigated layer thicknesses investigated up to 150 nm always reveal the same hexagonal lattice constants, we have to assume that the layers are fully relaxed.
The existence of the hexagonal phase of GSO and LLO has already been shown by Schäfer [4], but the formation mechanism of the hexagonal phase is yet unknown. The hexagonal GSO and LLO reveal a lattice mismatch of 13% and 18% for GSO and LLO with respect to the GaN, respectively and is not stable regarding to ab-initio calculations. In this thesis, the formation of the hexagonal phase is investigated, especially the interface, at which the epitaxial growth of the layers begins.
X-ray diffraction (XRD) measurements (see Figure 3.19 and Figure 3.29) proof the growth of the hexagonal phase of GSO, SSO and LLO, with the c-axis perpendicular to the interface. Reciprocal space map measurements revealed a fibre texture of the grown epitaxial layers with the c-axis as fibre axis perpendicular to the interface. In this way a possible relaxation mechanism is offered to match the oxide layer atoms locally to the GaN atoms. The in-plane tilt of the oxide layers is determined by reciprocal space maps, revealing an average grain tilt of 0.17° and 0.12° for LLO and GSO, respectively. In other words adjacent grains are only tilted by a small angle against each other. This explains, why electron diffraction patterns, such as the one shown in Figure 3.7 (b) do not show an obvious sign of rotated grains. The space group of the hexagonal phase can not be determined by XRD measurements, so that the assumed space group for the ab-initio calculations were guessed. Automated diffraction tomography measurements were performed, to narrow down the possible space groups. The investigations revealed the space group is P–c, so that the space groups $P6_3mc$, P-62c or $P6_3|mmc$ are the only possible space groups for the hexagonal phase. Aldebert et al. investigated the space groups of different crystal structures of La_2O_3 and determined, that hexagonal La_2O_3 exhibits the space group 194 ($P6_3|mmc$) [61]. Thus, this space group is most probably the one, hexagonal GSO and LLO exhibit.
Besides the structural analysis of the whole oxide, the interface is important for the epitaxial growth. The epitaxial growth and the formation of the hexagonal phase despite the large lattice mismatch and consequently the large tension at the interface, is attributed to the interface properties. For this reason the interface was investigated by TEM and STEM with EDX. The determined structural defects are shown in Figure 3.45. All investigated ternary rare-earth oxides revealed a region of blurry contrast at the interface. In the oxide away from the interface individual atom columns are distinguished. At scattered places at the interface the oxides revealed atom columns, that were oriented in relation to the GaN atoms. The blurry contrast in between those places indicates a change in orientation, which results from tilted domains. Due to the tilt of the domains, the atoms of the oxide can be matched to the GaN atoms and absorb the tension in between the oxide and the substrate, induced by the large lattice mismatch. The region of blurry contrast was widest for the LLO layer, which is related to the largest lattice mismatch.

Another structural defect, that may reduce the stress in between the oxide layer and the substrate, was a decomposition of the oxide. Hexagonal GSO exhibits a decomposition of Sc and Gd at the interface, whereby twice as much Sc as Gd is present in the first atomic plane at the interface. As in hexagonal GSO the amorphous GSO does not show any decomposition, so that the formation of a Sc rich interface layer is special for the hexagonal phase. Since the atom radius of Sc (160 pm) is smaller as the one of Gd (188 pm), a hexagonal Sc_2O_3 would reveal a shorter a-axis than the GSO. Jur et al. deposited hexagonal Sc_2O_3 on GaN by metal-organic chemical vapor deposition and determined the length of the a-axis to be 3.42 Å, which is a reduction of the axis of 5% compared to hexagonal GSO. The calculated lattice mismatch of hexagonal Sc_2O_3 to GaN is 7.2%, which is lower compared to the lattice mismatch of GSO (13%). [38] Although the first atom row at the interface exhibits Gd, so that the phase at the interface is not pure hexagonal Sc_2O_3, the higher Sc content reduces the lattice mismatch at the interface. The residual Gd, that is segregated at the interface, is distributed over the three next atom rows. In this way the enlargement of the a-axis due to the larger Gd content is reduced. In comparison SSO reveals a strong decomposition of the Sc and the Sm in places, while at other places only a slight decomposition was determined. In the LLO only a slight decomposition with a larger Lu content at the interface was measured (see Figure 3.39). In both cases the decomposition of the oxides results in first atom row with a reduced a-axis because of the smaller atom radius of Lu (175 pm) to La (195 pm) and Sc (160 pm) to Sm (185 pm). A smaller atom radius of the oxide atoms and a larger difference in atom radius seem to make the decomposition energetically favourable.
Since the PLD targets are stoichiometric, the decomposition of the oxides occurs during the growth of the oxide layer on the substrate. Most probably the oxide forms an homogeneous layer up to a critical layer thickness, at which the decomposition of the oxide happens to reduce the tension.
While all of the investigated hexagonal ternary rare-earth oxides reveal a blurry contrast and a decomposition at the interface, the hexagonal rare-earth scandates GSO and SSO exhibit another structural defect. GSO and SSO reveal an enhanced distance of the atom rows at the interface, which is larger than the distance of the atom rows in GaN and GSO or SSO. A possible explanation is a N-terminated GaN and a O-terminated oxide layer. The bonding of the substrate and the oxide by a N- and O-terminated layer is unlikely, since O as well as N are anions. If either the Ga would be N-terminated or the oxide layer O-terminated, the atom row distance at the interface would not be larger than the one of GSO. Most probably the enhanced distance results from a weak bonding of the oxide layer and the substrate. The enhanced distance and consequently the weaker connection between the GaN and the GSO supports the tilting of the grains and reduces the stress due to the lattice mismatch.

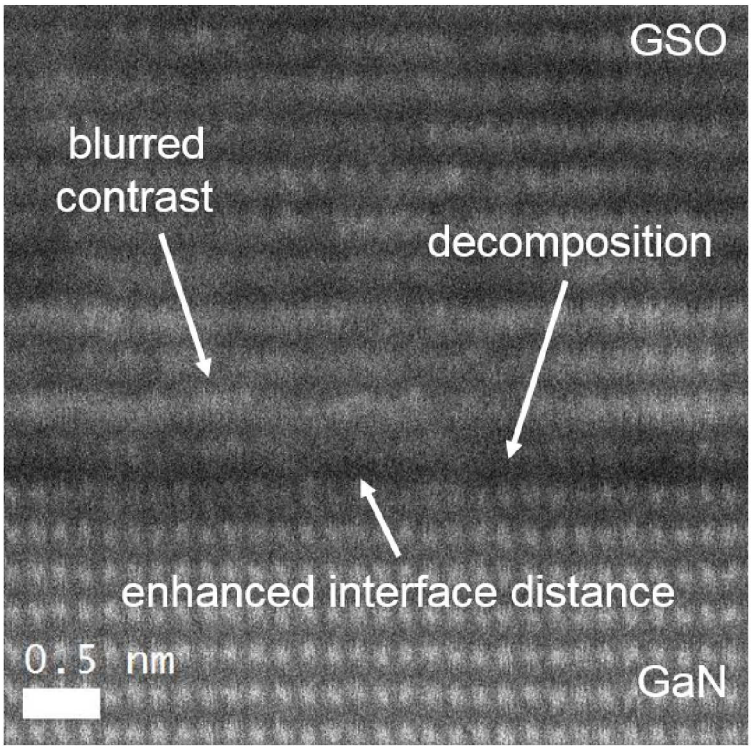

Figure 3.45: HAADF image of hexagonal GSO on GaN showing the structural defects at the interface. The decomposition at the interface is distinguishable due to the darker contrast at the interface.

Since the hexagonal LLO does not reveal any enhanced distance for stress reduction, the stress is absorbed by the tilted domains at the interface, causing a wider blurry contrast at the interface than the one of hexagonal GSO and SSO. Besides the determined structural defects Schäfer suggested, that the atoms of the rare-earth oxide do not match to the atoms of GaN, but every fifth or sixth atom of the oxide is located over an atom of the GaN. In this way the lattice mismatch can be reduced below 2%. [4] This assumption was not validated by this work, but can be another relaxation mechanism.

3.4 Summary

In conclusion, the ternary rare-earth oxides GSO and LLO were electrical characterised to attest the suitability of the layers as gate dielectric and the structural mechanism for the stabilization of the hexagonal phase was investigated.

The electrical characterization of the oxide layer revealed a large permittivity (23-32) and a band gap about 5 eV, making them suitable candidates for future gate dielectrics. The investigated hexagonal ternary rare-earth oxides exhibit improved properties in comparison to the amorphous phase, the binary oxides and other ternary rare-earth oxides. Acceptor-type defects and a possible interface contamination influence the electrical properties of the investigated samples. The GSO and the LLO reveal a staggered band alignment to the GaN, causing asymmetric IV characteristics.
The structural investigation of the layers revealed a fibre texture of the grown layers, whereby the grains are tilted by 0.12° to 0.17°. Especially the interface is important for the epitaxial growth and the stabilization of the hexagonal phase, despite the large lattice mismatch of the oxide and the substrate and consequently the large stress at the interface. The investigated hexagonal oxides reveal tilted domains resulting in a blurry contrast at the interface. Further, a decomposition of the ternary oxides occurs at the interface. Additionally, the GSO and the SSO exhibit an enhanced interface distance, that reduces the stress. The determined structural defects favour and contribute to the explanation of the stabilization and formation of the hexagonal phase. The space group of the hexagonal phase is narrowed down to the space groups $P6_3mc$, P-62c and $P6_3|mmc$ by automated diffraction tomography, whereby the space group 194 ($P6_3|mmc$) is most probably.

4 Ferroelectrics

Ferroelectric HfO_2 (HfO) wth 5% Gd (HfGdO), with 5% Lu (HfLuO) and with 3% Y (HfYO) was investigated with regard to the electrical and structural properties to evaluate their suitability for negative field effect transistors. Therefore, polarisation voltage and capacitance voltage measurements are performed, and transmission electron microscopy (TEM) images and X-ray diffraction (XRD) especially grazing incidence X-ray diffraction (GIXRD) scans were recorded. Parts of this work have already been published [62].

4.1 Introduction

4.1.1 Ferroelectric

Ferroelectrics exhibit in contrast to dielectrics and paraelectrics a spontaneous polarisation in the absence of an electric field, induced by the shift of positive and negative charges in the crystal. Ferroelectric crystals require one polar axis meaning that both ends of the axis are not equivalent. A typical ferroelectric material is $BaTiO_3$, where the Ti^{4+} ion is shifted by the electric field against the negative O^{2-} (see Figure 4.1 (a)). The polar axis is the c-axis along which the Ti ion is shifted. Ferroelectrics typically form domains, which show differently orientated polarisation. At the initial state all the domains are randomly distributed exhibiting no net polarisation (see Figure 4.1 (b)). By applying a positive electric field (E) the domains are orientated parallel resulting in the maximum spontaneous polarisation (P_s). If the electric field is turned off, the domains partially relax and the polarisation decreases to the remanent polarisation (P_r), which is stable without any applied electric field. If a negative electric field is applied the domains are switched to the opposite spontaneous polarisation. At a certain electric field the net polarisation is extinguished. This electric field is called coercive field strength (E_c). In theory ferroelectrics exhibit a hysteresis with a specific electric field, at which all domains switch at once. Due to electrical defects the domains switch successively. [27]

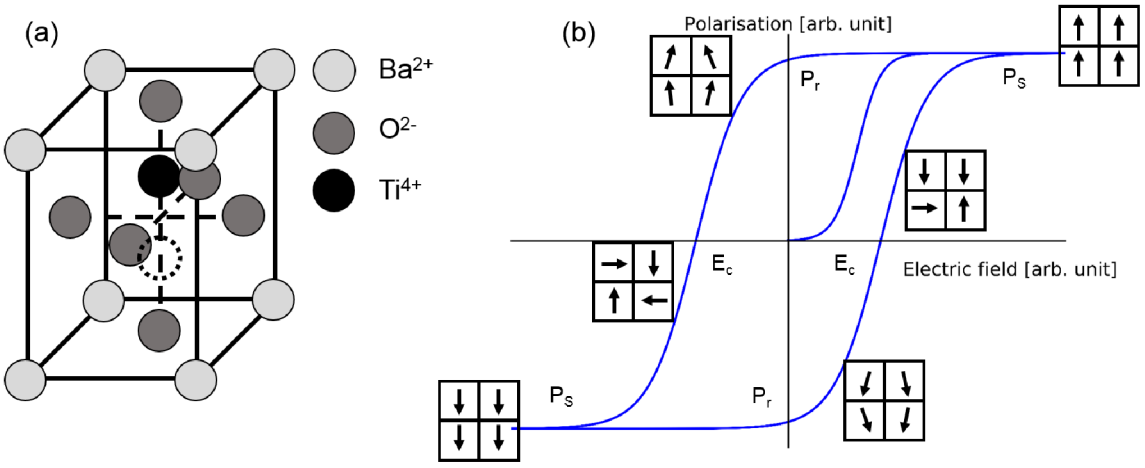

Figure 4.1: (a) Crystal structure of $BaTiO_3$ showing the two different positions of the Ti ion for different polarisation states. (b) Hysteresis of a ferroelectric from the initial state and sketches of the domain structure in the ferroelectric. The coercive field strength (E_c), the spontaneous polarisation (P_S) and the remanent polarisation (P_r) are marked in the hysteresis.

The domains in a ferroelectric are formed to reduce the free energy. If the ferroelectric would be totally polarized in one direction, a strong electrical stray field would be present causing a huge field energy. Therefore domains with opposite polarisation are combined, so that the net polarisation is minimized. The driving force is the reduction of the electric stray field, which is limited by the energy to build up domain walls. The form and size of the domains depends on the ferroelectric sample and the crystal structure. The domain structure is changed by applying an electric field. In contrast to ferromagnetics with domain walls of 10 nm and more, ferroelectric domain walls are only a few atomic layers thick. Beside ferroelectrics also antiferroelectrics exist, which exhibit ordered domains with the same strength of polarisation but opposite orientation. Thus, no overall net polarisation exists. Polarisation in ferroelectrics is influenced by pressure along the polar axis, too. Due to compresive stress or the tensile stress the distance of the negative and the positive charges is decreased or increased, respectively. An enhanced distance of the negative and positive charges, increases the polarisation, while a reduced distance, minimizes the polarisation. The relation between mechanical stress and polarisation is called piezoelectric. [27] Electrical defects in the ferroelectric layer or the top or bottom electrode may cause domain pinning. The electrical defects pin the domain

walls, so that they do not switch at an applied electric field. Two possible mechanisms affect the domain wall pinning. The first effect is the compensation of domain wall charges by charged electrical defects and the second effect is an alignment of electrical defect-dipoles to the local polarisation of the ferroelectric. [63]

4.1.1.1 Landau-Ginzburg-Devonshire theory

The phenomenological theory of ferroelectricity was developed by Ginzburg and Devonshire based on the Landau theory. The Landau-Ginzburg-Devonshire (LGD) theory describes the free energy of a ferroelectric by the order parameter polarisation in dependence of the temperature, because above a ferroelectric transition temperature (T_C) the polarisation disappears. Thus, the ferroelectricity and the phase change from dielectric to ferroelectric is described by the free energy density (G) by the order parameter polarisation (P) for an isothermal and isochoric estimation. Due to the symmetric shape of the free energy density only even exponents are allowed in the polynomial expansion [27, 64]:

$$G = F - EP = F_0 + \frac{\alpha}{2}P^2 + \frac{\beta}{4}P^4 + \frac{\gamma}{2}P^6 - EP \text{ [64]}, \tag{4.1}$$

where F_0 is the free energy density of the paraelectric phase and the expansion coefficients α, β and γ are pressure and temperature dependent. The minima of the polynomial expansion are related to the equilibrium conditions. [27, 64]

$$\frac{\delta F}{\delta P} = 0 \; and \; \frac{\delta^2 F}{\delta P^2} > 0. \text{ [64]} \tag{4.2}$$

Two types of transition are distinguished: First-order transition of ferroelectrics like $BaTiO_3$ exhibit a sudden disappearance of the polarisation at T_C, while second-order transition for materials like triglycine sulfat reveal a continuous reduction of polarisation with increasing temperature (T). For the second order transition the coefficient are $\alpha = \frac{T-T_0}{\epsilon_0 C}$, $\beta < 0$ and $\gamma = 0$, where T_0 is a temperature constant, C is the Curie-Weiss constant and ϵ_0 is the vacuum permittivity. Applying the coefficient of the second-order transition and the equilibrium conditions (equation 4.2) into the free energy expansion (equation 4.1), two solutions are obtained. P is either $P = 0$ or $P = \pm\sqrt{\frac{1}{\beta \cdot C \cdot \epsilon_0}(T_0 - T)}$. Since β, C and ϵ_0 are all positive the only real solution for $T > T_0$ is $P = 0$. Because above T_0 the ferroelectric becomes paraelectric, so that T_0 is T_C. The polarisation approaches continuously against 0 for $T \to T_C$, so that this is a second order transition. The free energy expansion of the ferroelectric under, at and above T_C and the polarisation depending on the temperature for a second-order transition are shown in Figure 4.2. [27, 64]

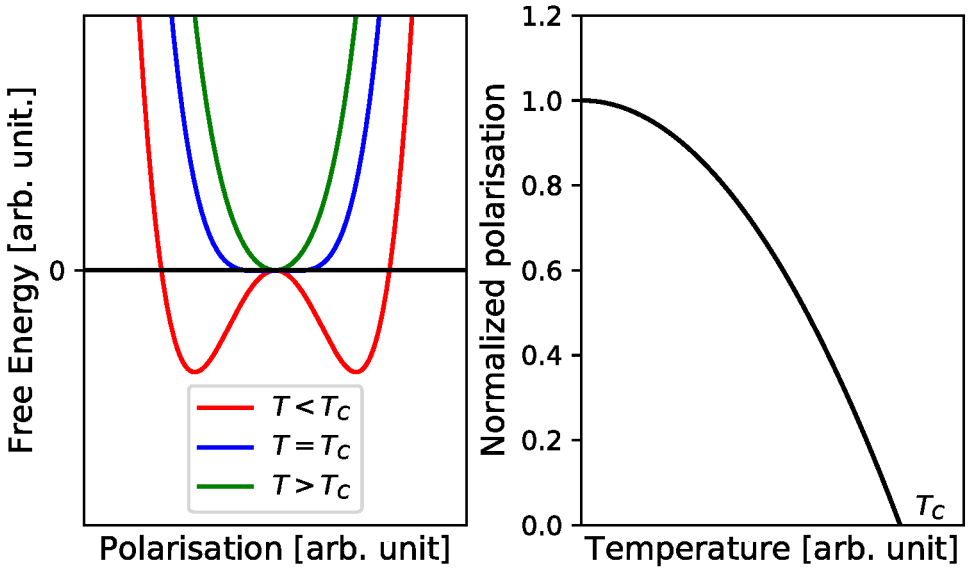

Figure 4.2: Following the second-order transition of the Landau-Ginzburg-Devonshire theory: (a) Sketch of the free energy vs. polarisation for $T > T_C$ (green curve), $T = T_C$ (blue curve) and $T < T_C$ (red curve). (b) Polarisation plotted vs temperature.

For the first-order transition β in equation 4.1 becomes negative, so that γ is important to prevent $G \to -\infty$ for huge P. Applying the coefficient of the first-order transition and the equilibrium conditions (equation 4.2) into the free energy expansion (equation 4.1), two solutions are obtained. [27, 64]

$$P = 0 \text{ and } \frac{1}{\epsilon_0 \cdot C} \cdot (T - T_0) \cdot P + \beta \cdot P^2 + \gamma \cdot P^4 = 0.[64] \tag{4.3}$$

Another condition is that at $T = T_C$ the free energy of the paralectric phase and the ferroelectric phase at zero polarisation (solution of 4.3) must be equal. The development of free energy density at different temperatures is shown in Figure 4.3 (a). At $T > T_C$ the global minima is at $P = 0$, while at $T = T_C$ there are minima at $P = 0$ and at finite P, and at $T < T_C$ two minima are at finite P. Thus, by cooling the system from $T > T_C$ the polarisation suddenly jumps from 0 to a finite value at $T = T_C$, indicating a first order transition as shown in Figure 4.3 (b). First order transitions are caused for example by phase changes of the material. [27, 64]

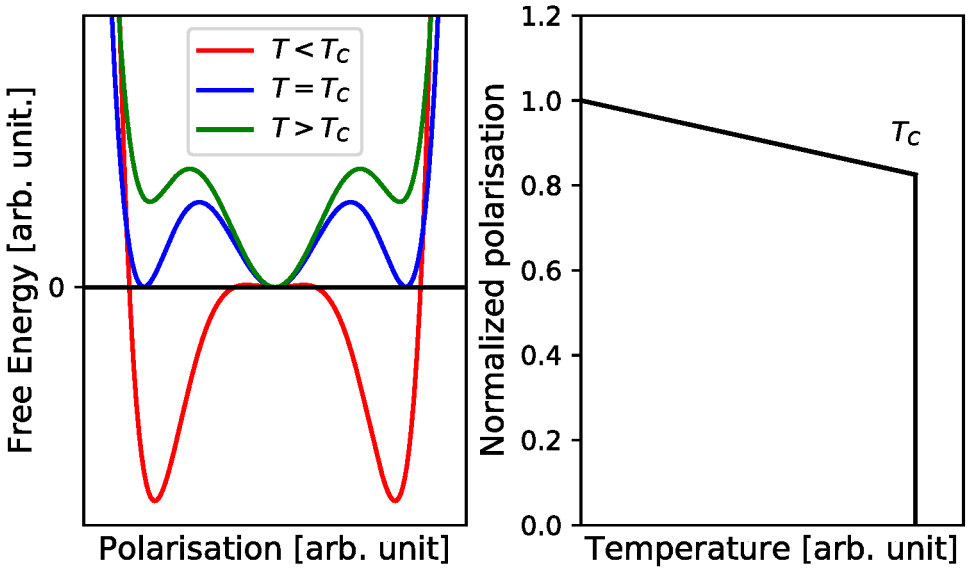

Figure 4.3: Following the first-order transition of the Landau-Ginzburg-Devonshire theory: (a) Sketch of the free energy vs. polarisation for $T > T_C$ (green curve), $T = T_C$ (blue curve) and $T < T_C$ (red curve). (b) Polarisation vs. temperature.

4.1.1.2 Ferroelectric HfO_2

Research on ferroelectric materials has mainly focused on perovskite structured materials, like $Pb(Zr, Ti)O_3$ or $BaTiO_3$, which exhibit many disadvantages concerning the intergration into CMOS technology [65]. Most ferroelectric perovskites exhibit a small bandgap between 3-4 eV resulting in a Schottky barrier height of about 1 eV [66]. Thus, a large layer thickness is required (~100 nm) to prevent leakage [67]. In addition, the growth of the perovskites on Si is difficult and results in a poor quality interface [68]. Therefore, the ferroelectrics are deposited in between metal top and bottom electrodes, which are connected to Si by a metal, making it difficult to achieve satisfactory interfaces [65, 69]. Further, the use of Pb in some perovskites is forbidden due to its toxicity [70]. Those disadvantages can be overcome by HfO_2 (HfO), which is usually employed as high-κ gate oxide [71, 72]. HfO is in comparison to the perovskite a simple binary oxide with a permittivity of 17 and a E_G of 5.3 - 5.7 eV in its monoclinic structure [73]. Depending on the temperature HfO exhibits various polymorphs at atmoshperic pressure. Up to a temperature of

1973 K HfO is monoclinic (space group $P2_1/c$), above this temperature it is tetragonal (space group $P4_2/nm$), until it switches to the cubic phase (space group Fm3m) at 2773 K. [74] In recent years, ferroelectric properties of polycrystalline HfO layer with various for example various concentrations of Gd[75], Sr[76], Lu [62], Y [77], Si [78] and Zr [79] have been discovered. In table 4.1 various added elements and the ferroelectric properties are shown.

Table 4.1: Added elements of HfO_2 and the theoretical and experimental remanent polarisation (P_r) and coercive field strength (E_c). [80]

Element	Theoretical P_r [$\mu C/cm^2$]	Experimental P_r [$\mu C/cm^2$]	E_c [MV/cm]
Si	41	24	0.8-1
Al	48	16	1.3
Gd	53	12	1.75
La	N/A	45	1.2
Y	40	24	1.2-1.5

The origin of the ferroelectric HfO is explained by an intermediate metastable orthorhombic phase (space group $Pbc2_1$), which is stabilized by various added elements [81]. The polar axis of the orthorhombic phase is along the c-axis [82]. Various deposition techniques are used for the ferroelectric HfO deposition like ALD [83], PLD [62] and chemical solution deposition [84]. A theoretical P_r of 40-50 $\mu C/cm^2$ was calculated, while the experimental determined P_r is about 12-24 $\mu C/cm^2$ besides HfO with La with a P_r of 45 $\mu C/cm^2$ [80]. Schroeder et al. investigated the influence of Si concentration on the ferroelectric properties. Besides the ferroelectric phase, they measured a pinched hysteresis for a Si concentration of 5.6 mol %, which could result from an antiferroelectric phase or domain wall pinning. An antiferroelectric phase is more likely, because the pinched hysteresis remained stable even after 10^7 cycles. [8] Ab-initio calculations by Reyes-Lillo et al. suggest the tetragonal phase of HfO is the antiferroelectric phase [85]. Böscke et al. investigated the influence of a top electrode (capping) layer during the anneal on the ferroelectric properties. They reported, that a capping layer increases the orthorhombic phase and therefore the ferroelectric properties. For the formation of the orthorhombic phase, an in-plane compressive pressure is necessary. The top capping layer prevents a volume expansion, which increases the compressive pressure and favours the formation of the orthorhombic phase. [86] Starschich et al. [84] investigated the wake-up effect of HfO with Y, describing the increasing polarisation during cycling. During cycling oxygen vacancies are created and redistributed, forming the orthorhombic phase and unpinning pinned domains, in this way increasing the polarisation. If a critical amount of oxygen vacanices is created, they form a leakage path, causing failure of

the device. [84] Ferroelectric HfO can be grown with a thickness of about 10 nm, which is crucial for three-dimensional capacitor fabrication [80] and an advantage over perovskite ferroelectric layers [65]. Consequently, the first ferroelectric field-effect transistors (FeFETs) based on ferroelectric HfO have been manufactured and scaled to the 28 nm technology node [87].

4.1.1.3 Negative capacitance field-effect-transistor

HfO is a commenly used high-κ oxide in CMOS technology, so that ferroelectric HfO can be easily integrated. Therefore HfO is a promising candidate for ferroelectric random access memory [88] or negative capacity field-effect-transitor (NCFET) to reduce the subthreshold slope (SS) [89, 10]. Common MOSFETs are limited to an SS of 60 mV/dec, which hinders further down scaling due to the generated heat by the large power consumption. An NCFET has the same structure as a metal-insultor-oxide field-effect-transitor (MOSFET compare section 3.1.1.2), besides an additional ferroelectric layer on the gate dielectric for the voltage amplification as shown in Figure 4.4 (a).

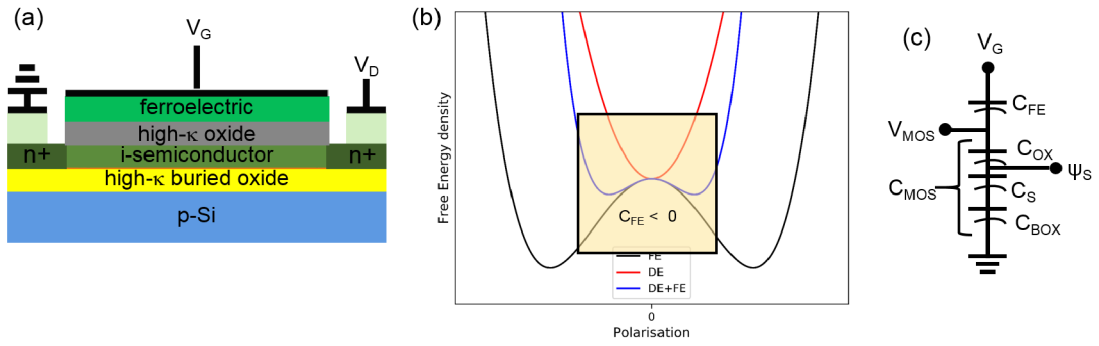

Figure 4.4: (a) Scheme of a NCFET. (b) Free energy over the polarisation of an dielectric and a ferroelectric and the region of negative capacitance. [90] (c) Simple capacitance model of an NCFET. [91]

The ferroelectric layer induces a voltage amplification on the applied gate voltage [91]. The free energy of a dielectric (green curve) and an ferroelectric (blue curve) over the polarisation is shown in Figure 4.4 (b). The free energy of the ferroelectric reveals two minima at finite polarisations, while the free energy of the dielectric has its minima at zero polarisation. The capacitance of the ferroelectric layer is the

second derivation of the free energy with respect to the polarisation $C = \frac{d^2F}{dP^2}^{-1}$. Hence, the ferroelectric exhibits a region around zero polarisation with a negative capacitance as displayed by the blue box in Figure 4.4 (b). The ferroelectric is unstable in this region, but in combination with a dielectric the minima of the free energy (purple curve) is stable in the region of negative capacitance. [90] A simple capacitance model for explanation of the negative capacity is shown in Figure 4.4 (c) [91].
The capacitance of an NCFET is a series combination of a ferroelectric capacitor (C_{Fe}) and the MOSFET capacitor (C_{MOS}), from which the amplification factor (A_V) can be derived by a simple capacitive divider for a negative C_{Fe}. [91]

$$A_V = \frac{\delta V_{MOS}}{\delta V_G} = \frac{|C_{Fe}|}{|C_{Fe}| - C_{MOS}} [91], \tag{4.4}$$

where δV_{MOS} is the change in the MOSFET channel and δV_G is the change in the gate voltage. A_V will be greater than 1 and thus a change in δV_G will induce a greater change in δV_{MOS}. The SS of the NCFET ($NCFET_{SS}$) can be calculated by dividing the SS of the MOSFET ($MOSFET_{SS}$) by the A_V. [91].

$$NCFET_{SS} = MOSFET_{SS} * \frac{1}{A_V} = \frac{60mV}{dec} * (1 + \frac{C_{dep}}{C_{Ox}}) * \frac{1}{A_V} [91], \tag{4.5}$$

where C_{Ox} is the capacitance of the oxide and C_{dep} is the capacitance of the depletion region. To determine the effect of the ferroelectric capacitor on the SS, A_V is substituted from equation 4.4 into equation 4.5 and C_{MOS} is expanded into C_{Ox} and C_{dep}. Then the $NCFET_{SS}$ is described by [91]:

$$NCFET_{SS} = \frac{60mV}{dec} * (1 + \frac{C_{dep}}{C_{Ox}} + \frac{C_{dep}}{|C_{Fe}|}) [91]. \tag{4.6}$$

If C_{Fe} is smaller than C_{Ox} the term in brackets becomes smaller than 1 and the SS of the NCFET is reduced below $\frac{60mV}{dec}$ [91]. Negative capacitance has already been measured on ferroelectrics [92, 93] and several groups have already shown NCFETs with SS down to 8.5 mV/dec [94, 95, 96]. Therefore, NCFETs are a promising device structure for the future.

4.1.2 Sample preparation

In this section the preparation of the ferroelectric metal-insulator-metal MIM and metal-oxide-semiconductor (MOS) stacks is described. The used techniques are explained in chapter 2. A scheme of the sample preparation is shown in Figure 4.5.

Ferroelectric HfO were grown on highly-doped Si or 40 nm TiN or TaN deposited on 200 mm Si wafers by sputtering and atomic layer deposition, respectively. The wafers were spin-coated with photoresist and cut into 20x20 mm^2 square pieces by a diamond saw. The resist was solved twice by acetone in a ultrasonic bath for five minutes and subsequently in isopropyl for three miuntes. The TiN and TaN was not further cleaned and the pure Si was RCA cleaned before oxide deposition following the approach of Kern et al. [24]. HfO_2 with 5% Gd (HfGdO) and HfO_2 with 5% Lu (HfLuO) were grown by pulsed laser deposition. The HfLuO and HfGdO stoichiometric targets were prepared by mixing 99.99 % HfO_2 and Lu_2O_3, HfO_2 and Gd_2O_3 powders in the desired amount, respectively. The mixed powders were grinded by ball milling with zirconia grinding balls and pressed into cylindrical greens 22 mm in diameter and 7 mm in height by cold isostatic pressing at 800 MPa. Before pressing, the powder mixture was granulated by adding a binder to enhance the fracture strength of the green bodies. The binder was burnt off before sintering by firing at 600 °C for 12 h in air. Sintering was performed at 1600 °C for 8 h in air. HfO_2 with 3% Y (HfYO) was deposited by ALD. After oxide deposition a 40 nm TiN layer is sputtered on top, followed by the deposition of 50 nm Pt by lithography and e-gun. Finally the layers were annealed up to 1000 °C and the TiN in between the Pt contacts was etched by reactive ion etching and Standard Clean 1. Some samples were investigated without a TiN top layer, for which the sputtering and the final etching was skipped.

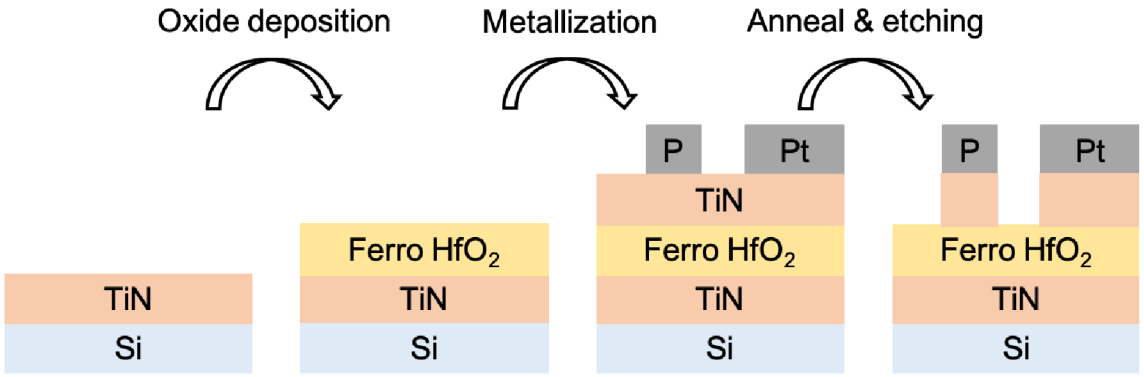

Figure 4.5: Scheme of the sample preparation MIM and MOS stacks with ferroelectric HfO_2.

4.2 Ferroelectric HfO_2 with 5% Gd

HfO with 5% Gd (HfGdO) is investigated to determine the influence of the process parameters on the electrical especially the ferroelectric properties. In Figure 4.6 (a) a polarisation voltage measurement of a 30 nm thick HfGdO sample with TiN bottom electrode and a TiN/ Pt top electrode is shown. The polarisation was normalized to the area of the measured pad and from the applied voltage the electric field (E) was calculated by dividing the applied voltage through the layer thickness. In Figure 4.6 (a) the polarisation electric field (PE) curve of HfGdO at different applied electric fields is shown. At an electric field of 1 MV/cm (black curve) no hysteresis is visible, since the applied electric field is smaller than the one, which is necessary to switch the domains.

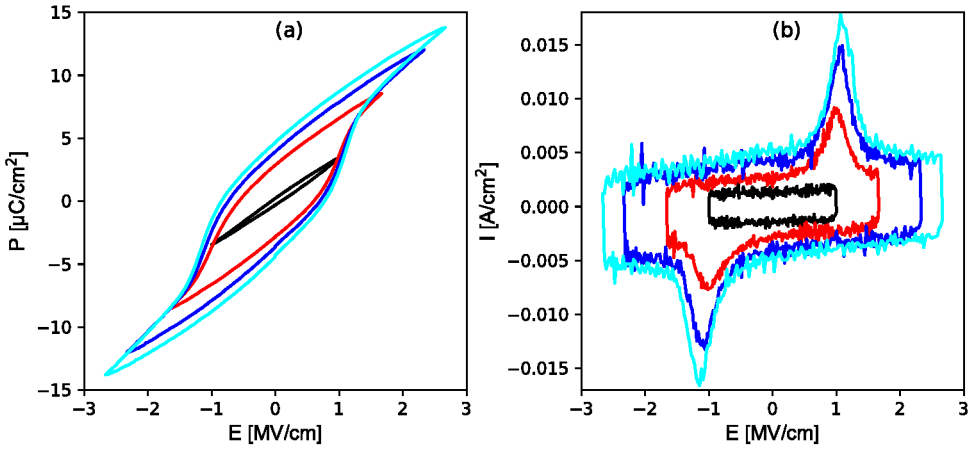

Figure 4.6: Influence of increasing electric field on the polarisation (a) and on the current (b) of 30 nm HfGdO on TiN bottom electrode with TiN/ Pt top electrode.

The corresponding current electric field (IE) curve is shown in Figure 4.6 (b) (black curve). Here, the electric field is calculated by dividing the applied voltage through the layer thickness and the current is normalized to the area of the measured pad. The current does not exhibit any change. By increasing the applied field up to 1.7 MV/cm (red curve) a small hysteresis occurs. Thus, the applied electric field is larger than the one to switch the polarisation of the ferroelectric layer. In the IE curve two distinguishable peaks are visible. By switching the domains, the polarisation of the ferroelectric layer is changed, which induces a measurable current.

Thus, the current increases during the switching and returns to the average, when all domains are switched. Further, increase of the electric field increases the polarisation of the ferroelectric, because more domains switch at a larger electric field. The remanent polarisation (P_r) is determined at zero electric field, because it is the polarisation that is stable, even without an applied electric field. Hence, a negative and a positive remanent polarisation exist, which are 4.7 µC/cm^2 and -4.3 µC/cm^2. Further, the coercive field strength (E_c) is determined. The coercive field strength is the applied electric field, at which the polarisation becomes zero. Thus, a positive and a negative coercive field strength are determined. The coercive field strength is 0.8 MV/cm and -0.8 MV/cm. The increased polarisation at higher electric fields is also visible in the IE curve by the increasing current as shown in Figure 4.6 (b). If more domains switch consequently the change in polarisation is larger, which induces a larger current. Therefore, at larger applied electric fields the current increases.

Another important property of the ferroelectric oxides is the change of the polarisation hysteresis and the current by cycling as shown in Figure 4.7. The sample is measured before and after the maximum positive and negative electric field is applied in turns for a 1000 times (cycling). Subsequently the polarisation electric field curve is measured again. This procedure is continued, till the sample exhibits failure.

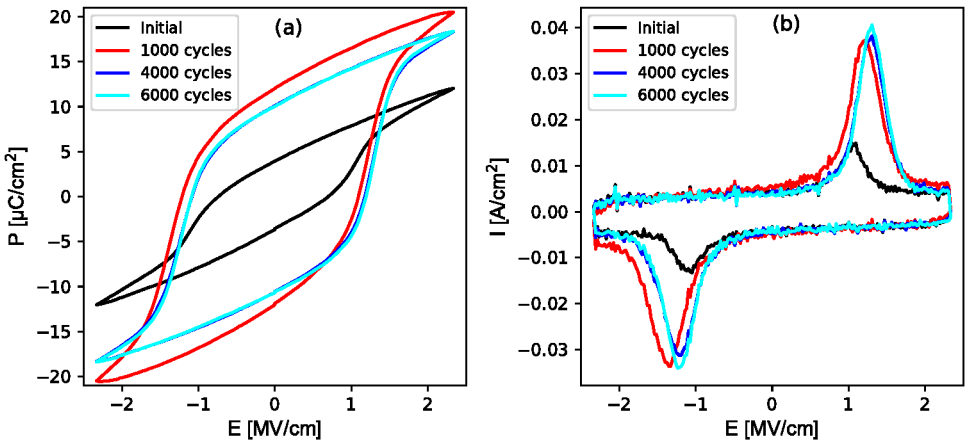

Figure 4.7: Influence of cycling on the PE (a) and IE (b) characteristics of a 30 nm HfGdO on TiN bottom electrode with TiN/ Pt top electrode.

The initial remanent polarisation (P_r) of a 30 nm HfGdO layer with TiN bottom and TiN/ Pt top electrode is 3.9 µC/cm^2 and -3.6 µC/cm^2 exhibiting a difference

of 0.3 µC/cm^2 between the positive and the negative P_r . After cycling the ferroelectric HfGdO for 10^3 times the hysteresis is steeper and the P_r is increased up to 12 µC/cm^2 and -11.9 µC/cm^2, so by cycling the difference in P_r is decreased. After $4{\cdot}10^3$ cycles the polarisation becomes smaller, so that the P_r is 10.1 µC/cm^2 and -10.5 µC/cm^2. Further, cycling up to $6{\cdot}10^3$ cycles does not change the polarisation curve. The IE curves of the sample are shown in Figure 4.7 (b). At the initial state the IE curve exhibits peaks with a maximum current of 0.015 A/cm^2. After 10^3 cycles the current increases up to 0.037 A/cm^2.

Capacitance voltage (CV) measurements of the ferroelectric layers are performed. From the measured CV curve the permittivity (κ) is calculated using the thickness of the HfGdO layer (d) measured by X-ray reflection by the equation

$$\kappa = \frac{\epsilon_0 \kappa A}{Cd}, \tag{4.7}$$

where ϵ_0 is the vacuum permittivity, A the area of the capacitor and C the capacity. The permittivity is plotted against the applied electric field, which is determined from the layer thickness and the applied voltage, as shown in Figure 4.8.

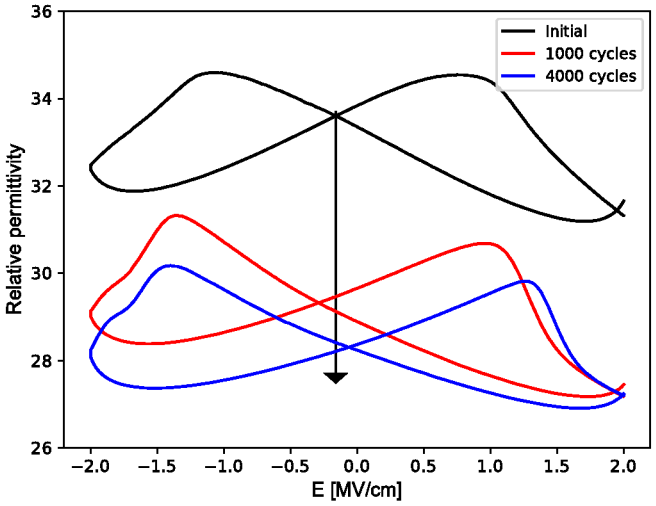

Figure 4.8: Influence of cycling on the relative permittivity of 30 nm HfGdO on TiN bottom electrode with TiN/ Pt top electrode.

The curve exhibits the characteristic "butterfly" shape. During the measurement the capacity is calculated from the change in the charge (Q) in relation to the voltage (V): $C = \frac{\delta Q}{\delta V}$. The switching of the domains induces a measurable charge and in

this way increases the measured capacitance. That way the butterfly shape arises. At the initial state the permittivity at the crossing point is about 33.6. By cycling the permittivity is reduced to 29.3 and 28.3 after 10^3 cycles and $4{\cdot}10^3$ cycles, respectively. Further, the position of the cross section corresponding to the electric field shifts.

The deposited HfGdO layers are amorphous and crystallize into the orthorhombic phase during a rapid thermal anneal revealed by XRD measurements (compare section 2.1.4). Thus, the annealing temperature is important for the ferroelectric properties. PE measurement of 30 nm HfGdO with a TiN bottom and TiN/Pt electrode annealed at 400 °C, 500 °C and 600 °C are shown in Figure 4.9. The remanent polarisation (P_r) is 5.5 µC/cm^2, 8.7 µC/cm^2 and 10.6 µC/cm^2 for an annealing temperature of 400 °C, 500 °C and 600 °C, respectively. The P_r is increasing with increasing annealing temperature (Figure 4.9 (a)). Temperatures above 600 °C cause leakage currents, so that the oxides are useless. The increasing polarisation is recognized in the current electric field (IE) curve (Figure 4.9 (b)), too. The current rise from 0.022 A/cm^2 up to 0.033 A/cm^2 for an annealing temperature of 400 °C and 600 °C, respectively.

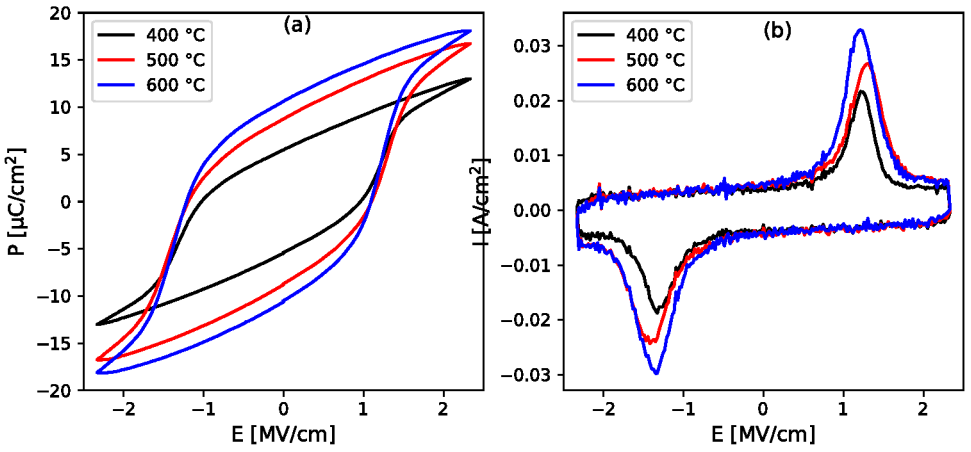

Figure 4.9: Influence of the annealing temperature on the polarisation (a) and the current (b) characteristics of 30 nm HfGdO on TiN bottom electrode with TiN/ Pt top electrode.

In order to determine the crystal structure of the HfGdO layer grazing incidence X-ray diffraction measurements are performed. The incident X-ray exhibits an angle of 2° with respect to the sample and the detector is scanning from 10° to 100° and

measures the intensity. In this way the effective path of the X-rays within the thin surface layer is enhanced and therefore the scattered intensity. In Figure 4.10 the GIXRD spectrum of the sample annealed at 600 °C (black curve) and 400 °C (red curve) is shown. The measured intensity is plotted against the detector angle (2Θ). In the GIXRD the reflections represent the different phases in the polycrystalline layer. The peak at 28° and 32° refer to the monoclinic phase, while the peak at 30.5° is the reflection of the orthorhombic or tetragonal phase, which can not be distinguished in GIXRD, due to their similar lattice parameters. The peak intensity of the monoclinic peaks at 28° and 32° are similar for both temperatures, but the intensity of the 30.5° tetragonal/ orthorhombic peak differs. Therefore, the oxide annealed at 400 °C exhibits less orthorhombic/ tetragonal phase than the sample annealed at 600 °C. Both peaks exhibit the same peak width, induced by the existence of residual amorphous phase. Since both peaks exhibit a comparable with, a difference in the amount of amorphous phase can be excluded. Further, a different ratio of tetragonal to orthorhombic phase of the sample annealed at 400 °C and at 600 °C is possible. Since the tetragonal phase is not ferroelectric, a higher ratio of tetragonal phase in the sample annealed at 400 °C could reduce the polarisation in comparison to the sample annealed at 600 °C.

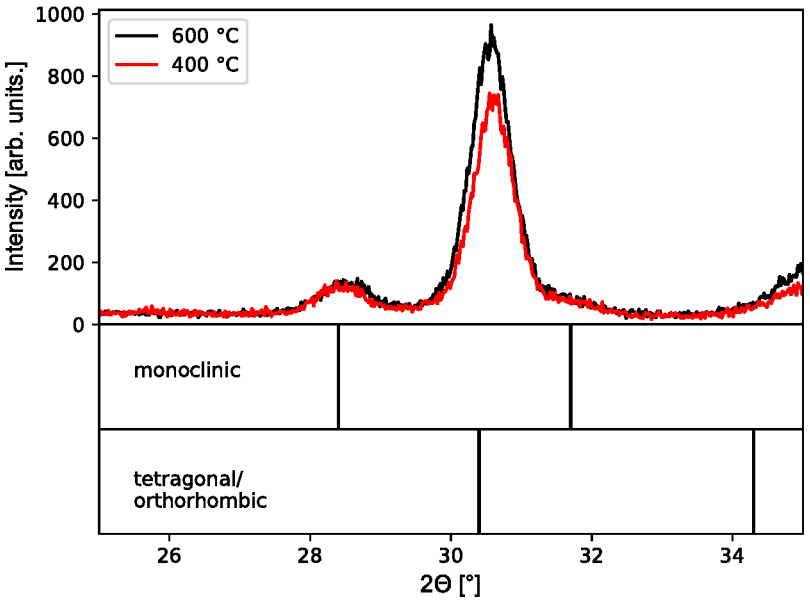

Figure 4.10: GIXRD of 30 nm HfGdO on TiN bottom electrode with TiN/ Pt top electrode annealed at 600 °C (black curve) and 400 °C (red curve).

The properties of the electrodes determine the properties of the ferroelectric layer. Therefore, different bottom and top electrodes are analysed as shown in Figure 4.11. In Figure 4.11 (a) the PE and IE measurement of the TiN/HfGdO/Pt stack is shown exhibiting a P_r of 4.5 µC/cm^2 and -4.4 µC/cm^2 and an E_c of 1 MV/cm and -1.1 MV/cm. Changing the bottom electrode to TaN (Figure 4.11 (c)) decreases the P_r to 3.5 µC/cm^2 and -3.6 MV/cm and the E_c is at 1.2 and -1.1 MV/cm. While the E_c of the TaN bottom electrode is comparable to the sample with TiN bottom electrode, the P_r is reduced about 1 µC/cm^2. Thus, the domains switch at the same electric field, but less domains switch, because less domains are present or the domains are pinned.

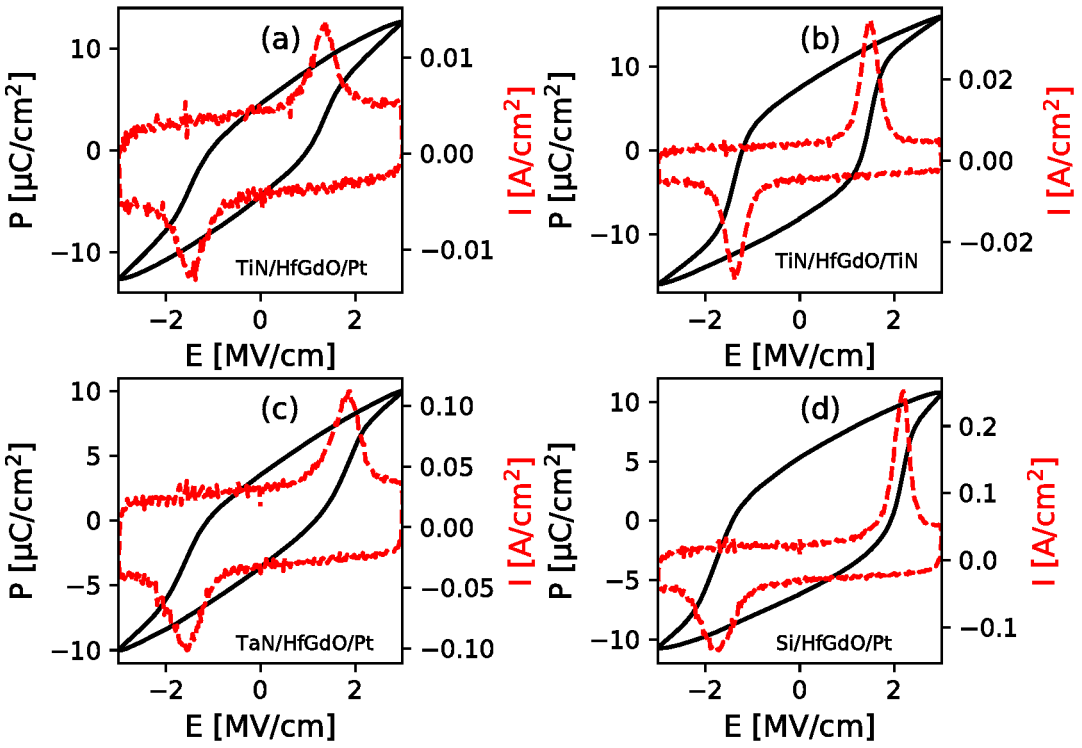

Figure 4.11: Influence of different top and bottom electrodes on the polarisation of the ferroelectric: (a) TiN/HfGdO/Pt, (b) TiN/HfGdO/TiN/Pt, (c) TaN/HfGdO/Pt, (d) Si/HfGdO/Pt.

Atomic force microscopy measurements exhibit a rougher surface of the TaN than the TiN. Thus, the electrode surface is significant for the ferroelectric layer. The

Si/HfGdO/Pt stack exhibits a P_r of 5.3 µC/cm^2 and -6.2 µC/cm^2 and an E_c of 1.9 MV/cm and -1.4 MV/cm. Thus, the hysteresis exhibits a difference in P_r of 1 µC/cm^2 and in E_c of 1 MV/cm. Further, the hysteresis is asymmetric, which is also visible in the IE curve (Figure 4.11 (d) red curve), showing a maximum positive current of 0.26 A/cm^2 and a maximum negative current of -0.13 A/cm^2. In Figure 4.11 (b) the hysteresis of the TiN/HfGdO/TiN stack is shown, revealing a P_r of 7.4 µC/cm^2 and -8.1 µC/cm^2 and an E_c of 1.3 MV/cm and -1.2 MV/cm. Thus, this stack exhibits the highest P_r , while the E_c is comparable to the other stacks. Further, the hysteresis of the stack is the steepest and the current (Figure 4.11 (b) red curve) is the largest with a maximum of 0.034 A/cm^2 and 0.029 A/cm^2. The metal-insulator-metal capacitor (MIMCap) with TiN bottom and top electrode is the best structure and is used for the further experiments.

4.3 Epitaxial HfO_2 with 5% Gd

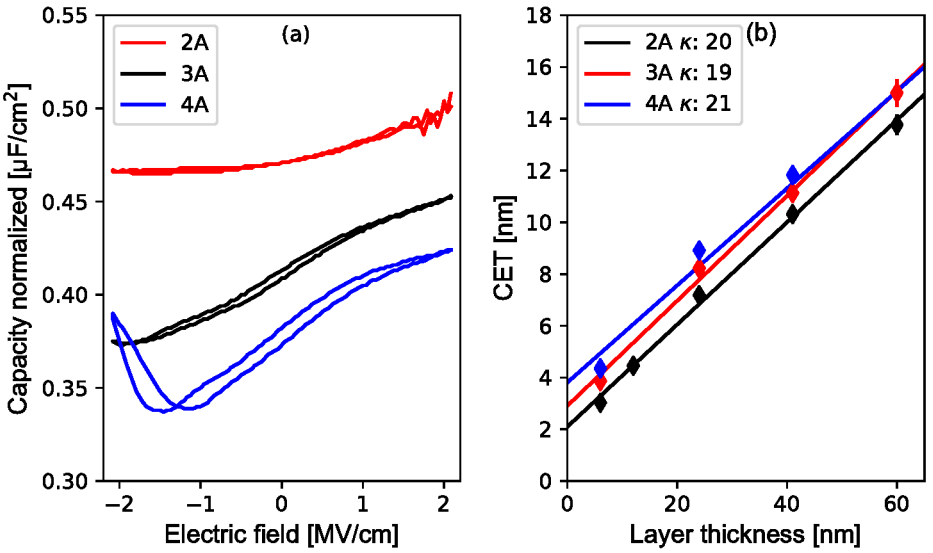

Figure 4.12: (a) Capacitance vs. electric field characteristics of a 24 nm thick HfGdO deposited on heated highly doped Si and (b) CET plots of epitaxial grown HfGdO at different substrate temperatures.

Ferroelectric HfO_2 (HfO) are usually polycrystalline and are placed in between a metal top and bottom electrode. Thus, the polycrystalline HfO exhibits an heterogeneous orientation of the crystal and hence of the polar axis. In this way, the

polarisation is reduced, since the crystals with an in-plane polar axis do not contribute to the polarisation. If the polar axis of all crystals would be perpendicular to the interface, the polarisation would be maximized. Further, a bottom and top electrode is required to maximize the amount of the orthorhombic phase in the layer (compare Figure 4.11). To overcome the disadvantages of a polycrystalline layer epitaxial layers could offer a single crystal or oriented polycrystal. Therefore, the HfGdO is deposited, while the highly n-doped Si substrate is heated by a current through the SiC heater of 2 A, 3 A or 4 A, resulting in a temperature of approximately 500 °C, 600 °C or 700 °C, respectively. By epitaxial growth a homogeneous crystal with a preferred orientation can be grown, generating less electrical defects and better polarisation. In Figure 4.12 (a) capacitance electric field measurements of 24 nm thick HfGdO layers deposited on highly doped Si are shown.

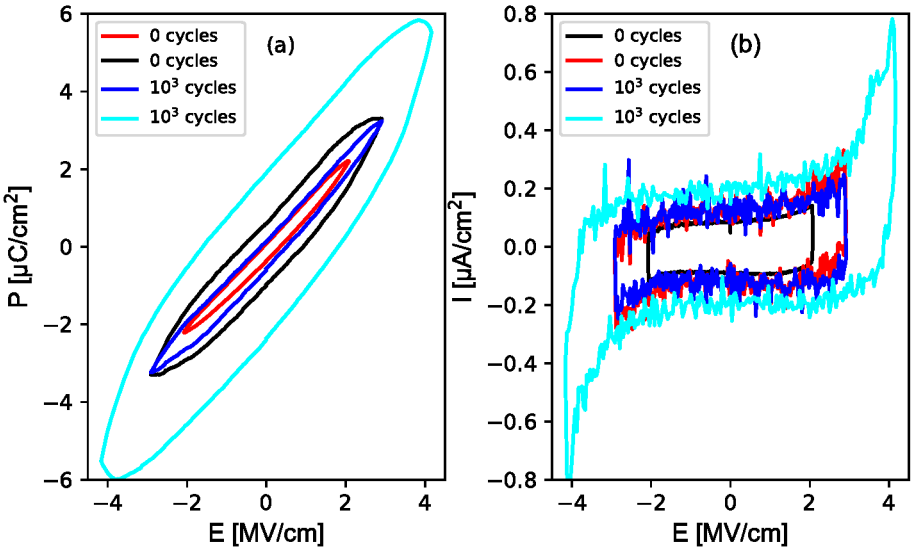

Figure 4.13: (a) PE measurement and (b) IE measurement of an epitaxial grown 24 nm thick HfGdO layer on Si deposited at ~600 °C.

Independent of the growth temperature the capacity does not exhibit the characteristic butterfly shape of ferroelectric materials (compare Figure 4.8). Further, the capacitance decreases with increasing temperature. In Figure 4.12 (b) the capacitance equilvalent thickness (CET) (compare section 3.1.1.1) plot of the epitaxial grown layers are displayed. The oxides deposited at 2 A, 3 A and 4 A exhibit a κ of 20, 19 and 21, respectively, which is smaller compared to ferroelectric HfO (κ ~35 [80]). The permittivity is not influenced by the deposition temperature. From the CET plot the interfacial SiO_2 layer can be determined from the intersection of the

linear fit with the y-axis. The interfacial layer thickness is 2 nm, 2.9 nm and 3.8 nm for deposition currents of 2 A (~470 °C), 3 A (~580 °C) and 4 A (~660 °C), respectively. Thus, by increasing the temperature the SiO_2 layer grows thicker, explaining the reduced capacitance with increasing deposition temperature in Figure 4.12 (a).

The ferroelectricity of the epitaxial deposited HfGdO layers is investigated. In Figure 4.13 the PE (a) and current electric field (IE) (b) measurements of a 24 nm thick HfGdO layer deposited at 3 A is shown. In the PE measurement a hysteresis occurs already after 0 cycles and at an electric field of 2 MV/cm, which increases by larger electric field and cycling. The hysteresis does not show any saturation or steep switching comparable to ferroelectric HfO. The IV characteristics for the sample is shown in Figure 4.13 (b), giving an explanation for the shape of the hysteresis. The current does not exhibit peaks, which would indicate the switching of domains and thus ferroelectricity. The current increases with the increasing electric field and does not reveal and reduction at larger electric fields, so that the layers only reveal leakage. Thus, the layers exhibit leakage and no polarisation. The increasing leakage current induces an apparent polarisation, although no ferroelectric is present. The epitaxial layers grown at 2 A and 4 A exhibit the same behaviour. Thus, the grown layers are dielectrics.

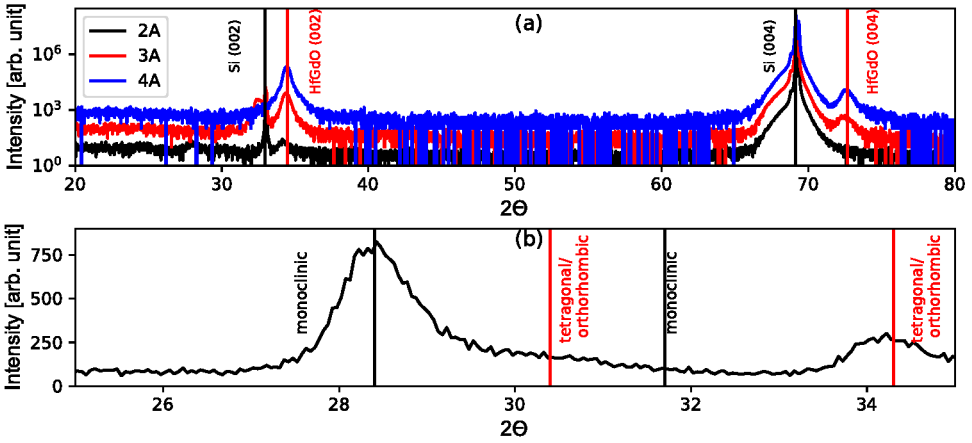

Figure 4.14: (a) XRD $\omega - 2\Theta$ out-of-plane scan of HfGdO deposited at a current through the substrate heater of 2 A (black curve), 3 A (red curve) and 4 A (blue curve). (b) GIXRD measurement of the sample deposited at a current through the substrate heater of 2 A.

To investigate the crystal structure of the grown epitaxial layers, they were char-

acterized by X-ray diffraction (Figure 4.14) especially ω-2Θ scans (a) and grazing incidence X-ray diffraction (GIXRD) (b). In the ω-2Θ-scan are four distinguishable reflections at 33°, 34.5°, 69.1° and 72.7°. The reflections at 33° and 69.1° correspond to the (002) and (004) substrate reflections of Si and are present for all three deposition temperatures. The reflection at 34.5° and 72.7° are the (002) and (004) reflections of the HfGdO and the determined out-of-plane lattice parameter is 5.2 Å, which fits to the c-axis of the tetragonal phase. Thus, the deposited layers are tetragonal and therefore dielectric. The intensity of the HfGdO reflections of the sample with a deposition current of 2 A are smaller compared to the other samples. Therefore, the 2 A sample is measured by GIXRD (Figure 4.14 (b)). Two peaks are visible at 28.5° and 34.5°. The positions of the monoclinic and the tetragonal/ orthorhombic peaks are laid over the GIXRD spectrum in Figure 4.14 (b). The peaks in the GIXRD spectrum refer to the monoclinic phase and and the tetragonal/ orthorhombic phase. The intensity of the monoclinic reflection is much larger as the one of the tetragonal/ orthorhombic reflection. Thus, at a heating current of 2 A a mostly monoclinic polycrystal is grown. Since the sample does not show any ferroelectric properties, the tetragonal/ orthorhombic reflection results most probably from the dielectric tetragonal phase.

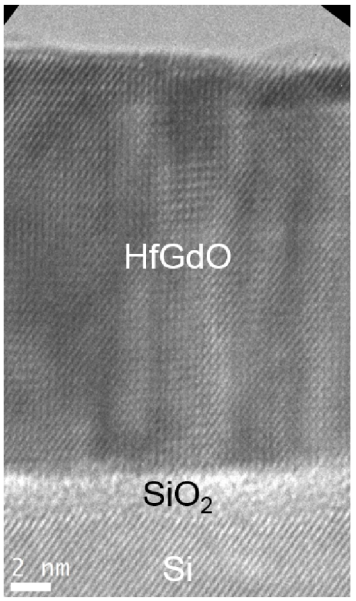

Figure 4.15: TEM image of epitaxial grown HfGdO on Si.

To check the oxide quality and to investigate the interface, the epitaxial grown HfGdO is investigated by transmission electron microscopy (TEM). A high-resolution TEM image of the epitaxial grown HfGdO layer is shown in Figure 4.15. At the

bottom the Si is visible, on which the HfGdO is grown. In between the HfGdO and the Si a bright, amorphous layer is visible, which is SiO_2. In the HfGdO the contrast and the orientation change. In the upper left part of the image diagonal lattice planes are visible, while in the center individual atoms are visible. Thus, the HfGdO layer is composed of individual grains, that are tilted against each other. The epitaxial grown layer is no single crystal, but a polycrystal, whose c-axis is oriented perpendicular to the substrate surface.

4.4 Ferroelectric HfO_2 with 5% Lu

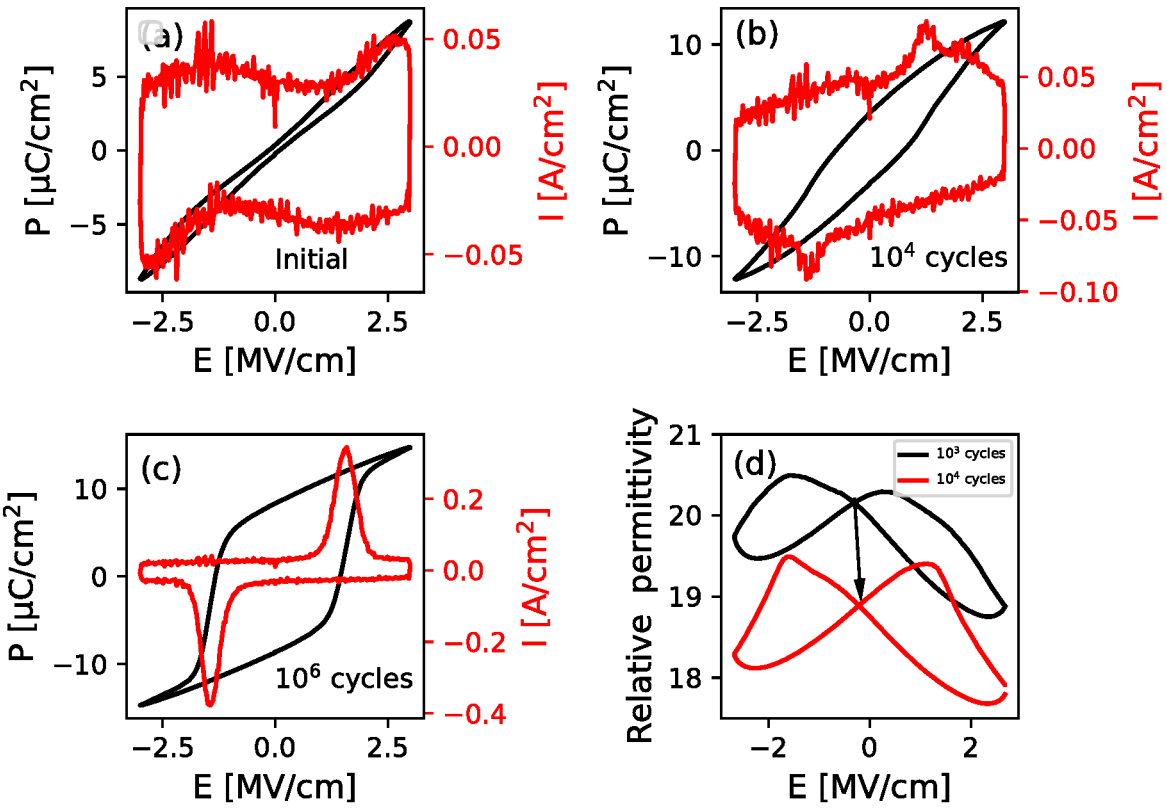

Figure 4.16: PE and IE measurements of a TiN/30 nm HfLuO/TiN/Pt stack annealed at 500 °C at the initial state (a), after 10^4 cycles (b) and after 10^6 cycles (c). CV measurement of the same sample after 10^3 (black) and 10^4 (red) cycles (d).

By adding Lu to the HfO the crystal structure of the HfO can be changed, too. In Figure 4.16 (a-c) polarisation electric field (PE) and current electric field (IE) measurements of a TiN/HfLuO (30 nm)/ TiN/Pt sample are shown. At the initial state (a) the PE curve exhibits a pinched hysteresis indicating either an antiferroelectric oxide or pinned domain walls. The IE curve exhibits a maximum current of 0.05 A/cm^2 at the initial state. After 10^4 cycles the hysteresis is not pinched any more with a remanent polarisation (P_r) of 3.5 µC/cm^2 and -3.2 µC/cm^2 and a

electric coercive field (E_c) of 0.8 MV/cm and -0.8 MV/cm. The current increases since the polarisation rises and reveals a maximum current of 0.09 A/cm^2. After 10^6 cycles the hysteresis reaches the maximum remanent polarisation (8.4 µC/cm^2 and -8.7 µC/cm^2 and E_c (1.4 MV/cm and -1.3 MV/cm). The current rises up to 0.35 A/cm^2. In Figure 4.16 (d) the permittivity of the sample is shown, calculated from a CV measurement assuming a layer thickness of 30 nm. After 10^3 cycles the permittivity at the cross section is 20.2 at an E of -0.3 MV/cm and after 10^4 cycles 18.9 at 0.2 MV/cm. Therefore, the permittivity and thus the capacity decrease by cycling and the curve shifts to the right.

For annealing temperatures in between 400 °C - 600 °C similar trends are observed. Annealing the sample at 700 °C changes the PE and IE curve of the sample as shown in Figure 4.17. The initial PE curve of the HfLuO annealed at 700 °C reveals no pinched hysteresis, but is ferroelectric from the beginning. The P_r rises from 5 µC/cm^2 and -3.8 µC/cm^2 to 10.6 µC/cm^2 and -9.8 µC/cm^2 after 10^4 cycles and is stable up to 10^6 cycles. The E_c increases from 0.7 MV/cm and -1.1 MV/cm at the initial state up to 1.1 MV/cm and -1.4 MV/cm after 10^4 cycles. The increasing polarisation is also visible in the IE curve. The current increases from 0.2 A/cm^2 at the initial state up to 0.4 A/cm^2 after 10^4 cycles.

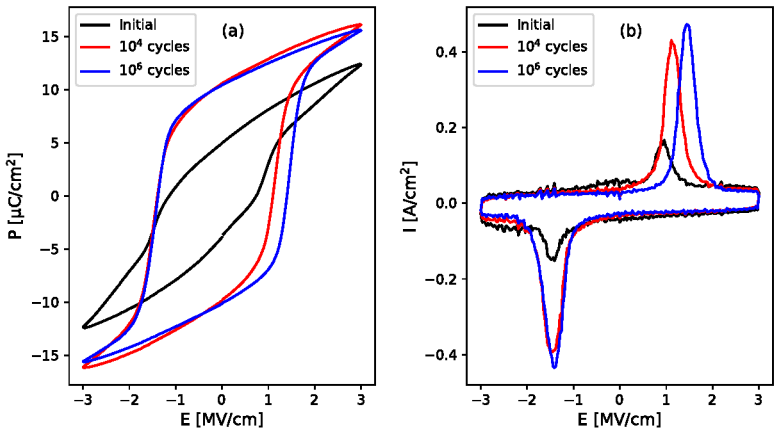

Figure 4.17: PE (a) and IE (b) measurement of a TiN/HfLuO (30 nm)/TiN/Pt sample annealed at 700 °C at the initial state and after cycling.

In Figure 4.18 the permittivity calculated from a CV measurement of a TiN/HfLuO (30 nm)/ TiN/ Pt stack annealed at 700 °C is shown after 10^3 and 10^4 cycles. The CV curve exhibits the typical butterfly shape of the ferroelectric capacitor. At the initial state the "butterfly" is not as significant as after cycling due to the wake-up

effect. After 10^3 cycles the cross section is at a permittivity of 20.2 at an electric field of -0.7 MV/cm decreasing to 18.6 at an electric field of -0.5 MV/cm. Thus, by cycling the permittivity decreases and the cross section shifts to a more positive electric field.

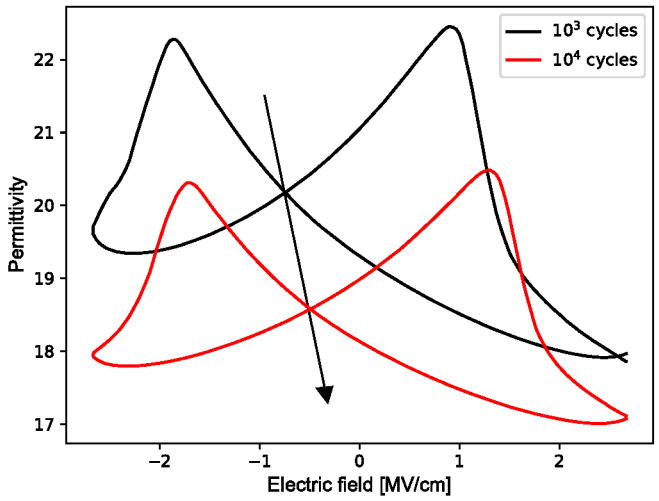

Figure 4.18: Influence of cycling on the permittivity of 30 nm HfLuO on TiN bottom electrode with TiN/ Pt top electrode annealed at 700 °C.

The durability of the HfLuO layer is investigated by Fatigue measurements. Therefore, the sample is successively cycled 10^4 times and the polarisation is measured in dependence of the applied electric field. The sum of the absolute values of the positive and the negative remanent polarisation (P_r) is calculated and the $2P_r$ is plotted against the number of cycles. In Figure 4.19 (a) the fatigue curves of the MOSCaps annealed at 700 °C (red curve) and annealed at 500 °C (black curve) are shown. The MOSCap annealed at 700 °C achieves its maximum polarisation of 20 µC/cm^2 already after 10^4 cycles and the $2P_r$ is stable afterwards. The MOSCap breaks after 10^6 cycles without reduced P_r . The MOSCap annealed at 500 °C reveals a polarisation of 6 µC/cm^2 after 10^4 cycles increasing up to 16 µC/cm^2 after 10^6 cycles. Afterwards, the P_r is stable until the MOSCap breaks after 10^7 cycles. Thus, the sample annealed at 500 °C does not reach its maximum polarisation at the beginning and achieves one order of magnitude more cycles before breakdown than the sample annealed at 700 °C. This could be related to the pinched hysteresis at the beginning of the PE measurements (see Figure 4.16), which could be caused by pinned domain walls or the antiferroelectric phase [97, 85]. The unpinning of domains or the transformation from the antiferroelectric, tetragonal phase requires the creation

and rearrangement of oxygen vacancies [84]. Those oxygen vacancies create leakage path, causing the failure of the device. Since the oxygen vacancies need to be created first, the growth of leakage path takes longer, compared to the sample annealed at 700 °C. To compare the crystal structure of the metal-insulator-metal capacitor (MIMCaps) GIXRD measurements were performed (Figure 4.19 (b)). Both curves (red curve: 700 °C and black curve: 500 °C) reveal the same shape with three distinguishable reflections at 28.4°, 30.4° and 31.7°. The reflections at 28.4° and 31.7° originate from the monoclinic phase, while the reflection at 30.4° originates from the tetragonal/ orthorhombic phase. Both MIMCaps exhibit monoclinic as well as tetragonal/ orthorhombic phase in a comparable ratio. Thus, the different polarisation characteristic seen in the PE and Fatigue measurements can not result from a different crystal structure of the MOSCaps, except a different ratio of tetragonal to orthorhombic phase.

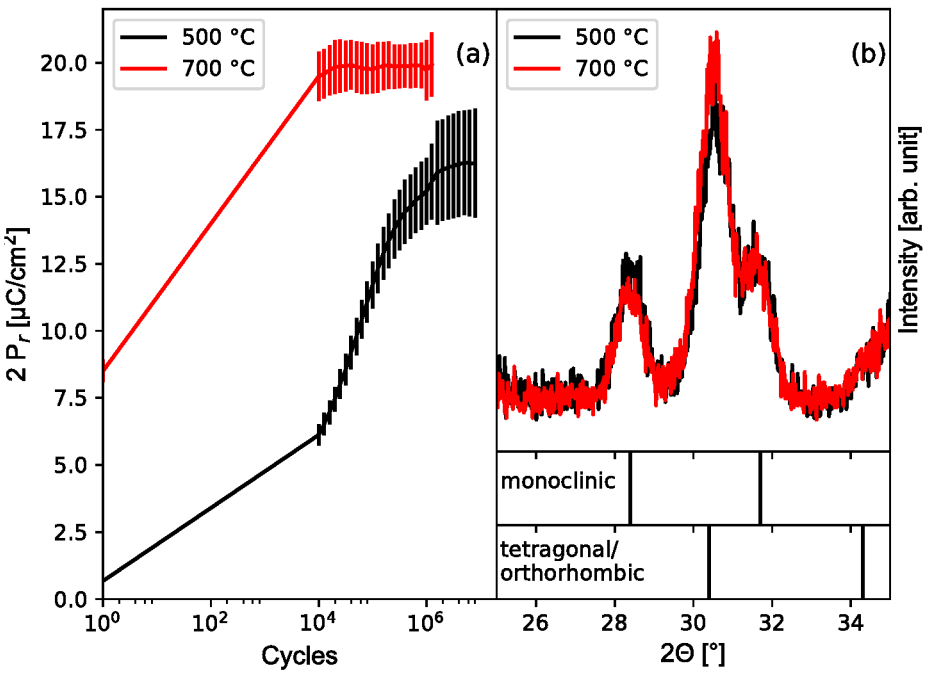

Figure 4.19: Fatigue (a) and GIXRD (b) measurements of a TiN/HfLuO (30 nm)/TiN/Pt sample annealed at 500 °C and 700 °C.

In Figure 4.20 bright and dark field images of the Si/TiN/HfLuO/TiN stack are shown. The bright field image (Figure 4.20 (a)) shows the interfaces in between the HfLuO and the TiN as well as the interface in between the TiN and the Si. In between the Si and the TiN a brighter amorphous layer is visible, which can be

identified as SiO_2. The HfLuO/ TiN interface is rough and individual grains are visible. One of the grains is showing Moire fringes. In Figure 4.20 (b) a dark field image of the stack is shown. The aperture is placed on the first ring of reflections as illustrated in the inset. Thus, only areas which scatter into the aperture appear bright. In the HfLuO layer a grain of 82 nm width is detected while in the TiN many grains with a width of approximately 10 nm are detected.

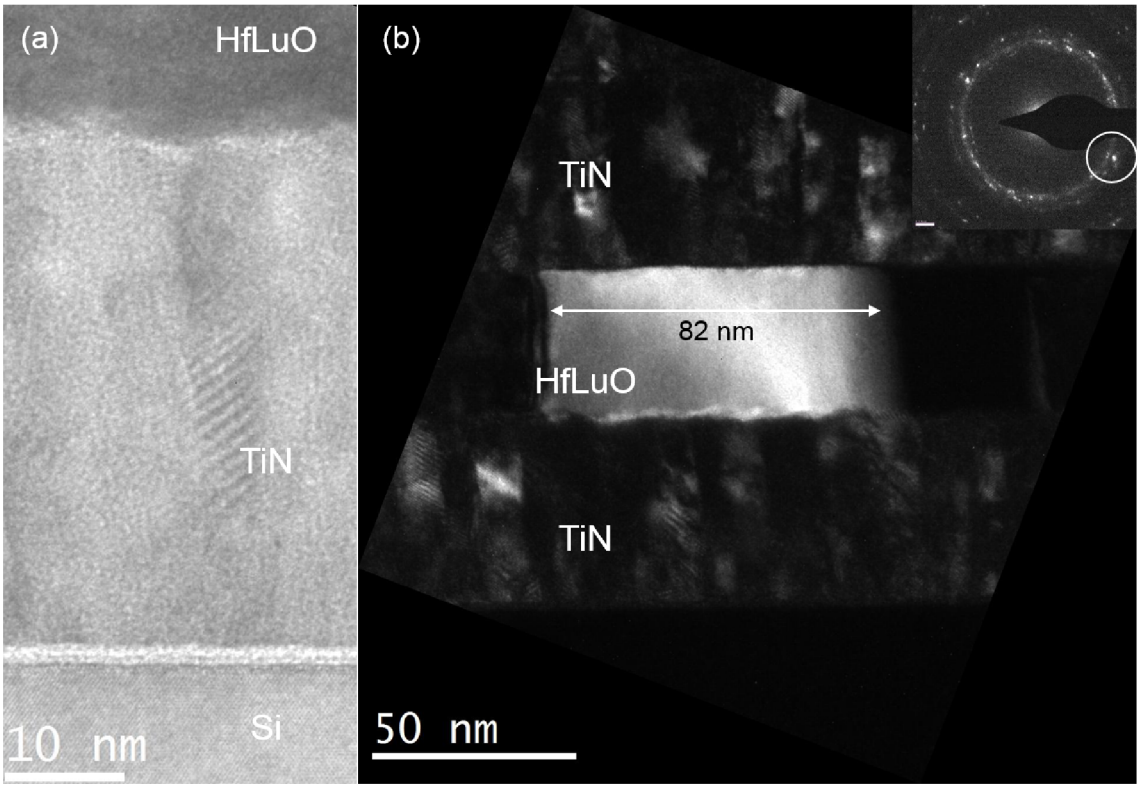

Figure 4.20: TEM images of a TiN/HfLuO 30 nm/TiN/Pt sample annealed at 700 °C. (a) Overview of the structure exhibiting a rough HfLuO/ TiN interface. (b) DF image of the HfLuO layer exhibiting grain sizes up to 82 nm in-plane. In the inset the diffraction pattern (DP) is displayed, revealing the position of the selected area diffraction aperture in the DP.

4.5 Ferroelectric HfO_2 with 3% Y

Beside ferroelectric HfO_2 deposited by PLD, first experiments with HfO_2 with 3% Y (HfYO) were carried out. 10 nm amorphous HfYO were deposited on sputtered TiN substrate by atomic layer deposition and subsequent 40 nm TiN were sputtered on top. As metal contact 50 nm Pt was deposited on top by e-gun and afterwards annealed in Ar for 30 s at various temperatures. The TiN in between the Pt contacts was etched away by reactive ion etching and SC1. In Figure 4.21 (a-c) the polarisation electric field (PE) and current electric field (IE) characteristics of a TiN/HfYO/TiN/Pt sample annealed for 30 s in Ar at 600 °C are shown. The three PE curves exhibit different hysteresis. The hysteresis at the initial state (Figure 4.21 (a)) is measured without cycling of the sample in a sweeping range of 0.2 MV/cm and reveals no hysteresis, because the electric field strength to switch the domains is not applied. The related IE curve (red curve in Figure 4.21 (a)) exhibits no increase in the current during the sweep. Applying a sweeping range of 0.5 MV/cm reveals an hysteresis of the HfYO layer with a remanent polarisation (P_r) of 10.7 µC/cm^2 and -10.9 µC/cm^2 at an coercive field strength (E_c) of 0.14 MV/cm and -0.13 MV/cm, respectively as shown in Figure 4.21 (b). In the corresponding IE curve two distinguishable peaks are revealed. After the sample was cycled 1000 times in a sweeping range of 0.5 MV/cm the hysteresis becomes steeper as displayed in Figure 4.21 (c) and the P_r increases to 15.8 µC/cm^2 and -15.9 µC/cm^2. The steepness of the HfYO layer is larger compared to HfGdO or HfLuO. Hence, the switching of the domains happens in the HfYO in a smaller range of the electric field. The current (Figure 4.21 (c) red) reveals two peaks, which are three times larger compared to the initial state (Figure 4.21 (a) red). Hence, more domains are activated after the cycling, so that more domains switch, causing an increased current. In Figure 4.21 (d) the polarisation (PE) (black) and the current (IE) (red) at an applied electric field of an equivalent sample annealed at 800 °C are shown. The PE curve exhibits P_r of 9.8 µC/cm^2 and -11.2 µC/cm^2 at an coercive field strength (E_c) of 0.2 MV/cm and -0.23 MV/cm, respectively. Thus, the polarisation is comparable to the initial polarisation of the sample annealed at 600 °C. In contrast to the sample annealed at 600 °C, the 800 °C sample does not exhibit steep switching. In fact the hysteresis exhibits a bump during the switching of the polarisation, indicating that the polarisation is switched in two steps. In the IE curve (Figure 4.21 (d) red) four peaks are visible. The peak in the IE curve is induced by the switching of the domains. Since two peaks are present for each switching, the domains tend to switch at different applied electric fields. The first peak is below 0.2 MV/cm and -0.2 MV/cm, which is comparable to the IE peaks for the sample annealed at 600 °C. Those domains seem to be mobile and switch at E_c . For the other domains, that induce the second peak, a larger applied electric field is necessary. Thus, those domains are pinned by electrical defects, that impede the switching of the domains. Therefore, besides the

energy to switch the domains, the applied electric field must provide the energy to release the domains from the electrical defects. Thus, the domains switch in two steps, since they are partially pinned by electrical defects, preventing steep switching of the polarisation as displayed in the hysteresis. After cycling of the sample 1000 times the leakage increases, causing the failure of the sample. This behaviour assist the assumption of electrical defects, because the present electrical defects may form a leakage path by cycling. For further application like NCFETs an annealing temperature of 600 °C is favourable, since the sample tends to have less electrical defects, that pin the domains and form a leakage path by cycling.

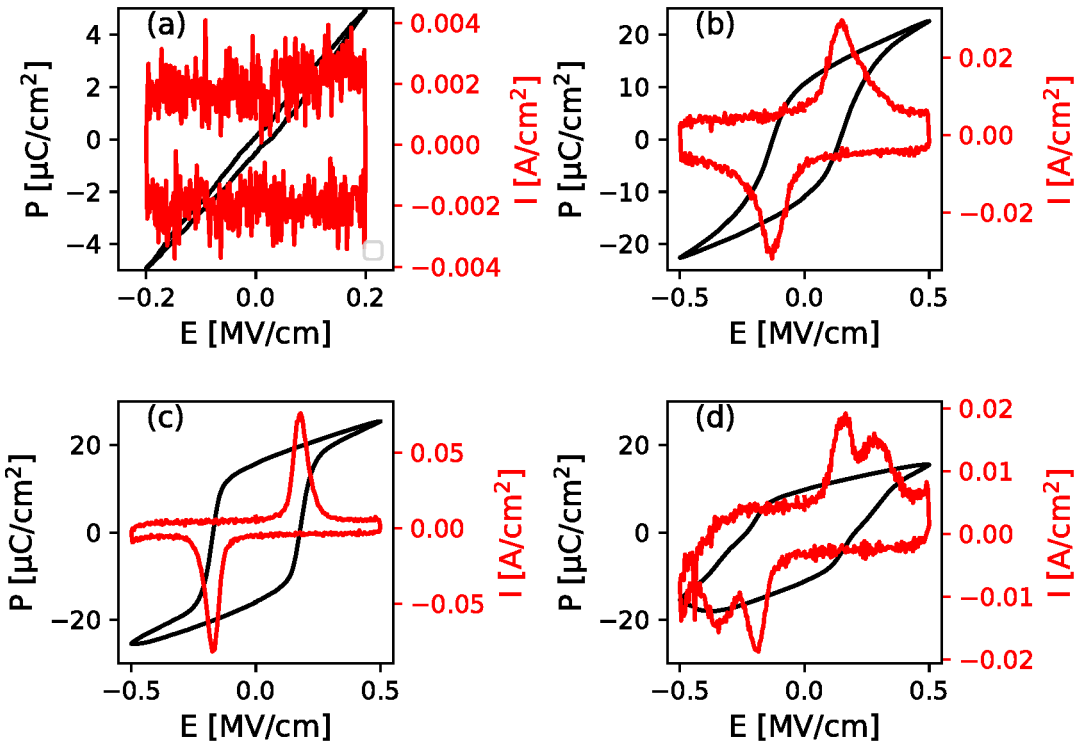

Figure 4.21: Polarisation and current characteristics of an TiN/HfYO/TiN/Pt sample annealed for 30 s in Ar at 600 °C at the initial state (a & b) and after cycling (c). Polarisation and current characteristics of a similar sample annealed at 800 °C for 30 s in Ar (d).

4.6 Discussion

In the following the results of the investigated ferroelectric layers are discussed in respect to literature.
By optimizing the process parameters of the pulsed laser deposition (PLD) grown HfGdO and HfLuO and the ALD deposited HfYO layers, the ferroelectric, orthorhombic phase was stabilized, achieving a maximum remanent polarisation (P_r) of 12 µC/cm^2, 12 µC/cm^2 and 20 µC/cm^2, respectively. The properties of the investigated ferroelectric HfO and selected values in literature are listed in table 4.2. The ALD grown HfYO exhibits a larger P_r than the PLD grown layers, indicating either a larger amount of orthorhombic HfO or an beneficial orientation of the polycrystal layer with the polar axis perpendicular to the interface. Further, the polarisation switch in the hysteresis is steeper, meaning that the domains in the layer switch in a closer region of the applied electric field. In a theoretical ferroelectric the whole polarisation is switched at the coercive electric field, but due to defects, that pin the domains, different electric fields are required to unpin and subsequently switch the domains. [12] Thus, the domains in the ALD layers must exhibit less defects or a more homogenous distribution of defects than HfGdO and HfLuO. The remanent polarisation of HfGdO and HfLuO is comparable to other PLD grown HfO like HfGdO (13 µC/cm^2) [98] and HfO with Y (13 µC/cm^2) [88], while the HfYO is comparable to values for HfYO deposited by chemical solution deposition (CSD) (20 µC/cm^2 [99]), too.

Table 4.2: Permittivity and remanent polarisation of ferroelectric HfO_2.

Composition	Deposition method	Permittivity	P_r [µC/cm^2]
HfGdO	PLD	34	12
HfLuO	PLD	22.5	12
HfYO [88]	PLD	40	13
HfYO [99]	CSD	22.5	20
HfYO	ALD	-	20

The maximum polarisation and steepest hysteresis were measured after a 1000 cycles. A twice as large polarisation is measured compared to the one at the initial state for HfGdO (see Figure 4.8), while the increase is smaller for HfYO. By cycling the domains are oriented parallel to the electric field and pinned domains are unpinned, so that more domains contribute to the overall polarisation. This effect is called "wake-up". [84, 100] Furthermore, by cycling additional oxygen vacancies are generated [84], that transform residual tetragonal phase into the orthorhombic

phase [85]. A ferroelectric layer, which exhibits the maximum polarisation already at the initial state is favourable, but due to the crystallization of the ferroelectric layer during the anneal, the domains are oriented randomly.
By cycling the relative permittivity of the PLD grown HfGdO and HfLuO decreased, which may result from the formation of a TiO_2 layer during cycling, which serves as scavenging material at the top and bottom electrode [101]. The decrease of the relative permittivity is already reported for PLD grown HfYO [88]. The relative permittivity of the HfLuO is 22.5, while the HfGdO reveals a relative permittivity of 34. The larger permittivity of HfGdO is comparable to other ferroelectric layers like HfYO deposited by chemical solution deposition (32) [99] or by PLD (40) [88]. The lower permittivity of the HfLuO results from the low-κ, monoclinic phase in addition to the orthorhombic phase, which is determined from the peak at 28° in the grazing incidence X-ray diffraction (GIXRD) measurement (Figure 4.19 (b)). In comparison the HfGdO reveals a lower ratio of monoclinic phase (Figure 4.10), which can be distinguished from the ratio of the orthorhombic/tetragonal reflection (30.5°) and the monoclinic reflection (28°). The small amount of the monoclinic phase indicates, that the HfGdO is close to the optimum process parameters, while HfLuO needs further optimization. Most probably the Lu concentration should be changed, because the remaining process parameters were explored as discussed in the following paragraph.
The properties of the ferroelectric layers strongly depend on the process parameters top and bottom electrode and annealing temperature, which were investigated for HfGdO layers. The results are discussed below.
By the top and bottom electrode of the metal-insulator-metal (MIM) structure the ferroelectrical properties are essentially modified (see Figure 4.11). The best ferroelectric properties i.e. the largest polarisation, steepest switching and largest portion of orthorhombic phase were found for a TiN/HfGdO/TiN stack. By omitting the TiN top layer the ferroelectric properties dwindle, because the capping of the ferroelectric layer by a top electrode hinders the volume expansion and the shearing of the unit cell during the crystallisation. In this way the formation of the monoclinic phase is reduced and the growth of the orthorhombic phase is supported. [86, 102] In comparison to the TiN/HfGdO stack, the TaN/HfGdO stack reduces the polarisation and the steep switching of the hysteresis, most probably due to the rougher surface, which causes a pinning of the domains, that reduces the full polarisation [63].
Besides the stack structure the annealing temperature is crucial for the ferroelectric properties. Low annealing temperatures hinder the complete crystallization of the HfGdO layer, which becomes visible by the lower P_r and a reduced orthorhombic peak in GIXRD measurements (compare Figure 4.9 and Figure 4.10). If an annealing temperature above a critical temperature is chosen, all investigated ferroelectric HfO_2 (HfO) exhibit leakage currents. The critical temperature varies for the added elements. Gao et al. calculated by first principle calculations, that ions

in HfO_2 would decrease the energy for oxygen vacancy formation [103, 104], which is crucial for the formation of the orthorhombic, ferroelectric phase [85]. Therefore, larger annealing temperatures support the formation of oxygen vacancies, stabilizing the orthorhombic phase and increasing the polarisation. Depending on the ion, different annealing temperatures are necessary, to generate sufficent oxygen vacancies. Above critical temperatures a critical amount of oxygen vacancies is generated, forming conductions paths, that explain the failure of the devices by leakage. Zhao et al. reported on the formation of conduction paths in HfO with Gd, that were used for resistive switching [104]. The influence of the oxygen vacancies becomes obvious by the comparison of HfYO annealed at 600 °C and 800 °C (compare Figure 4.21). Up to an annealing temperature of 600 °C the P_r and the steepness of the hysteresis increases. In comparison to the initial hysteresis of the layer annealed at 600 °C, the hysteresis of the layer annealed at 800 °C reveals a smooth polarisation switching and a lower polarisation. The additional generated oxygen vacancies at 800 °C are defects, that are randomly distributed and pin the domains, so that the domains need varying applied electric fields to switch, causing a smooth hysteresis. Furthermore, some pinned domains are not switched, resulting in a lower polarisation. The pinning of the domains become obvious in the current voltage (IV) characteristic by the peak, which are induced by the switching domains, generating the measured current increase. The layer annealed at 600 °C exhibits only two peaks at 0.014 A/cm^2 and -0.013 A/cm^2, that is broadened, too, due to randomly orientated domains and arbitrary pinning of domains by the randomly distributed oxygen vacancies. In contrast to this layer, the IV measurement of the layer annealed at 800 °C reveals four peaks, so that the domains in the layer annealed at 800 °C switch in two steps, because of their varying pinning by oxygen vacancies [76, 105, 106]. Cycling of the layer annealed at 800 °C causes failure of the device by leakage, since more oxygen vacancies are generated [84], forming leakage paths, while the layer annealed at 600 °C exhibits an increased polarisation [103, 104].

In contrast to HfYO and HfGdO, the investigated HfLuO revealed different properties depending on the annealing temperature. At 500 °C the layer exhibits a pinched hysteresis, which can result either from an antiferroelectric HfO or pinned domain walls [12]. The pinched hysteresis vanishes after 1000 cycles and the hysteresis shows the typical ferroelectric state. HfO exhibits an antiferroelectric phase, which is attributed to the tetragonal phase [8, 85]. By an applied electric field the antiferroelectric tetragonal phase can transform into the ferroelectric, orthorhombic phase, because the barrier between the two phases is very low and the orthorhombic phase is preferred by an applied electric field to the tetragonal phase [85]. The other possibility is the pinning and unpinning of the domain walls. At the initial state the oxygen vacancies are distributed inhomogeneous at the grain boundaries of the HfLuO [76], pinning the domain walls. Some of the pinned domains switch at an applied positive electric field and others at an applied negative electric field, so that the

hysteresis is pinched. The other pinned domains do not switch and consequently do not contribute to the polarisation. During the cycling the layer "wakes-up", due to the homogeneous redistribution of the oxygen vacancies, increasing the polarisation and resulting in a ferroelectric hystersis. [105, 106] In contrast the HfLuO sample annealed at 700 °C reveals a ferroelectric hysteresis from the beginning. Therefore, the higher temperature either prevents the antiferroelectric, tetragonal phase or generates a homogeneous distribution of oxygen vacancies. A difference in the crystal structure can not be distinguished by GIXRD (see Figure 4.19 (b)), because the peaks of the tetragonal and the orthorhombic phase overlap. A different ratio of tetragonal to orthorhombic phase at the different temperatures is possible.
Fatigue measurements, that measure the durability of the polarisation, show a different behaviour of the layers. The sample annealed at 500 °C exhibits an increasing polarisation up to 10^7 cycles (compare Figure 4.19), while the HfLuO sample annealed at 700 °C reveals its maximum polarisation already after 10^4 cycles and survives 10^6 cycles. Thus, the sample annealed at 500 °C went through either a change from antiferroelectric to ferroelectric or rearrangement of oxygen vacancies, leading to an increase in polarisation. In addition, the sample annealed at 500 °C seems to have less oxygen vacancies, since failure of the device occurs one magnitude of cycles later than for the sample annealed at 700 °C. In comparison to PLD grown HfYO the sample annealed at 500 °C survives a comparable amount of cycles [88].

Most ferroelectric HfO are polycrystalline, so that the crystals are oriented randomly. Since the polar axis of the ferroelectric orthorhombic phase (space group $Pbc2_1$) is the c-axis [80], an orientation of the c-axis orthogonal to the surface is favourable to enhance the out-of-plane polarisation of the layer. Therefore, epitaxial grown layers of HfGdO were deposited on highly doped Si (compare section 4.3), but all layers were dielectric. The layer deposited at a heating current of 3 A (~580 °C) and of 4 A (~660 °C) exhibited the tetragonal phase, while the layer deposited at 2 A revealed a polycrystalline layer of monoclinic and tetragonal phase (see Figure 4.14). The polycrystalline layer is not of further interest, because no preferred orientation is present. The process to form the orthorhombic phase is discussed in the following, to understand the missing parameter to stabalize the ferroelectric phase. The formation of the ferroelectric orthorhombic phase requires the prevention of the formation of the monoclinic phase. Therefore, a small grain size (~4 nm) is necessary [107]. During the anneal the tetragonal phase instead of the monoclinic phase forms, if the grains size is small enough. Subsequently, in-plane compressive stress induces the formation of the tetragonal phase into the orthorhombic, ferroelectric phase [85]. The reason for the in-plane stress was investigated for ALD deposited $Hf_{0.5}Zr_{0.5}O_2$. The cause for the in-plane stress is the neighbouring nuclei touch each other during growth. [108, 82] The in-plane stress is further increased by a capping layer [86, 102]. The epitaxial layers grown at a heating current of 3 A and 4 A reveal the tetragonal phase, although the critical grain size may be

exceeded (see Figure 4.15). Thus, the tetragonal phase seems to be favoured at larger substrate temperatures. A transformation of the tetragonal phase into the orthorhombic phase is possible under an applied electric field [85]. Because of the orientation of the tetragonal crystal, a transformation into the orthorhombic phase is pointless as explained in the following. The tetragonal HfO exhibits its c-axis perpendicular to the surface, which is the longest axis of the tetragonal phase. In contrast the non-polar b-axis of the orthorhombic HfO is the longest one and the polar c-axis the shortest one. During a phase transition the tetragonal out-of-plane c-axis would become the b-axis of the ferroelectric orthorhombic phase, while the polar c-axis of the orthorhombic phase would be parallel to the substrate, generating an in-plane ferroelectricity, which is useless for the NCFET. [82]

4.7 Summary

In conclusion, the ferroelectric, orthorhombic phase was stabilized in the investigated HfGdO (12 µC/cm^2), HfLuO (12 µC/cm^2) and HfYO (20 µC/cm^2), revealing ferroelectric characteristics comparable to literature. The HfYO layer reveals the largest polarization and the steepest switching, so that it was used by Han et al. for the fabrication of a NCFET [109]. The ferroelectric properties of the oxides depend on the process parameters, whereby a TiN bottom and top electrode enhances the polarisation, because they hinder the shearing of the unit cell and the volume expansion during the crystallization, which favours the formation of the ferroelectric, orthorhombic phase [86, 102]. An increasing annealing temperature generates an enhanced polarization, up to a critical temperature, above which leakage via conduction paths of oxygen vacancies occurs. By an increasing annealing temperature more oxygen vacancies are generated [103, 104], that stabilize the ferroelectric, orthorhombic phase [85], until above a critical temperature the oxygen vacancies form conduction paths, leading to the failure of the device. The ferroelectric properties of the HfLuO layer depend on the annealing temperature. At an annealing temperature from 400 °C to 600 °C, the layer reveal a pinned hysteresis, which could indicate antiferroelectricity or pinned domains. After a 1000 cycles the hysteresis shows a ferroelectric shape. At a temperature of 700 °C the HfLuO becomes ferroelectric. The epitaxial growth of HfGdO formed a dielectric tetragonal phase, instead of the orthorhombic phase with an out-of-plane polar axis, to enhance the polarization

5 Conclusion

In this thesis epitaxial ternary rare-earth oxides on GaN for power devices and ferroelectric HfO_2 for the integration in negative capacitance field-effect-transistors were investigated. The aim of this thesis is the qualification of the oxides in respect to their electrical and structural properties. More precisely, the ternary rare-earth oxides were analysed in respect to their band gap and permittivity, and the formation of the hexagonal phase was investigated. With respect to the ferroelectric layers, the influence of the processing parameters on the ferroelectric characteristics were determined.

Ternary rare-earth oxides are promising candidates for future gate dielectrics. While binary rare-earth oxides reveal either a large relative permittivity or a large band gap, ternary rare-earth oxides should exhibit both, making them promising candidates for future gate oxides. [1] Amorphous and hexagonal $GdScO_3$ (GSO) and hexagonal $LaLuO_3$ (LLO) were epitaxial grown by pulsed laser deposition on GaN and the electrical and structural properties were investigated.
The determined permittivities of the layers are 23, 30 and 32 for amorphous GSO, hexagonal GSO and hexagonal LLO, respectively, and all investigated layers have a band gap larger than 5 eV. Thus, the layers are suitable for gate dielectrics and the permittivity is larger compared to the binary oxides Gd_2O_3 (12) [31], Sc_2O_3 (14) [54], La_2O_3 (23.5) [55] and Lu_2O_3 (15) [57].
Current-voltage measurements reveal an asymmetric shape, with larger leakage currents at positive than at negative applied gate voltage, which is explained by the staggered band structure of GaN and the ternary rare-earth oxides. The valence band of the oxide is below the one of the GaN, but the conduction band of the oxides is in the band gap of the GaN. Therefore, the electrons face no potential barrier at positive gate voltage, but a larger barrier at negative voltages.
Besides the eminent band gap and permittivity the layers reveal some electrical defects, which are observed by capacitance-voltage (CV) measurements. During the measurement the CV curve shifts to more positive voltage because of negative charges, whereby larger gate voltages induce a larger shift. The shift is stable and does not degrade by time.
Due to ab-initio calculations the hexagonal phase of $GdScO_3$ and $LaLuO_3$ is not thermodynamically stable. Therefore, the grown layers and especially the interface

between the oxides and the GaN were investigated, to understand the stabilization of the oxides.
Reciprocal space maps of the hexagonal layer reveal a fibre texture with the c-axis as fibre axis perpendicular to the substrate. Since the space group can not be determined by X-ray diffraction, automated diffraction tomography measurements are performed, narrowing the space group of the hexagonal LLO and GSO down to P- -c. Thus, the possible space groups are $P6_3mc$, P-62c or $P6_3|mmc$, of which the space group $P6_3|mmc$ is most probably, since it is the one of hexagonal La_2O_3 [61].
For the epitaxial growth especially the interface is important, so that it was investigated by transmission electron microscopy. Hexagonal $GdScO_3$ (GSO), $LaLuO_3$ (LLO) and $SmScO_3$ (SSO) exhibit a blurry contrast at the interface due to tilted domains, which absorb the tension because of the lattice mismatch of the ternary rare-earth oxide and GaN. Further, a decomposition at the interface is observed. Hexagonal GSO on GaN reveals twice as much Sc as Gd at the interface, because hexagonal Sc_2O_3 has a 5% smaller a-axis [38], which would reduce the lattice mismatch to the GaN in comparison to GSO. The SSO reveals a decomposition of Sm and Sc at the interface, too, although the Sc enrichment along the interface varies. Hexagonal LLO only reveals a slight Lu enrichment at the interface. The hexagonal scandates reveal another relaxation mechanism. The distance at the interface in between the scandate and the GaN is enhanced, indicating weaker bonds, to reduce the tension.
The large relative permittivity (>30) and the good insulating properties of the hexagonal GSO and LLO make them suitable candidates for future gate dielectrics in transistors. In future studies, the space group will be defined and the found space group and structural properties will be used, to understand the formation of the hexagonal phase.

To overcome the limitation of the subthreshold slope (SS) of 60 mV/dec of a MOSFET, Salahuddin et al. proposed an improved device structure for the standard metal-oxide-semiconductor field-effect-transistor (MOSFET). Adding an additional ferroelectric layer in between the gate oxide and the gate metal, a negative capacitance field-effect-transistor (NCFET) is generated. The ferroelectric layer exhibits a negative capacity in the region of zero polarisation, that induces a voltage amplification of the gate voltage and in this way the SS limit of 60 mV/dec is overcome. [9, 10] In this thesis metal-insulator-metal stacks with ferroelectric HfO_2 with 5% Gd (HfGdO), HfO_2 with 5% Lu (HfLuO) and HfO_2 with 3% Y (HfYO) are investigated and qualified for the use in a NCFET. Amorphous HfO_2 (HfO) with additional Gd, Lu or Y is deposited by pulsed laser deposition (PLD) and atomic layer deposition (ALD), and subsequently annealed to form the orthorhombic, ferroelectric phase.
The ferroelectric phase was stabilized in all investigated HfO, whereby the PLD grown HfLuO and HfGdO reveal a remanent polarisation (P_r) of 12 $\mu C/cm^2$, which is comparable to values reported from other PLD grown layers [98, 88]. ALD

grown HfYO reveals the largest remanent polarisation (20 µC/cm^2) and the steepest switching. HfLuO reveals a relative permittivity of 22.5 and HfGdO one of 34, while most ferroelectric HfO exhibit a relative permittivity of 32-40 [99, 88]. The low permittivity of HfLuO could be related to the present monoclinic phase, which has a relative permittivity of 17 [73]. Grazing incidence X-ray diffraction measurements reveal less monoclinic crystals in the HfGdO than in the HfLuO, explaining the larger relative permittivity of HfGdO.
All investigated ferroelectric layers reveal an increasing polarisation after 1000 cycles ("wake-up"), due to the formation and redistribution of oxygen vacancies, that are necessary to stabilize the ferroelectric, orthorhombic phase of HfO_2 and to unpin the domains [105, 106].
For the optimization of the ferroelectric properties the process parameters of the metallization and the annealing temperature were investigated. A capping TiN top layer improves the ferroelectric properties like the remanent polarisation, because during the crystallization the in-plane stress of the HfO is increased. In this way, the stabilization of the orthorhombic phase is supported. [86, 102] Additionaly, more oxygen vacancies are formed, that stabilize the orthorhombic phase [103, 104, 105, 106]. Above a critical annealing temperature too many oxygen vacancies are generated, that form a leakage path and cause failure of the device [103, 104].
The ferroelectric HfO layers are polycrystalline, since they transform from the amorphous into the orthorhombic phase during an anneal, so that the polar axis is oriented randomly. To grow ferroelectric HfO_2 with a preferred orientation, in particular an out-of-plane polar axis, epitaxial HfGdO layers were deposited by pulsed laser deposition. Epitaxial HfGdO does not reveal any ferroelectricity, because the tetragonal phase is formed. To form the orthorhombic phase in-plane stress is necessary, that is induced during the crystallization and by a capping layer. Epitaxial grown layers lack this stress and therefore are dielectric. [85, 86, 102]
The HfLuO exhibits varying properties depending on the annealing temperature, revealing a pinched hysteresis at the initial state and a ferroelectric hysteresis after cycling, if annealed at 500 °C. The pinched hysteresis indicates either an antiferroelectric phase at the beginning, which would be the tetragonal phase, transforming into the orthorhombic phase by cycling [8, 85] or oxygen vacancies, that pin the domains and are redistributed by cycling [76].
The results show the good ferroelectric properties of the investigated HfO_2, that can be implemented into transistors, so that the investigated oxides will be used for NCFETs as shown by Han et al. [109]. Further, the generation and the influence of the oxygen vacancies on the ferroelectricity and the failure of the oxide will be investigated, to extend the durability and to increase the stability of the polarization.

Bibliography

[1] O. Engström, *The MOS System*. Cambridge University Press, 2014.

[2] A. Schäfer, K. Rahmanizadeh, G. Bihlmayer, M. Luysberg, F. Wendt, A. Besmehn, A. Fox, M. Schnee, G. Niu, T. Schroeder, S. Mantl, H. Hardtdegen, M. Mikulics, and J. Schubert, "Polymorphous GdScO3 as high permittivity dielectric," *Journal of Alloys and Compounds*, vol. 651, pp. 514–520, 2015.

[3] A. Schäfer, F. Wendt, S. Mantl, H. Hardtdegen, M. Mikulics, J. Schubert, M. Luysberg, A. Besmehn, G. Niu, and T. Schroeder, "Hexagonal LaLuO3 as high-κ dielectric," *Journal of Vacuum Science & Technology B, Nanotechnology and Microelectronics: Materials, Processing, Measurement, and Phenomena*, vol. 33, no. 1, p. 01A104, 2015.

[4] A. B. Schäfer, *Growth and characterization of crystalline rare-earth based gate oxide thin films for the application in nanotechnology*. PhD thesis, RWTH Aachen, 2015.

[5] J. Lutz, *Halbleiter-Leistungsbauelemente*. Springer-Verlag Berlin Heidelberg, 2 ed., 2012.

[6] S. Huang, Q. Jiang, S. Yang, C. Zhou, and K. J. Chen, "Effective passivation of AlGaN/GaN HEMTs by ALD-grown AlN thin film," *IEEE Electron Device Letters*, vol. 33, no. 4, pp. 516–518, 2012.

[7] G. Meneghesso, G. Verzellesi, F. Danesin, F. Rampazzo, F. Zanon, A. Tazzoli, M. Meneghini, and E. Zanoni, "Reliability of GaN high-electron-mobility transistors: State of the art and perspectives," *IEEE Transactions on Device and Materials Reliability*, vol. 8, no. 2, pp. 332–343, 2008.

[8] U. Schroeder, E. Yurchuk, J. Müller, D. Martin, T. Schenk, P. Polakowski, C. Adelmann, M. I. Popovici, S. V. Kalinin, and T. Mikolajick, "Impact of different dopants on the switching properties of ferroelectric hafniumoxide," *Japanese Journal of Applied Physics*, vol. 53, no. 8S1, p. 08LE02, 2014.

[9] S. Salahuddin, "Can the subthreshold swing in a classical FET be lowered below 60 mV/decade?," *IEEE ELECTRON DEVICE LETTERS,*, pp. 1–4, 2008.

[10] S. Salahuddin, "Use of Negative Capacitance to Provide Voltage Amplification for Low Power Nanoscale Devices," *Nano Lett*, 2008.

[11] AixACT, *TF ANALYZER 2000 FE-Module*. AixACT, 2016.

[12] L. Spieß, G. Teichert, R. Schwarzer, H. Behnken, and C. Genzel, *Moderne Röntgenbeugung*. Vieweg+Teubner, 2009.

[13] H. Bubert and H. Jennet, *Surface and Thin Film Analysis*. Weinheim, FRG: Wiley-VCH Verlag GmbH, feb 2002.

[14] S. Miyazaki, "Characterization of high-k gate dielectric/silicon interfaces," *APPLIED SURFACE SCIENCE*, vol. 190, no. 1-4, pp. 66–74, 2002.

[15] G. Friedbacher and H. Bubert, *Surface and Thin Film Analysis*. Wiley-VCH Verlag GmbH & Co. KGaA, 2011.

[16] D. B. Williams and C. B. Carter, *Transmission Electron Microscopy*. Springer Science & Business Media, 2009.

[17] M. Luysberg, M. Heggen, and K. Tillmann, "FEI Tecnai G2 F20," *Journal of large-scale research facilities JLSRF*, vol. 2, 2016.

[18] A. Claverie and M. Mouis, *Transmission Electron Microscopy in Micro-Nanoelectronics*. Hoboken, NJ USA: John Wiley & Sons, Inc., dec 2012.

[19] U. Kolb, T. Gorelik, C. Kübel, M. T. Otten, and D. Hubert, "Towards automated diffraction tomography: Part I-Data acquisition," *Ultramicroscopy*, vol. 107, no. 6-7, pp. 507–513, 2007.

[20] U. Kolb, T. Gorelik, and M. T. Otten, "Towards automated diffraction tomography. Part II-Cell parameter determination," *Ultramicroscopy*, vol. 108, no. 8, pp. 763–772, 2008.

[21] F. Brent and J. M. Howe, *Transmission Electron Microscopy and Diffractometry of Materials*. Berlin, Heidelberg: Springer Berlin Heidelberg, 2008.

[22] S. J. Pennycook and P. D. Nellist, *Scanning Transmission Electron Microscopy*.

New York, NY: Springer New York, 2011.

[23] A. Kovács, R. Schierholz, and K. Tillmann, "FEI Titan G2 80-200 CREWLEY," *Journal of large-scale research facilities*, vol. 2, 2016.

[24] W. KERN and D. Puotinen, "Cleaning solutions based on hydrogen peroxide for use in silicon semiconductor technology," *RCA Rev.*, vol. 31, p. 187, 1970.

[25] H. Steffen and H. Bausch, *Elektrotechnik*. B. G. Teubner Verlag / GWV Fachverlage GmbH, 2007.

[26] D. G. Schlom and J. H. Haeni, "A Thermodynamic Approach to Selecting Alternative Gate Dielectrics," *MRS Bulletin*, vol. 27, pp. 198–204, mar 2002.

[27] R. Gross and A. Marx, *Festkörperphysik*, vol. 1. Oldenbourg Wissenschaftsverlag GmbH, 2012.

[28] S. M. Sze and K. N. Kwok, *Physics of Semiconductor Devices*. John Wiley & Sons, Inc., 2007.

[29] P. Misra, Y. Sharma, and R. S. Katiyar, "Effect of Current Compliance on Resistive Switching Characteristics of Amorphous Ternary Rare Earth Oxide $SmGdO_3$ Thin Films Grown by Pulsed Laser Deposition," *ECS Transactions*, vol. 61, pp. 133–138, mar 2014.

[30] C. Zhao, T. Witters, B. Brijs, H. Bender, O. Richard, M. Caymax, T. Heeg, J. Schubert, V. V. Afanas'ev, A. Stesmans, and D. G. Schlom, "Ternary rare-earth metal oxide high-κ layers on silicon oxide," *Applied Physics Letters*, vol. 86, p. 132903, mar 2005.

[31] H. D. B. Gottlob, T. Echtermeyer, T. Mollenhauer, J. K. Efavi, M. Schmidt, T. Wahlbrink, M. C. Lemme, H. Kurz, M. Czernohorsky, E. Bugiel, H. J. Osten, and A. Fissel, "CMOS integration of epitaxial Gd_2O_3 high-k gate dielectrics," *Solid-State Electronics*, vol. 50, no. 6, pp. 979–985, 2006.

[32] M. Leskelä and M. Ritala, "Rare-earth oxide thin films as gate oxides in MOSFET transistors," *Journal of Solid State Chemistry*, vol. 171, no. 1-2, pp. 170–174, 2003.

[33] P. B. Klein, S. C. Binari, K. Ikossi, A. E. Wickenden, D. D. Koleske, and R. L. Henry, "Current collapse and the role of carbon in AlGaN/GaN high electron mobility transistors grown by metalorganic vapor-phase epitaxy," *Ap-*

plied Physics Letters, vol. 79, no. 21, pp. 3527–3529, 2001.

[34] T. Hashizume, S. Ootomo, and H. Hasegawa, "Suppression of current collapse in insulated gate AlGaN/GaN heterostructure field-effect transistors using ultrathin Al_2O_3 dielectric," *Applied Physics Letters*, vol. 83, no. 14, pp. 2952–2954, 2003.

[35] J. Shi, L. F. Eastman, X. Xin, and M. Pophristic, "High performance AlGaN/GaN power switch with HfO_2 insulation," *Applied Physics Letters*, vol. 95, no. 4, pp. 8–10, 2009.

[36] R. M. Lin, F. C. Chu, A. Das, S. Y. Liao, S. T. Chou, and L. B. Chang, "Physical and electrical characteristics of AlGaN/GaN metal-oxide- semiconductor high-electron-mobility transistors with rare earth Er_2O_3 as a gate dielectric," *Thin Solid Films*, vol. 544, pp. 526–529, 2013.

[37] P. W. Peacock and J. Robertson, "Bonding, Energies, and Band Offsets of Si-ZrO_2 and HfO_2 Gate Oxide Interfaces," *Physical Review Letters*, vol. 92, p. 057601, feb 2004.

[38] J. S. Jur, V. D. Wheeler, M. T. Veety, D. J. Lichtenwalner, D. W. Barlage, and M. Johnson, "Epitaxial Rare Earth Oxide Growth on GaN for Enhancement-mode MOSFETs," *CS MANTECH Conference, 2008, Chicago, IL*, no. 919, pp. 17–20, 2008.

[39] J. W. Johnson, B. Luo, F. Ren, B. P. Gila, W. Krishnamoorthy, C. R. Abernathy, S. J. Pearton, J. I. Chyi, T. E. Nee, C. M. Lee, and C. C. Chuo, "Gd_2O_3/GaN metal-oxide-semiconductor field-effect transistor," *Applied Physics Letters*, vol. 77, no. 20, pp. 3230–3232, 2000.

[40] M. D. Biegalski, J. H. Haeni, S. Trolier-McKinstry, D. G. Schlom, C. D. Brandle, and A. J. Ven Graitis, "Thermal expansion of the new perovskite substrates DyScO3and GdScO3," *Journal of Materials Research*, vol. 20, no. 4, pp. 952–958, 2005.

[41] B. Veličkov, V. Kahlenberg, R. Bertram, and M. Bernhagen, "Crystal chemistry of GdScO3, DyScO3, SmScO3 and NdScO3," *Zeitschrift für Kristallographie*, vol. 222, no. 9, pp. 466–473, 2007.

[42] Y. Liu, M. Xu, J. Heo, P. D. Ye, and R. G. Gordon, "Heteroepitaxy of single-crystal $LaLuO_3$ on GaAs(111)A by atomic layer deposition," *Applied Physics Letters*, vol. 97, no. 16, p. 162910, 2010.

[43] J. Schubert, O. Trithaveesak, W. Zander, M. Roeckerath, T. Heeg, H. Y. Chen, C. L. Jia, P. Meuffels, Y. Jia, and D. G. Schlom, "Characterization of epitaxial lanthanum lutetium oxide thin films prepared by pulsed-laser deposition," *Applied Physics A*, vol. 90, no. 3, pp. 577–579, 2007.

[44] K. Ovanesyan, A. Petrosyan, G. Shirinyan, C. Pedrini, and L. Zhang, "Single crystal growth and characterization of $LaLuO_3$," *Optical Materials*, vol. 10, pp. 291–295, sep 1998.

[45] F. X. Zhang, M. Lang, J. W. Wang, U. Becker, and R. C. Ewing, "Structural phase transitions of cubic Gd_2O_3 at high pressures," *Physical Review B - Condensed Matter and Materials Physics*, vol. 78, no. 6, pp. 1–9, 2008.

[46] H. Hardtdegen, N. Kaluza, R. Steins, P. Javorka, K. Wirtz, A. Alam, T. Schmitt, and R. Beccard, "Uniform III-nitride growth in single wafer horizontal MOVPE reactors," *physica status solidi (a)*, vol. 202, no. 5, pp. 744–748, 2005.

[47] NOVAGAN, "Novagan," 2018.

[48] S. Iacopetti, *Characterisation of Rare Earth Oxide/III-V Nitride semiconductor systems for electronic applications.* Master thesis, Politecnico Di Milano, 2015.

[49] S. Iacopetti, P. Shekhter, R. Winter, T. C. U. Tromm, J. Schubert, and M. Eizenberg, "The asymmetric band structure and electrical behavior of the $GdScO_3$ /GaN system," *Journal of Applied Physics*, vol. 121, no. 20, p. 205303, 2017.

[50] T. C. U. Tromm, A. Schafer, M. Luysberg, F. A. Wendt, A. Besmehn, M. Mikulics, H. Hardtdegen, S. Mantl, and J. Schubert, "(Invited) Ternary Rare Earth Based Oxides for Nitride Based Devices," *ECS Transactions*, vol. 72, pp. 307–317, may 2016.

[51] S. D. Wolter, S. E. Mohney, H. Venugopalan, A. E. Wickenden, and D. D. Koleske, "Kinetic study of the oxidation of gallium nitride in dry air," *Journal of the Electrochemical Society*, vol. 145, no. 2, pp. 629–632, 1998.

[52] M. Nespolo, "International Tables for Crystallography, Volume A, Space-group symmetry . 6th edition. Edited by Mois I. Aroyo. Wiley, 2016. Pp. xxi + 873. Price GBP 295.00, EUR 354.00 (hardcover). ISBN 978-0-470-97423-0.," *Acta Crystallographica Section A Foundations and Advances*, vol. 73, pp. 274–276,

may 2017.

[53] V. V. Afanas'ev, A. Stesmans, C. Zhao, M. Caymax, T. Heeg, J. Schubert, Y. Jia, D. G. Schlom, and G. Lucovsky, "Band alignment between (100)Si and complex rare earth/transition metal oxides," *Applied Physics Letters*, vol. 85, pp. 5917–5919, dec 2004.

[54] J. Kim, R. Mehandru, B. Luo, F. Ren, B. P. Gila, A. H. Onstine, C. R. Abernathy, S. J. Pearton, and Y. Irokawa, "Inversion behavior in Sc_2O_3/GaN gated diodes," *Applied Physics Letters*, vol. 81, no. 2, pp. 373–375, 2002.

[55] J. B. Cheng, A. D. Li, Q. Y. Shao, H. Q. Ling, D. Wu, Y. Wang, Y. J. Bao, M. Wang, Z. G. Liu, and N. B. Ming, "Growth and characteristics of La_2O_3gate dielectric prepared by low pressure metalorganic chemical vapor deposition," *Applied Surface Science*, vol. 233, no. 1-4, pp. 91–98, 2004.

[56] H. Nohira, T. Shiraishi, T. Nakamura, K. Takahashi, M. Takeda, S. Ohmi, H. Iwai, and T. Hattori, "Chemical and electronic structures of Lu_2O_3/Si interfacial transition layer," *Applied Surface Science*, vol. 216, no. 1-4 SPEC., pp. 234–238, 2003.

[57] C. L. Yuan, P. Darmawan, M. Y. Chan, and P. S. Lee, "Leakage conduction mechanism of amorphous Lu_2O_3 high-k dielectric films fabricated by pulsed laser ablation," *Europhysics Letters (EPL)*, vol. 77, p. 67001, mar 2007.

[58] P. Darmawan, C. L. Yuan, and P. S. Lee, "Trap-controlled behavior in ultrathin Lu_2O_3 high-k gate dielectrics," *Solid State Communications*, vol. 138, no. 12, pp. 571–573, 2006.

[59] C. Mizue, Y. Hori, M. Miczek, and T. Hashizume, "Capacitance–Voltage Characteristics of Al_2O_3/AlGaN/GaN Structures and State Density Distribution at Al_2O_3/AlGaN Interface," *Japanese Journal of Applied Physics*, vol. 50, no. 2, p. 021001, 2011.

[60] B. P. Gila, J. W. Johnson, R. Mehandru, B. Luo, A. H. Onstine, K. K. Allums, V. Krishnamoorthy, S. Bates, C. R. Abernathy, F. Ren, and S. J. Pearton, "Gadolinium Oxide and Scandium Oxide: Gate Dielectrics for GaN MOSFETs," *Physica Status Solidi (A) Applied Research*, vol. 188, no. 1, pp. 239–242, 2001.

[61] P. Aldebert and J. P. Traverse, "Etude par diffraction neutronique des structures de haute temperature de La2O3 et Nd2O3," *Materials Research Bulletin*,

vol. 14, pp. 303–323, 1979.

[62] T. C. U. Tromm, J. Zhang, J. Schubert, M. Luysberg, W. Zander, Q. Han, P. Meuffels, D. Meertens, S. Glass, P. Bernardy, and S. Mantl, "Ferroelectricity in Lu doped HfO_2 layers," *Applied Physics Letters*, vol. 111, no. 14, 2017.

[63] M. Kohli, P. Muralt, and N. Setter, "Removal of 90° domain pinning in (100) $Pb(Zr_{0.15}Ti_{0.85})O_3$ thin films by pulsed operation," *Applied Physics Letters*, vol. 72, no. 24, pp. 3217–3219, 1998.

[64] V. Fridkin and S. Durcharme, *Ferroelectricity at the Nanoscale*, vol. 1. Springer-Verlag Berlin Heidelberg, 2014.

[65] K. Kim and S. Lee, "Integration of lead zirconium titanate thin films for high density ferroelectric random access memory," *Journal of Applied Physics*, vol. 100, no. 5, p. 51604, 2006.

[66] J. F. Scott, *Ferroelectric memories*. Springer-Verlag Berlin Heidelberg, 2000.

[67] D. S. Jeong, R. Thomas, R. S. Katiyar, J. F. Scott, H. Kohlstedt, A. Petraru, and C. S. Hwang, "Emerging memories: Resistive switching mechanisms and current status," *Reports on Progress in Physics*, vol. 75, no. 7, 2012.

[68] C. Dubourdieu, J. Bruley, T. M. Arruda, A. Posadas, J. Jordan-Sweet, M. M. Frank, E. Cartier, D. J. Frank, S. V. Kalinin, A. A. Demkov, and V. Narayanan, "Switching of ferroelectric polarization in epitaxial $BaTiO_3$ films on silicon without a conducting bottom electrode," *Nature Nanotechnology*, vol. 8, no. 10, pp. 748–754, 2013.

[69] K. Kim and Y. J. Song, "Integration technology for ferroelectric memory devices," *Microelectronics Reliability*, vol. 43, no. 3, pp. 385–398, 2003.

[70] N. Setter, D. Damjanovic, L. Eng, G. Fox, S. Gevorgian, S. Hong, A. Kingon, H. Kohlstedt, N. Y. Park, G. B. Stephenson, I. Stolitchnov, A. K. Taganstev, D. V. Taylor, T. Yamada, and S. Streiffer, "Ferroelectric thin films: Review of materials, properties, and applications," *Journal of Applied Physics*, vol. 100, no. 5, 2006.

[71] C. Liu, E. F. Chor, and L. S. Tan, "Enhanced device performance of AlGaN/GaN HEMTs using HfO_2 high-κ dielectric for surface passivation and gate oxide," *Semiconductor Science and Technology*, vol. 22, no. 5, pp. 522–527, 2007.

[72] B. H. Lee, L. Kang, R. Nieh, W.-J. Qi, and J. C. Lee, "Thermal stability and electrical characteristics of ultrathin hafnium oxide gate dielectric reoxidized with rapid thermal annealing," *Applied Physics Letters*, vol. 76, no. 14, pp. 1926–1928, 2000.

[73] E. Bersch, S. Rangan, R. A. Bartynski, E. Garfunkel, and E. Vescovo, "Band offsets of ultrathin high-κ oxide films with Si," *Physical Review B - Condensed Matter and Materials Physics*, vol. 78, no. 8, pp. 1–10, 2008.

[74] O. Ohtaka, H. Fukui, T. Kunisada, and T. Fujisawa, "Phase Relations and Volume Changes of Hafnia under High Pressure and High Temperature," *Journal of the American Ceramic Society*, vol. 84, no. 6, pp. 1369–1373, 2001.

[75] S. Mueller, C. Adelmann, A. Singh, S. Van Elshocht, U. Schroeder, and T. Mikolajick, "Ferroelectricity in Gd-Doped HfO_2 Thin Films," *ECS Journal of Solid State Science and Technology*, vol. 1, no. 6, pp. N123–N126, 2012.

[76] T. Schenk, U. Schroeder, M. Pesic, M. Popovici, Y. V. Pershin, and T. Mikolajick, "Electric field cycling behavior of ferroelectric hafnium oxide," *ACS Appl Mater Interfaces*, vol. 6, no. 22, pp. 19744–19751, 2014.

[77] S. Starschich, D. Griesche, T. Schneller, R. Waser, and U. Böttger, "Chemical solution deposition of ferroelectric yttrium-doped hafnium oxide films on platinum electrodes," *Applied Physics Letters*, vol. 104, no. 20, p. 202903, 2014.

[78] P. D. Lomenzo, Q. Takmeel, C. Zhou, C. Chung, S. Moghaddam, J. L. Jones, and T. Nishida, "Mixed Al and Si doping in ferroelectric HfO_2 thin films," *Applied Physics Letters*, vol. 107, no. 24, p. 242903, 2015.

[79] S. Zarubin, E. Suvorova, M. Spiridonov, D. Negrov, A. Chernikova, A. Markeev, and A. Zenkevich, "Fully ALD-grown $TiN/Hf_{0.5}Zr_{0.5}O_2/TiN$ stacks: Ferroelectric and structural properties," *Applied Physics Letters*, vol. 109, no. 19, p. 192903, 2016.

[80] M. H. Park, Y. H. Lee, H. J. Kim, Y. J. Kim, T. Moon, K. D. Kim, J. Müller, A. Kersch, U. Schroeder, T. Mikolajick, and C. S. Hwang, "Ferroelectricity and Antiferroelectricity of Doped Thin HfO_2-Based Films," *Advanced Materials*, vol. 27, no. 11, pp. 1811–1831, 2015.

[81] T. D. Huan, V. Sharma, G. A. Rossetti, and R. Ramprasad, "Pathways towards ferroelectricity in hafnia," *Physical Review B*, vol. 90, no. 6, 2014.

[82] M. Hyuk Park, H. Joon Kim, Y. Jin Kim, T. Moon, and C. Seong Hwang, "The effects of crystallographic orientation and strain of thin $Hf_{0.5}Zr_{0.5}O_2$ film on its ferroelectricity," *Applied Physics Letters*, vol. 104, no. 7, p. 72901, 2014.

[83] J. Müller, T. S. Böscke, U. Schröder, S. Mueller, D. Bräuhaus, U. Böttger, L. Frey, and T. Mikolajick, "Ferroelectricity in Simple Binary ZrO_2 and HfO_2," *Nano Lett*, vol. 12, no. 8, pp. 4318–4323, 2012.

[84] S. Starschich, S. Menzel, and U. Böttger, "Pulse wake-up and breakdown investigation of ferroelectric yttrium doped HfO_2," *Journal of Applied Physics*, vol. 121, no. 15, p. 154102, 2017.

[85] S. E. Reyes-Lillo, K. F. Garrity, and K. M. Rabe, "Antiferroelectricity in thin-film ZrO_2 from first principles," *Physical Review B - Condensed Matter and Materials Physics*, vol. 90, no. 14, pp. 1–5, 2014.

[86] T. S. Böscke, S. Teichert, D. Bräuhaus, J. Müller, U. Schröder, U. Böttger, and T. Mikolajick, "Phase transitions in ferroelectric silicon doped hafnium oxide," *Applied Physics Letters*, vol. 99, no. 11, p. 112904, 2011.

[87] J. Müller, E. Yurchuk, T. Schlösser, J. Paul, R. Hoffmann, S. Müller, D. Martin, S. Slesazeck, P. Polakowski, J. Sundqvist, M. Czernohorsky, K. Seidel, P. Kücher, R. Boschke, M. Trentzsch, K. Gebauer, U. Schröder, and T. Mikolajick, "Ferroelectricity in HfO_2 enables nonvolatile data storage in 28 nm HKMG," *Digest of Technical Papers - Symposium on VLSI Technology*, pp. 25–26, 2012.

[88] F. Huang, Y. Wang, X. Liang, J. Qin, Y. Zhang, X. Yuan, Z. Wang, B. Peng, L. Deng, Q. Liu, L. Bi, and M. Liu, "HfO_2-Based Highly Stable Radiation-Immune Ferroelectric Memory," *IEEE Electron Device Letters*, vol. 38, no. 3, pp. 330–333, 2017.

[89] M. H. Lee, P.-G. Chen, C. Liu, K.-Y. Chu, C.-C. Cheng, M.-J. Xie, S.-N. Liu, J.-W. Lee, S.-J. Huang, M.-H. Liao, M. Tang, K.-S. Li, and M.-C. Chen, "Prospects for ferroelectric $HfZrO_x$ FETs with experimentally CET=0.98nm, SS for=42mV/dec, SSrev=28mV/dec, switch-off 0.2V, and hysteresis-free strategies," in *2015 IEEE International Electron Devices Meeting (IEDM)*, pp. 22.5.1–22.5.4, IEEE, dec 2015.

[90] W. Gao, A. Khan, X. Marti, C. Nelson, C. Serrao, J. Ravichandran, R. Ramesh, and S. Salahuddin, "Room-temperature negative capacitance in a ferroelectric-dielectric superlattice heterostructure," *Nano Lett*, vol. 14, no. 10,

pp. 5814–5819, 2014.

[91] C. W. Yeung, A. I. Khan, S. Salahuddin, and C. Hu, "Device Design Considerations for Ultra-Thin Body Non-Hysteretic Negative Capacitance FETs," *IEEE ELECTRON DEVICE LETTERS,*, pp. 1–2, 2013.

[92] A. I. Khan, K. Chatterjee, B. Wang, S. Drapcho, L. You, C. Serrao, S. R. Bakaul, R. Ramesh, and S. Salahuddin, "Negative capacitance in a ferroelectric capacitor," *Nat Mater*, 2014.

[93] M. Hoffmann, M. Pesic, K. Chatterjee, A. I. Khan, S. Salahuddin, S. Slesazeck, U. Schroeder, and T. Mikolajick, "Direct Observation of Negative Capacitance in Polycrystalline Ferroelectric HfO_2," *Advanced Functional Materials*, vol. 26, no. 47, pp. 8643–8649, 2016.

[94] A. I. Khan, K. Chatterjee, J. P. Duarte, Z. Lu, A. Sachid, S. Khandelwal, R. Ramesh, C. Hu, and S. Salahuddin, "Negative Capacitance in Short-Channel FinFETs Externally Connected to an Epitaxial Ferroelectric Capacitor," *IEEE Electron Device Letters*, vol. 37, pp. 111–114, jan 2016.

[95] K.-S. Li, P.-G. Chen, T.-Y. Lai, C.-H. Lin, C.-C. Cheng, C.-C. Chen, Y.-J. Wei, Y.-F. Hou, M.-H. Liao, M.-H. Lee, M.-C. Chen, J.-M. Sheih, W.-K. Yeh, F.-L. Yang, S. Salahuddin, and C. Hu, "Sub-60mV-Swing Negative-Capacitance FinFET without Hysteresis," *IEEE ELECTRON DEVICE LETTERS,*, pp. 22.6.1–22.6.4, 2015.

[96] M. H. Lee, S. T. Fan, C. H. Tang, P. G. Chen, Y. C. Chou, H. H. Chen, J. Y. Kuo, M. J. Xie, S. N. Liu, M. H. Liao, C. A. Jong, K. S. Li, M. C. Chen, and C. W. Liu, "Physical thickness 1.x nm ferroelectric $HfZrO_x$ negative capacitance FETs," *Technical Digest - International Electron Devices Meeting, IEDM*, pp. 12.1.1–12.1.4, 2017.

[97] U. Schroeder, S. Mueller, J. Mueller, E. Yurchuk, D. Martin, C. Adelmann, T. Schloesser, R. van Bentum, and T. Mikolajick, "Hafnium Oxide Based CMOS Compatible Ferroelectric Materials," *ECS Journal of Solid State Science and Technology*, vol. 2, no. 4, pp. N69–N72, 2013.

[98] Y. Sharma, D. Barrionuevo, R. Agarwal, S. P. Pavunny, and R. S. Katiyar, "Ferroelectricity in Rare-Earth Modified Hafnia Thin Films Deposited by Sequential Pulsed Laser Deposition," *ECS SOLID STATE LETTERS*, vol. 4, no. 11, pp. N13–N16, 2015.

[99] S. Starschich, D. Griesche, T. Schneller, and U. Böttger, "Chemical Solution Deposition of Ferroelectric Hafnium Oxide for Future Lead Free Ferroelectric Devices," *ECS Journal of Solid State Science and Technology*, vol. 4, no. 12, pp. P419–P423, 2015.

[100] H. J. Kim, M. H. Park, Y. J. Kim, Y. H. Lee, T. Moon, K. D. Kim, S. D. Hyun, and C. S. Hwang, "A study on the wake-up effect of ferroelectric $Hf_{0.5}Zr_{0.5}O_2$ films by pulse-switching measurement," *Nanoscale*, vol. 8, no. 3, pp. 1383–1389, 2016.

[101] X. Ma, X. Wang, K. Han, W. Wang, H. Yang, C. Zhao, D. Chen, and T. Ye, "Remote Scavenging Technology Using Ti/TiN Capping Layer Interposed in a Metal/High-k Gate Stack," *ECS Transactions*, vol. 50, pp. 285–290, mar 2013.

[102] T. S. Böscke, J. Müller, D. Bräuhaus, U. Schröder, and U. Böttger, "Ferroelectricity in hafnium oxide thin films," *Applied Physics Letters*, vol. 99, no. 10, p. 102903, 2011.

[103] B. Gao, H. W. Zhang, S. Yu, B. Sun, L. F. Liu, X. Y. Liu, Y. Y. Wang, R. Q. Han, J. F. Kang, B. Yu, and Y. Y. Wang, "Oxide-based RRAM: Uniformity improvement using a new material-oriented methodology," *Symposium on VLSI Technology Digest of Technical Papers*, pp. 30–31, 2009.

[104] H. Zhang, L. Liu, B. Gao, Y. Qiu, X. Liu, J. Lu, R. Han, J. Kang, and B. Yu, "Gd-doping effect on performance of HfO_2 based resistive switching memory devices using implantation approach," *Applied Physics Letters*, vol. 98, no. 4, p. 042105, 2011.

[105] M. Pesic, F. P. G. Fengler, L. Larcher, A. Padovani, T. Schenk, E. D. Grimley, X. Sang, J. M. LeBeau, S. Slesazeck, U. Schroeder, and T. Mikolajick, "Physical Mechanisms behind the Field-Cycling Behavior of HfO_2-Based Ferroelectric Capacitors," *Advanced Functional Materials*, vol. 26, no. 25, pp. 4601–4612, 2016.

[106] U. Schroeder, M. Pešić, T. Schenk, H. Mulaosmanovic, S. Slesazeck, J. Ocker, C. Richter, E. Yurchuk, K. Khullar, J. Müller, P. Polakowski, E. D. Grimley, J. M. LeBeau, S. Flachowsky, S. Jansen, S. Kolodinski, R. van Bentum, A. Kersch, C. Künneth, and T. Mikolajick, "Impact of field cycling on HfO_2 based non-volatile memory devices," *2016 46TH EUROPEAN SOLID-STATE DEVICE RESEARCH CONFERENCE (ESSDERC)*, pp. 364–368, 2016.

[107] J. Müller, T. Böscke, S. Müller, E. Yurchuk, P. Polakowski, J. Paul, D. Martin, T. Schenk, K. Khullar, A. Kersch, W. Weinreich, S. Riedel, K. Seidel, A. Kumar, T. M. Arruda, S. V. Kalinin, T. Schlösser, R. Boschke, R. van Bentum, U. Schröder, and T. Mikolajick, "Ferroelectric Hafnium Oxide A CMOS-compatible and highly scalable approach to future ferroelectric memories," *IEDM - Electron Devices Meeting*, 2013.

[108] W. D. Nix and B. M. Clemens, "Crystallite coalescence: A mechanism for intrinsic tensile stresses in thin films," *Journal of Materials Research*, vol. 14, pp. 3467–3473, aug 1999.

[109] Q. Han, T. C. U. Tromm, J. Schubert, S. Mantl, and Q.-T. Zhao, "Steep Slope Negative Capacitance FDSOI MOSFETs with Ferroelectric $HfYO_X$," in *2018 Joint International EUROSOI Workshop and International Conference on Ultimate Integration on Silicon (EUROSOI-ULIS)*, vol. 2, pp. 1–4, IEEE, 2018.

List of publications

Journal papers

- T. C. U. Tromm, J. Zhang, J. Schubert, M. Luysberg, W. Zander, Q. Han, P. Meuffels, D. Meertens, S. Glass, P. Bernardy, and S. Mantl, “Ferroelectricity in Lu doped HfO_2 layers,” *Applied Physics Letters*, vol. 111, no. 14, 2017.

- T. C. U. Tromm, A. Schäfer, M.Luysberg, F. Wendt, A. Besmehn, M. Mikulics, H. Hardtdegen, S. Mantl, J. Schubert, "Ternary Rare Earth Based Oxides for Nitride Based Devices", *ECS Transactions*, vol. 72, no. 2, 2016.

- S. Iacopetti, P. Shekhter, R. Winter, T. C. U. Tromm, J. Schubert, M. Eizenberg, "The asymmetric band structure and electrical behavior of the $GdScO_3$ /GaN system", *Journal of Applied Physics*, vol. 121, no. 20, 2017.

- Q. Han, T.C.U. Tromm, J. Schubert, S. Mantl, Q. Zhao, "Steep Slope Negative Capacitance FDSOI MOSFETs with Ferroelectric $HfYO_X$", *2018 Joint International EUROSOI Workshop and International Conference on Ultimate Integration on Silicon (EUROSOI-ULIS)*, vol. 2, no. 2, 2018.

Conference contributions

- T. C. U. Tromm, A. Schäfer, F. Wendt, W. Zander, A. Tiedemann, K.-H. Deussen, J. Schubert, M. Luysberg, S. Mantl, "Doping of HfO_2 gate oxides to raise the dielectric constant (κ). Poster presentation at the *Nanoelectronic Days 2015*, Jülich, Germany, 2015

- T.C.U. Tromm, J. Schubert, W. Zander, M. Luysberg, S. Mantl, "PLD grown ferroelectric HfO_2, Talk at the *Novel high-κ Application Workshop 2016*, Dresden, Germany, 2016

- T. C. U. Tromm, J. Schubert, W. Zander, D. Meertens, M. Kruth, H. Hardtdegen, S. Mantl, M. Luysberg, "Influence of the interface on electric properites and growth of non-thermodynamic equilibrium phases: Hexagonal $GdScO_3$ and $LaLuO_3$ on GaN (0001)., Poster presentation at the*Microscopy Conference 2017*, Lausanne, Switzerland, 2017.

Acknowledgement

This work would not have been possible without the amazing support and advise of a numerous of people. I would like to thank those people, who made my time at the research center Jülich an interesting and enriching experience.
In particular I want to thank Prof. Mantl, who gave me the opportunity to work in his research group and being an encouraging supervisor of my work. I also want to thank Prof. Mayer for reviewing my thesis as second promoter.
A special thank you goes to my supervisors Dr. Jürgen Schubert und Dr. Martina Luysberg for the many helpful discussions and encouragement in every single step of my Ph.D. thesis. Dr. Jürgen Schubert has an unlimited knowledge about PLD growth and crystallography, and introduced me to his scientific network, that helped me to make progress with this thesis. Dr. Martina Luysberg introduced me to the various microscopes and promoted this thesis by her critical questions.
Another huge thanks goes to Dr. Dan Buca and Dr. Qing-Tai Zhao for sharing their knowledge with me. Special thanks go to Willi Zander, who grew an endless number of samples for me. I also want to thank the 'Waldschlösschen-Team' Andreas Tiedemann, Patric Bernardy and Karl-Heinz Deussen, that supported my thesis by processing a infinite number of samples.
Many thanks go to Doris Mertens, Lidia Kibkalo and Steffi Lenk, whose support made the TEM investigations even possible.
There are many students I want to thank for sharing their knowledge and helping me with my thesis, but especially for making my daily work more fun: Stefan Glass, Denis Rainko, Daniela Stange, Dr. Nils von den Driesch, Qinghua Han, Konstantin Mertens, Paulus Aleksa, Keyvan Narimani and my former colleagues Dr. Anna Schäfer, Dr. Christian Schulte-Braucks, Dr. Stephan Wirths and Dr. Gia Vinh Luong. I also want to thank my colleagues in the Ernst Ruska-Centre, that helped me with the various microscopes and advise: Maximilian Kruth, Dr. Juri Barthel, Dr. Michael Schnedler, Wilma Sybertz, Dr. Andras Kovacs, Dr. Marc Heggen, Werner Pieper, Martin Gocyla, Dr. Katherine MacArthur and Dr. Marta Lipinska-Chwalek. I also appreciated the successful cooperation with Prof. Moshe Eizenberg, Sara Iacopetti, Dr. Pini Shekhter and Roy Winter from the Technion in Haifa. Further, I want to thank Dr. Ute Kolb and Sergi Plana Ruiz for their ADT investigations.

Finally I want to thank my familiy for their support and encouragement at any time. A special thanks goes to my girlfriend Ricarda, who motivated me and supported me, even when I had doubts.